INFORMATION TO USERS

The most advanced technology has been used to photograph and reproduce this manuscript from the microfilm master. UMI films the text directly from the original or copy submitted. Thus, some thesis and dissertation copies are in typewriter face, while others may be from any type of computer printer.

The quality of this reproduction is dependent upon the quality of the copy submitted. Broken or indistinct print, colored or poor quality illustrations and photographs, print bleedthrough, substandard margins, and improper alignment can adversely affect reproduction.

In the unlikely event that the author did not send UMI a complete manuscript and there are missing pages, these will be noted. Also, if unauthorized copyright material had to be removed, a note will indicate the deletion.

Oversize materials (e.g., maps, drawings, charts) are reproduced by sectioning the original, beginning at the upper left-hand corner and continuing from left to right in equal sections with small overlaps. Each original is also photographed in one exposure and is included in reduced form at the back of the book. These are also available as one exposure on a standard 35mm slide or as a 17" x 23" black and white photographic print for an additional charge.

Photographs included in the original manuscript have been reproduced xerographically in this copy. Higher quality 6" x 9" black and white photographic prints are available for any photographs or illustrations appearing in this copy for an additional charge. Contact UMI directly to order.

U·M·I

University Microfilms International
A Bell & Howell Information Company
300 North Zeeb Road, Ann Arbor, MI 48106-1346 USA
313/761-4700 800/521-0600

Order Number 9000014

Optical properties and local atomic bonding in hydrogenated amorphous silicon-carbon alloy films

Basa, Deepak Kumar, Ph.D.

City University of New York, 1989

U·M·I
300 N. Zeeb Rd.
Ann Arbor, MI 48106

PLEASE NOTE:

Best Copy Available. Filmed
as Received

U·M·I

OPTICAL PROPERTIES AND LOCAL ATOMIC BONDING
IN
HYDROGENATED AMORPHOUS SILICON-CARBON ALLOY FILMS

4

BY

DEEPAK KUMAR BASA

A dissertation submitted to the Graduate Faculty in Physics in partial fulfillment of the requirements for the degree of Doctor of Philosophy, The City University of New York.

1989

This manuscript has been read and accepted for the Graduate Faculty in Physics in satisfaction of the dissertation requirement for the degree of Doctor of Philosophy.

1/5/89 — Frederick W. Smith

date — Chairman of Examining Committee

1/5/89

date — Executive Officer

Frederick W. Smith

Supervisory Committee

The City University of New York

ABSTRACT

OPTICAL PROPERTIES AND LOCAL ATOMIC BONDING IN HYDROGENATED AMORPHOUS SILICON-CARBON ALLOY FILMS

By

Deepak K Basa

Advisor: Professor Frederick W.Smith

Thin films of a-$Si_{1-x}C_x$:H alloys have been prepared via the rf glow discharge of acetylene and silane and ethylene and silane. The optical constants, optical bandgap E_{opt} and the infrared absorption have been determined as functions of composition and annealing temperature in order to understand the effect of the local silicon, carbon, and hydrogen bonding configurations on the optical properties of these alloy films.

The films in this alloy series are proposed to be macroscopically homogeneous, while having a heterogeneous microstructure. A microstructural model, based on four components: amorphous polymeric, amorphous graphitic, amorphous tetrahedral and void, is proposed to model the optical response of these films. This microstructural model gives a good description of the observed dependences of ϵ_1 and ϵ_2 on composition and provides a convincing demonstration that appearance of the amorphous graphitic component in the

films limits the attainable value of E_{opt} in this alloy series as the carbon content increases. In addition, the model provides strong evidence that complete chemical ordering with homogeneous dispersion exists within the amorphous tetrahedral component across the entire alloy series. Thus we have provided for the first time a new experimental approach to the issue of chemical ordering and have asserted that the optical constants measurements have the potential to be a sensitive probe of film microstructure and of chemical ordering.

The annealing study of these films has enabled us to understand the changes in the local bonding and the structural changes in the network leading to crystallization. It has been established that there is a change from amorphous to microcrystalline and then to crystalline phase with increase in the annealing temperature. In addition this study enables us to resolve conclusively the controversy regarding the assignment of various IR modes of a-$Si_{1-x}C_x$:H films.

It is also observed that the optical band gap E_{opt} correlates well with the hydrogen concentration. Further, it is established that E_{opt} is controlled by the amount of disorder and that the hydrogen affects E_{opt} indirectly through its effect on disorder.

ACKNOWLEDGEMENT

I wish to express my deep sense of gratitude to Prof F.W.Smith for his patient guidance and continued support during the course of this research. He has been of immense help throughout the time this project was underway. He has been both advisor and friend, and has helped this gruelling undertaking to see the light of the day.

I also offer thanks to other members of my doctoral committee, who have, without exception, contributed to this work either through discussions, the procurement of needed experimental facilities, or both. In particular, I wish to thank Prof R.R. Alfano and Prof Green for the extensive use of their spectrophotometer, and also to Prof Woodward for the use of his FTIR.

Also, special thanks are due to Prof H.Z. Cummins Dr. K. Arya, Dr S.Gayen and Dr C. Pande and Dr K. Mui of CCNY and Reed Corderman of BNL for many discussions.

Finally, I thank Mr T. Mishra and Mr U. Mishra for the extensive use of their computers and Mr Dharnidhar Chhatoi for typing this manuscript.

DEDICATION

To my parents

CONTENTS

ABSTRACT

ACKNOWLEDGEMENT

DEDICATION

CONTENTS

I. INTRODUCTION 1

II. BACKGROUND 4

A. Difference between amorphous and crystalline semiconductors 4

B. Discussion of the basic properties of the tetrahedrally coordinated amorphous semiconductors 6

C. Review of previous research on a-$Si_{1-x}C_x$:H films 7

III. THEORY 12

A. Concepts of density of states and band gap 12

B. Quantum mechanical model of optical absorption in an amorphous semiconductor 17

C. Expressions for getting n,k,d from R_a, R_s and T 23

D. Effective Medium Approximation 26

E. Microstructural model 28

F. IR absorption. 29

IV. EXPERIMENTAL PROCEDURE 35

A. Experimental apparatus 35

B. Substate preparation 45

C. Sample preparation 45

D. Analysis procedure 47

V. OPTICAL CONSTANTS, MICROSTRUCTURE, AND CHEMICAL ORDERING 53

A.Results 53

B.Discussion 64

VI. INFRARED ABSORPTION, STRUCTURAL CHANGE, AND LOCAL ATOMIC BONDING 75

A.Results 75

I. Effect of annealing temperature 75

II.Effect of composition 84

B.Discussion 90

VII.CONCLUSIONS 113

TABLE CAPTIONS 118

TABLES 120

FIGURE CAPTIONS 138

FIGURE 146

APPENDICES 202

I. Tetrahedron model for the dielectric function of amorphous silicon-carbon alloys 202

II.Frequency shift of Si-H using Lucovsky's approach 212

REFERENCES 213

CHAPTER I

INTRODUCTION

Films of primarily tetrahedrally bonded binary amorphous semiconductors like hydrogenated silicon-carbon alloy films ($a\text{-}Si_{1-x}C_x\text{:}H$) continue to be of considerable current interest both fundamentally in regards to understanding the effect of the local silicon, carbon, and hydrogen bonding configurations on film properties[1-10] and also technologically in regard to their applications as p-type layers in p-i-n a-Si:H photovoltaic devices[11,12] and as potentially useful optical and solar selective coatings.[13]

In the process of film growth a number of microstructures are formed which include void, polymeric, tetrahedral and graphitic components. These microstructures and their relative abundance in the film determines its electronic[14] and optical properties.[15-17]

Although a broad outline of the interesting properties of $a\text{-}Si_{1-x}C_x\text{:}H$ films has been fairly well established, there has yet to be undertaken a careful study of their optical constants and the infrared absorption either for the as-deposited films with varying composition or for films given subsequent anneals. The study of the variation of the optical constants with composition is very important to tailor the properties of the film for specific purpose.

Further, the optical band gap E_{opt}, which is a very useful parameter for the characterization of amorphous semiconducting films, can be extracted form the energy dependence of the imaginary part of the dielectric constant using Tauc's relation.[18]

The goal of my thesis is to get quantitative microstructural information from the measured optical properties of amorphous hydrogenated silicon carbon alloy films and to investigate if there is any chemical short range order (SRO) in the local atomic bonding. In the present context, the chemical SRO refers to an enhanced probability for the formation of Si-C bonds in the given alloy.

Another objective is to study the change in hydrogen content and the nature of bonding of Si, C, H, and O and to investigate the structural changes in the network leading to crystallization from the measured optical properties (both IR and visible) with annealing temperature. Clearly, the annealing study will help to determine the thermal stability of the films which is very important technologically for, if the material is to be used in devices, it must be stable.

My thesis will present data in two sections, the first to include the careful investigation of the optical constants for the as-deposited nine alloy films with varying compositions ranging from a-C:H to a-Si:H and the

second segment covers the detailed study of the infrared absorption of these alloy films as a function of composition and annealing temperature. The following section will outline the works that have been done and the work that needs to be done for the hydrogenated silicon carbon alloy films. In the section on theory I will present the parameters according to current theory, utilized in characterizing amorphous semiconductors, as well as proposing the microstructural model necessary to model the optical response. This section is followed by the description of the experimental set up necessary for the deposition as well as for the characterization of the hydrogenated amorphous silicon carbon films.

CHAPTER II

BACKGROUND

A. Difference between crystalline & amorphous semiconductors

The structures of amorphous semiconductors are developed by the repetition of one or more basic molecular[19] units, in a way that cannot be identified topologically with any known crystal structure or indeed with any infinite periodic array. The atomic order within a molecular unit might be similar within small bond angle distortions in both the crystalline and amorphous phases, yet quite different within large volumes. This order within the molecular units is responsible in large part for establishing the electronic band widths, which explains the early observation of the similarity of the optical band gaps of many materials in their amorphous and crystalline phases.[20]

In contrast to the crystalline material, the density of states of amorphous material is nowhere zero[21] (see Fig.2.1). Both the conduction band and the valence band have tail states and deeper in the gap are the defect-related gap states. The tail states are intimately associated with the disorder in the non-crystalline structure. The defect-related gap states originate from structural and coordination defects (atoms which are not bonded according to their normal valency) as well as from

impurities.

The tail states as well as the defect-related states are localized to a region of a few atoms. The charge carriers in these states have zero mobility at low temperatures. The carriers in extended band states, in contrast, have a finite mobility. The demarcation energies E_V and E_C separating extended from localized states thus define a mobility gap (see Fig. 2.1).

The optical absorption process can occur between extended band states (B-B), between the tail states and band states (T-B), and between gap states and band states (G-B). The outcome of these transitions is that the optical absorption in amorphous semiconductors can be separated into three regions as shown in Fig. 2.2. Regions A, B, C correspond to the transitions between (G-B), (T-B), and (B-B), respectively.

In amorphous semiconductors, even at energies well separated from band edges, the atomic potential is strong enough that even slight distortions in the nearest neighbor bond length and bond angle distributions, within otherwise identical molecular units, leads to strong electronic scattering and a short coherence length of the wave functions. Indeed, the coherence length is of the order of the lattice spacing and the resulting uncertainty in the wave vector k is of the order of the wavevector itself. This leads to the breakdown of momentum selection rule in

the optical transitions. However, the momentum may be transferred to the whole lattice of the amorphous material rather than to phonons and, therefore, the optical transitions in amorphous semiconductors may be termed non-direct as opposed to indirect. Here, no phonon absorption or emission processes to conserve the energy need to be involved. This is perhaps the single most important difference between the responses of crystalline and amorphous semiconductors.

B.Discussion of the basic properties of the tetrahedrally coordinated amorphous semiconductors.

The end points of a-$Si_{1-x}C_x$:H are a-Si:H and a-C:H. Both a-Si:H and a-C:H are interesting materials in their own right. The bonded hydrogen in a-Si:H was a significant factor in transforming a-Si to a new optoelectronic[22] material (a-Si:H). In a-Si:H, the hydrogen (10-20 at%) serves to passivate dangling bonds and also to relax the strained a-Si network, thereby contributing to the attainment of a more ideal tetrahedrally coordinated Si network.

In a-C:H, the situation is more complex due to the fact that carbon can be bonded in either trigonal (graphitic) or tetrahedral (diamondlike) coordination. The hydrogen (30- 50 at%) in a-C:H also serves an important role in passivating dangling bonds and in promoting tetrahedral coordination for the carbon atoms to which it is bonded.[15] These a-C:H films have also been referred to as "diamondlike" due to

their high transparency[23] (optical gap ~ 2.3 eV), high resistivity, and high hardness. In addition, a-C:H can be doped[24] n- or p- type via the incorporation of phosphorus or boron atoms, respectively, though not with the same efficiency as has been obtained for a-Si:H. Thus, a-C:H films have potential applications as hard, transparent optical coatings, wear-resistant coatings and also as a novel semiconducting material.

The outstanding problem for a-C:H has been the preparation of diamondlike films which are both very hard and optically transparent. The difficulty in achieving this important goal has been due to the relatively small volume fraction (0.10-0.15) of graphitically bonded carbon which remain in the film.[15] In order to investigate how the tetrahedral coordination for carbon in the film enhances their 'diamondlike' properties, we have chosen to prepare and characterize the a-$Si_{1-x}C_x$:H films.

C. Review of previous research on a-$Si_{1-x}C_x$:H

The electronic and optical properties of the a-$Si_{1-x}C_x$:H alloy films reflect the local atomic bonding configurations present in the material. An important issue for a-$Si_{1-x}C_x$:H films is the nature of the bonding of the Si and C atoms in the amorphous tetrahedral component. An outstanding question is whether the silicon-carbon tetrahedral bonding configurations are completely random or whether chemical short range order (SRO) may be present in

the films. Specifically, complete chemical SRO, which corresponds to the maximum possible number of Si-C bonds actually present in the films, with no C-C bonds in Si-rich films, while in C-rich films no Si-Si bonds would be present, even though these bonds would be statistically allowed in a completely disordered or random alloy.

Previous experimental work concerning the existence of chemical SRO in amorphous silicon-carbon alloys has involved techniques which can probe the local atomic bonding configurations. These includes Raman scattering,[25-27] infrared absorption,[27] photoelectron spectroscopy,[4,28,29] electron diffraction,[8] and electron energy loss spectroscopy.[8]

Raman spectra showing C-C bonds in C-deficient amorphous SiC films have been observed[25] and are consistent with at least partial random local bonding, ie. the absence of complete chemical SRO. More recent Raman and IR absorption results[27] in a-SiC, however, claim to be consistent with some degree of chemical SRO in as-deposited films, with phase separation into SiC and either Si- or C- like clusters developing in the alloys upon annealing. Photoelectron spectroscopy results (XPS, UPS)[4,28,29] have generally been interpreted in terms of complete chemical disorder, but may not be inconsistent with some chemical ordering as long as the chemically-ordered bonds are homogeneously dispersed through the

medium, without phase separation.[27] Very recent electron diffraction[8] and electron energy loss studies on an a-$Si_{0.68}C_{0.32}$:H film have yielded evidence for chemical ordering, but cannot distinguish between homogeneous dispersion and phase separation. Thus there have been claims in literature regarding both the absence and presence of chemical ordering in a-$Si_{1-x}C_x$:H alloy films but the question has not been resolved satisfactorily. In the present thesis, we propose a new experimental approach to the issue of chemical ordering and resolve the issue satisfactorily for our films.

In spite of the attention received by the films of tetrahedrally bonded, binary amorphous semiconductors such as a-$Si_{1-x}C_x$:H, few investigations of structural changes leading to crystallization in these films have been reported. It is important to investigate how a binary amorphous semiconductor like a-$Si_{1-x}C_x$:H is crystallized by annealing, because if this material is to be used in devices, it must be stable. The structure and the local bonding configuration of an amorphous solid are not determined and fixed by thermodynamic equilibrium conditions but can be altered by some means (like annealing) which change the energy of the system.

To probe the local atomic bonding configurations present in the film, Fourier transform infrared (FTIR) spectroscopy is used. The as-deposited a-$Si_{1-x}C_x$:H films

exhibit four main absorption regions in the range from 400 to 4000 cm^{-1} in the infrared spectrum[12] (see Fig. 2.3).

a) The absorption band from 2000 to 2300 cm^{-1} is due to Si-H stretch.

b) The absorption band between 2800 and 3000 cm^{-1} is ascribed to C-H stretch.

c) The absorption bands from 1200 to 1500 cm^{-1} are due to bending and scissoring modes of CH_2, CH_3, $Si(CH_3)$, $C(CH_3)$.

d) The absorption bands from 600-1200 cm^{-1} are ascribed to Si-C stretch, Si-O stretch, SiH_2 and $(SiH_2)_n$ bending and Si-H group rocking.

A lot of controversy exists in the assignment of various infrared modes of $a\text{-}Si_{1-x}C_x:H$ films. The Si-H stretch in $a\text{-}Si_{1-x}C_x:H$, peaked near 2085 cm^{-1}, is assigned to SiH_2 stretching mode[30,31] and or to a shift of Si-H monohydride in a different environment.[3,32] Further there is controversy in the assignment of 650 cm^{-1} peak. Wieder et al[3] have assigned this mode to Si-C stretch but McKenzie[33] has assigned this to Si-H group rocking or wagging mode. The C-H related modes are observed to peak at 2800, 2870, 2915, 2950 cm^{-1}. A lot of uncertainty exists in the assignment of C-H related peaks. The peak near 2915 cm^{-1}, for example, is assigned to C-H monohydride by Dischler et al[33a] while Tawada et al[12] assigned it to CH_2 stretch. Wieder et al[3] and McKenzie on the other hand assigned C-H related peaks to be due to CH_3 and CH_2 stretch. The

strongest feature in these spectra occurs between 700- 800 cm^{-1}. A lot of controversy in the assignment of this mode exists. The peak in this region (780 cm^{-1}) is assigned to the $Si-CH_3$ rocking or wagging mode by Wieder et al.[3] However, Katayama et al[34] concluded that this peak is assigned to the Si-C stretching mode, because this peak could be seen in the sputtered $a-Si_{1-x}C_x$ without hydrogen. Further Borders et al[35] found that for an ion-implanted $a-Si_{1-x}C_x$ sample the absorption maximum occurred at a somewhat lower wavenumber (700-725 cm^{-1}). McKenzie,[33] however, assigned Si-C stretching mode to have a wide range of wavenumbers (700-800 cm^{-1}). Thus there exist a lot of controversy in the assignment of various IR modes of $a-Si_{1-x}C_x:H$.

To resolve these issues we have undertaken a careful study of a film of approximately 20% C at various annealing temperature and of the films varying in composition. Further, the study of the change in C-H, Si-H, Si-C, Si-O modes of the above films with composition and annealing temperature is undertaken to understand the nature of hydrogen bonding on the film properties and to investigate the structural changes leading to crystallization.

CHAPTER III

THEORY

A. Concept of Density of states and band gap.

1. Concept of Density of States

In order to precisely define the basis of the various optical parameters to be obtained further on, it is necessary to give the form of the electron density of states. Fig. 2.1 sketches the density of electron energy states N(E). This is essentially the distribution of energy states of the CFO model[36] that has been proposed by Cohen, Fritzsche, and Ovshinsky in 1969. Both the conduction band and the valence bands have tail states, and deeper in the gap are the defect related gap states. Hence, in contrast to crystals, N(E) of amorphous material is nowhere zero.

The tail states are intimately associated with the disorder in the noncrystalline structure. The valence band tail states are covalent bonds that are weaker than normal. This can happen, for instance, when the covalent angle is bent from its equilibrium value, when the bond is stretched due to internal strains, or when some antibonding orbital is mixed in. That occurs, for instance, when atoms bond together in odd-numbered rings containing 5,7,9 atoms (instead of 6 atoms in the diamond structure). Moreover, it was found, both theoretically and experimentally, that there are net static charges on some atoms or group of atoms.[37] These net charges produce potential fluctuations

which remove any sharp features in N(E). All the above mentioned effects produce tail states extending down in energy from the (antibonding) conduction band. The total number of tail states[21] is approximately 10^{-3} of the number of states in one band.

The defect related gap states originate from structural and coordination defects (atoms which are not bonded according to their normal valency) as well as from impurities. A typical defect related gap state is a dangling bond and it lies near the gap center as it is not bonded (and not antibonded). Having one electron only, it is easily detectable by measuring the electron magnetic moment by electron spin resonance (ESR). The number of defect related gap states[21] varies between 10^{-5} to 10^{-7} to the number of states in one band.

The tail states, as well as the defect-related states, are localized to a region of a few atoms. A charge carrier occupying them has, therefore, no chance of moving away (zero mobility) at low temperatures. Carriers in extended band states, in contrast, have a finite mobility. The demarcation energies E_v and E_c separating extended from localized states thus define a mobility gap

Optical absorption processes can occur between extended band states (B-B), between the tail states and band states(T-B) and between gap states and band states (G-B). The strength of optical absorption is given by the

logarithmic fraction of photons absorbed per cm of the material. This absorption coefficient α is proportional to the product of density of those occupied states and the density of those unoccupied states. Since the density of states N(E) of band, tail and gap states differ so drastically, the absorption coefficient shows wide variation in its magnitude. These gap state to band state (G-B) transitions start at the threshhold energy for photoconductivity. At higher photon energies $h\nu$, transitions between tail states and the band state (T-B) occur, and at even higher band to band (B-B) transitions takes place. The strongest absorption is caused by B-B transitions, G-B absorption is the weakest and changes with N(E) of the gap states from sample to sample. The T-B absorption region is nearly exponential suggesting that N(E) of the tail states falls off exponentially into the gap.

The low absorption coefficients due to (G-B) transition are determined by photo-thermal spectroscopic techniques, namely photo-thermal deflection spectroscopy or photo acoustic spectroscopy. The absorption due to (T-B) transitions are determined by optical absorption spectroscopy and also by photo-thermal deflection spectroscopy or photo-acoustic spectroscopy. The absorption due to (B-B) transitions are determined by direct optical absorption spectroscopy. In this thesis we limit ourselves to the absorption due to (B-B) and (T-B) transitions.

The interaction with light provides a powerful means for probing the electronic and vibrational structure of a solid. The optical response function of a solid involves a pair of spectral functions (two are needed to describe the amplitude and the phase of the response) which are typically taken to be the real and imaginary parts of the frequency dependent dielectric constant. For example, the complex dielectric constant $\epsilon^{c}(\nu) = \epsilon_1(\nu)+i\epsilon_2(\nu)$, connects E, the electric field amplitude of an incident light wave of frequency ν, to $P(\nu)$ the complex amplitude of the polarization wave induced in the solid, by

$$P(\nu) = \frac{1}{4\pi}\left[\epsilon^{c}(\nu) - 1\right] E(\nu) \tag{3.1}$$

For the situations in which the light is transmitted through a sample having transmittance T and reflectance R, the optical absorption coefficient $\alpha(\nu)$ may be measured. This quantity $\alpha(\nu)$ describes the attenuation of the intensity of the beam for a path length x propagating within the sample, and is given by the expression

$$T = (1-R)^2 e^{-\alpha x}/(1-R^2 e^{-2\alpha x}) \tag{3.2}$$

Unlike the other optical quantities mentioned above, $\alpha(\nu)$ is not dimensionless but instead has the dimension of reciprocal length. $\alpha(\nu)$ and $\epsilon_2(\nu)$ are related as $\alpha = (\frac{2\pi\nu}{nc})\epsilon_2$ where c is the velocity of light and n is the refractive index. $\epsilon_2(\nu)$, the imaginary part of the dielectric constant, is a dimensionless measure of absorption. The ϵ_2

spectra, being related directly to the density of states, provide the most immediate access to these states.

2. Concept of band gap

The sharp rise in the optical absorption at a characteristic energy suggests the concept of an optical energy gap parameter E_{opt} for the crystalline semiconductor. In contrast to crystalline semiconductor, the optical absorption edge of an amorphous semiconductor is difficult to define experimentally which lead to the ambiguity in the definition of optical energy gap parameter. The optical energy gap parameter E_{opt} for amorphous semiconducting films can be extracted from the energy dependence of ϵ_2 , the imaginary part of the dielectric constant, in a variety of ways[10] depending on assumptions involving both the energy dependence of valence and conduction band densities of states near the band edges and the energy dependences of the optical matrix element. The assumption as to which optical matrix element[38-40] (momentum or dipole) is independent of energy and whether the density of states for valence and conduction band are linear or have square root dependence with energy leads to three equations.

$$\epsilon_2(E) = B_1(E - E_{opt})^2 / E^2 \qquad (3.3a)$$

$$\epsilon_2(E) = B_2(E - E_{opt})^3 / E^2 \qquad (3.3b)$$

$$\epsilon_2(E) = B_3(E - E_{opt})^2 \qquad (3.3c)$$

where B_1, B_2 and B_3 are constants. Eq. (3.3a) assumes square

root densities of states and constant average momentum matrix element. Eq.(3.3b) assumes linear densities of states and constant average momentum matrix element. Eq. (3.3c) assumes square root densities of states and constant dipole matrix element. However, there is absolutely no theoretical justification for linear or square root density of states and also for the assumption regarding the independence of matrix element (momentum or dipole) with energy.

To do away with the degree of arbitrariness in the definition of E_{opt}, the optical band gap parameter can be defined to be that energy where the absorption coefficient equals to $10^4 cm^{-1}$. Here again the theoretical justification is nonexistant.

In spite of the arbitrariness in the definition of the optical band gap, it continues to be a useful concept in the amorphous semiconductor like the traditional optical band gap of the crystalline semiconductor. Further, the utility of the optical band gap lies in understanding the electronic changes induced in the semiconductor through either structural, thermal disorder,[41] or the microstructural changes due to alloying composition[16] and annealing.[10,42]

B. Quantum Mechanical model of optical absorption in an Amorphous semiconductor

Throughout this chapter, we focus on the imaginary part of the dielectric constant $\epsilon_2(E)$. The real part $\epsilon_1(E)$ can be determined by Kramers-Kronig analysis for any theoretical model for ϵ_2. It is, however, of less experimental

interest because its spectral variations, unlike that of ϵ_2, is not directly related to the density of states within the forbidden gap of the amorphous semiconductor. The theoretical model for ϵ_2 permits us to determine the optical band gap parameters.

The optical properties of amorphous and crystalline semiconductors may be deduced almost entirely from the general one electron expression for the imaginary part of the dielectric constant[43]

$$\epsilon_2(E) = \left(\frac{2\pi e \hbar^2}{m}\right)\left(\frac{2}{VE^2}\right)\sum |P_{ou}|^2 \delta(E_o - E_u - E) \qquad (3.4)$$

In Eq. (3.4), E is the energy of the incident light wave, V is the illuminated volume of the sample and P_{ou} refers to the momentum matrix element between occupied and unoccupied states, E_o and E_u refers to the energy of the occupied and the unoccupied states. The sum is over the occupied and unoccupied single particle (one spin) electronic states, which are normalized to unity over the volume V. The factor of 2 accounts for spin conservation in transition and the spin degeneracy in the occupation.

If we define the occupied state by $|v\rangle$, a valence band eigenstate with eigenvalue E_v and unoccupied state by $|c\rangle$, a conduction band eigenstate with eigenvalue E_c, the matrix element can then be written as $|P_{v,c}|^2$ where $P_{v,c} = \langle c|\frac{\tau \cdot P}{\hbar}|v\rangle$ where τ is the polarization vector of the light wave and P is the momentum operator. The expression for $\epsilon_2(E)$ than

becomes

$$\epsilon_2(E) = \left(\frac{2\pi e\hbar^2}{m}\right)^2 \left(\frac{2}{VE^2}\right) \sum |P_{v,c}|^2 \delta(E_c - E_v - E) \qquad (3.5)$$

In a crystal, the behavior of $\epsilon_2(E)$ is set by the requirement of momentum conservation in optical transitions and by the form of electronic density of states. The first occurs because the translational symmetry of the crystal only permits nonzero momentum matrix elements when the wave vectors of initial and final states of transition are identical. The second then arises because for such vertical transitions, the momentum matrix elements vary slowly with wave vector K.[19]

In the amorphous phase, the structure again determines the behavior of the momentum matrix elements which in turn specifies the nature of transition between filled and empty states. On the whole, the development parallels the crystalline case and one obtain a different expression for $\epsilon_2(E)$ described by Eq. (3.3) which is dictated by the nature and the form of matrix element and the type of density of states.[10]

First we will focus on the Tauc model,[18] which assumes the momentum matrix element to be independent of energy and that the density of states for valence and conduction band to have square root dependence with energy. This was the first successful attempt to describe amorphous materials in the framework of crystalline materials and for introducing

the concept of band gap in amorphous material. The concept of band gap in amorphous material contributed substantially for understanding this class of materials.[10,16,41,42]

The Tauc model starts with a 'virtual' crystal into which positional disorder is introduced.[44] The virtual crystal has the same nearest and the next-nearest-neighbour bonding in the amorphous phase as in the 'real' crystal of the element or compound in question. The virtual crystal also has to simulate topological disorder. The average features of the virtual crystal, however, are closely related to the features of the real crystal.

Following Tauc, we make the following assumptions:

1) The amorphous semiconductor and its virtual crystal can be described by valence and conduction bands separated by a gap in which there is a very low density of states.

2) The valence (conduction) band wave functions for the amorphous semiconductor can be expanded in terms of the Bloch waves of the valence (conduction) band of the virtual crystal. There is no mixing of valence and conduction band wavefunctions due to positional disorder.

3) The optical matrix element, which is independent of energy, is modeled to be

$$(P_{v,c})_{cryst} = P_{k_v k_c'} = S\,\delta_{k_v k_c'} \tag{3.6}$$

where in Eq. (3.6) the notation k_v and k_c' indicate Bloch wave functions appropriate to the valence and conduction bands with momentum k_v and k_c'. The Kronecker delta symbol

describes electronic momentum conservation for the ordered virtual crystal.

We can derive from Eq. (3.5) under the above assumption an expression for ϵ_2 in the virtual crystal which describes a direct optical transition since both energy and momentum are conserved. If we add to the above assumptions the additional one that there is no conservation of electron momentum in the disordered amorphous semiconductor, we will derive an expression for ϵ_2 which describes an optical transition in which momentum is not conserved.[45] This can be described as a nondirect transition to distinguish the absorption edge of the amorphous semiconductor with positional disorder from the indirect absorption edge of crystalline semiconductors. From Eq. (3.5), we have

$$\epsilon_2(E) = \left(\frac{2\pi e\hbar^2}{m}\right)^2 \left(\frac{2}{VE^2}\right) S^2 \sum_{v,c} |\langle v|T|c\rangle|^2 \delta(E_c - E_v - E) \quad (3.7)$$

where

$$\langle v|T|c\rangle = \sum_{K_v K_c'} \langle v|K_v\rangle \delta_{K_v K_c'} \langle K_c'|c\rangle$$

If we note that the quantity T^{+} is a projection operator which takes a crystalline valence-band Bloch wavefunction and transforms it into a crystalline Bloch wave function in the conduction band with same electronic momentum, that the quantity TT^{+} is a unit operator for the crystal valence band, and that $T^{+}T$ is a unit operator for the crystal conduction band, we can define a sum rule due to Velicky[18]

$$\sum_{v,c} |\langle v|T|c\rangle|^2 = \sum_{v} \langle v|TT^{+}|v\rangle = \sum_{v} 1 = N_o \quad (3.8)$$

The quantity N_o is the number of single spin states in the valence (conduction) band. The number of electrons that can occupy these states is $2N_o$.

If we replace the quantity $|\langle v|T|c\rangle|^2$ by a constant T_o^2 then from the sum rule defined by Eq. (3.8) we get $T_o^2 = 1/N_o$ and the Eq. (3.7) becomes

$$\epsilon_2(E) = \left(\frac{2\pi e\hbar^2}{m}\right)^2\left(\frac{2}{VE^2}\right) S^2\left(\frac{1}{N_o}\right)\sum_{v,c}\delta(E_c - E_v - E) \tag{3.9}$$

The Eq. (3.9) can be written as

$$\epsilon_2(E) = \left(\frac{2\pi e\hbar^2}{m}\right)^2\left(\frac{2}{VE^2}\right) S^2\left(\frac{V^2}{N_o}\right)\int dz\; N_c(z) N_v(z-E) \tag{3.10}$$

where z is a parameter and

$$\begin{aligned}\sum_c \delta(E_c - z) &= V N_c(z)\\ \sum_v \delta\{E_v - (z-E)\} &= V N_v(z-E)\end{aligned} \tag{3.11}$$

defines the volume density of single spin states for the conduction band and valence band respectively. Again, V is the illuminated volume of the sample to which all wave functions have been normalized. If the density of states are given by $N_c(z) = const\,(z - E_A)^s$ and $N_v(z) = const\,(E_B - z)^p$

then from the Eq. (3.10), that describes a nondirect optical transition, we get

$$E^2\epsilon_2(E) = \left(\frac{2\pi e\hbar^2}{m}\right)^2 S^2\left(\frac{2V}{N_o}\right)(const)\frac{\Gamma(s+1)\,\Gamma(p+1)}{\Gamma(s+p+2)}\left(E - E_{opt}\right)^{s+p+1} \tag{3.12}$$

Depending upon the density of states to be parabolic (s=1/2 and p=1/2) or linear (s=1 and p=1), we obtain from Eq.(3.12)

$$E^2\epsilon_2(E) = B_1(E - E_{opt})^2 \tag{3.13}$$

$$E^2\epsilon_2(E) = B_2(E - E_{opt})^3 \tag{3.14}$$

where B_1 and B_2 are constants and Γ are the Gamma Functions.

Thus assuming constant average momentum matrix element and assuming square root and linear densities of states we reproduce Eqs. (3.3a) and (3.3b) from Eq. (3.12)

From the general relation between momentum operator P and its conjugate coordinate R, we have $P = \frac{im}{\hbar}[H,R]$ where H is the Hamiltonian of the system. We can rewrite Eq. (3.5) in the equivalent form within one electron approximation as

$$\epsilon_2(E) = (2\pi e)^2\left(\frac{2}{V}\right)\sum_{v,c}|R_{v,c}|^2\,\delta(E_c - E_v - E) \qquad (3.15)$$

where R is the dipole matrix element.

We now assume the dipole matrix element to be independent of energy and model it to be

$$(R_{v,c}) = R_{K_v K_c'} = Q\,\delta_{K_v K_c'}$$

Assuming square root dependence of density of state and carrying out the same analysis as outlined above, we obtain from Eq. (3.15)

$$\epsilon_2(E) = (2\pi e)^2\left(\frac{2}{V}\right)Q^2\left(\frac{2V}{N_0}\right)(const)\frac{\Gamma(3/2)\,\Gamma(3/2)}{\Gamma(3)}(E - E_{opt})^2 \qquad (3.16)$$

If we replace the cofficient of $(E-E_{opt})^2$ by a constant B_3 then the Eq. (3.16) becomes

$$\epsilon_2(E) = B_3(E - E_{opt})^2 \qquad (3.17)$$

Thus assuming square root density of states and constant dipole matrix element we obtain Eq. (3.3c).

C. Expressions for getting n, k, d from R_a, T, R_s

The determination of real ϵ_1 and imaginary ϵ_2 parts of the dielectric constant of the film involves the knowledge of real(n) and imaginary (k) parts of the refractive index

as they are related by $\epsilon_1 = n^2 - k^2$, $\epsilon_2 = 2nk$. The real and imaginary part of the refractive index and the thickness (d) of the film can be extracted from the measured reflectance and transmittance of the film. The expressions for transmittance and reflectance (both from air and substrate side) is given in this section and the procedure for determining n, k, d using the expressions for transmittance and reflectance along with the measured transmittance and reflectance will be described in the next section.

Explict, single expressions for the reflectance and transmittance of the system of many films are cumbersome and are depressingly complicated. The extraction of parameters from the equations involves tedious computation. This problem is tackled by using matrix method using Fresnel cofficient.

For the derivation of expressions for reflectance from film (R_a) and substrate (R_s) side and the transmittance (T) as a function of n, k, d and wavelength λ, the method of Abeles[46] is made use of. The method consists in establishing the relations between the electric vectors of successive layers in terms of Fresnel cofficients. For this purpose the films are assumed to be homogeneous, isotropic and the case of normal incidence is considered to duplicate the experimental situation (see Fig. 3.1).

The explicit expressions[47] for the reflectance and the transmittance of an absorbing film, like our hydrogenated

amorphous silicon carbon alloy, of $\tilde{n}_1 = n_1 - ik_1$ on a transparent substrate of refractive index n_2 are given below. The film as well as the substrate are in contact with air. The expressions for the reflectance from the film side (R_a), the transmittance (T) and the reflectance from substrate side (R_s), including the interference effects, are given by

$$R_a = \frac{tu13}{pv13}$$

$$T = \frac{lm13}{pv13} \qquad (3.18)$$

$$R_s = \frac{trp2}{pv13}$$

where

$$pv13 = \beta + [(g_2^2+h_2^2)(g_1^2+h_1^2)]/\beta + 2g_1(g_2c_1+h_2s_1) + 2h_1(g_2s_1-h_2c_1) + g_3^2[\beta(g_2^2+h_2^2) + (g_1^2+h_1^2)/\beta + 2g_1(g_2c_1-h_2s_1) + 2h_1(h_2c_1+g_2s_1)]$$

$$tu13 = (g_2^2+h_2^2)/\beta + (g_1^2+h_1^2)\beta + 2g_1(g_2c_1+h_2s_1) + 2h_1(h_2c_1-g_2s_1) + g_3^2[\tfrac{1}{\beta} + (g_1^2+h_1^2)(g_2^2+h_2^2)\beta + 2g_1(g_2c_1-h_2s_1) - 2h_1(h_2c_1+g_2s_1)]$$

$$lm13 = [\{(1+g_1^2)+h_1^2\}\{(1+g_2)^2+h_2^2\}\{(1+g_3)^2\}]$$

$$trp2 = \beta[(g_2^2+h_2^2)+g_3^2] + (g_1^2+h_1^2)[1+(g_2^2+h_2^2)g_3^2]/\beta + 2g_2(1+g_3^2)(g_1c_1+h_1s_1) - 2h_2(1-g_3^2)(g_1s_1-h_1c_1)$$

and

$$g_1 = \frac{(1-n_1^2-k_1^2)}{(1+n_1)^2+k_1^2}$$

$$h_1 = \frac{2k_1}{(1+n_1)^2+k_1^2}$$

$$g_2 = \frac{n_1^2-n_2^2+k_1^2}{(n_1+n_2)^2+k_1^2}$$

$$h_2 = \frac{-2n_2k_1}{(n_1+n_2)^2+k_1^2}$$

$$g_3 = \frac{n_2^2-1}{(n_2+1)^2}$$

$$a_1 = \frac{2\pi\kappa_1 d}{\lambda}$$

$$b_1 = \frac{2\pi n_1 d}{\lambda}$$

$$b_2 = \frac{2\pi n_2 D}{\lambda}$$

$$\beta = \exp(2a_1)$$

$$C_1 = \cos(2b_1)$$

$$S_1 = \sin(2b_1)$$

D. Effective Medium Approximation (EMA)

The optical properties of the random heterogeneous composite films are described by a spatially-varying dielectric constant $\epsilon(r,w)$ where r is the coordinate vector and w is the frequency. When the spatial variations of $\epsilon(r,w)$ are much smaller than the wavelength of light, but large enough to have "bulklike" dielectric properties then the composite can be characterized by a macroscopic dielectric constant $\epsilon(w)$. The calculation of $\epsilon(w)$ from $\epsilon(r,w)$ is a forbidding mathematical problem. The approximate solutions to the integral equation from which $\epsilon(w)$ are obtained by neglecting multiple scattering of the electric field by the grains of the components.[48] This approximation is equivalent to a mean field theory in which the effect of all the grains on a given grain is represented by a uniform field. Two well-known approximations are the effective medium theory[49,50] and the Maxwell-Garnett theory.[51]

In the effective medium theory the components are

treated in an equivalent manner. Grains of the components are embedded in an effective medium whose dielectric constant ϵ is the same as that of the composite material. On the other hand, in the Maxwell-Garnett theory it is assumed that the grains of one component are embedded in the matrix of the other component. This theory, unlike the effective medium theory, treats the two components in an asymmetric manner. Recent treatments[52,53] have attempted to understand their differences more fundamentally in terms of microstructure of the composite materials. These investigations showed that the Maxwell Garnett result follows from a coated sphere (cermet) configuration, where one component is completely surrounded by another component. The Bruggemann expression follows from an aggregate model, where the components are mixed on a random basis.

We choose to use the EMA for hydrogenated silicon carbon alloy because the scale of the heterogeneity in the film (i.e the dimensions of the distinct regions corresponding to the various components) is much smaller than the wavelength of light in the medium, yet large enough compared to the lattice constant so that the individual components have "bulk-like" dielectric properties. Also, it treats the components on an equal basis. Further, the EMA has previously been shown to be applicable both to hydrogenated amorphous carbon film (a-C:H)[15] and also to $Si-SiO_2$ and $Si-Si_3N_4$ mixtures.[17] The EMA expression for ϵ,

the complex dielectric function of the composite medium, is given by

$$\sum_i v_i \frac{\epsilon_i - \epsilon}{\epsilon_i + 2\epsilon} = 0 \qquad (3.19)$$
$$\sum_i v_i = 1$$

where v_i and ϵ_i are the volume fraction and complex dielectric function of component i, respectively.

E. Microstructural Model

To model the dielectric response, a microstructural model[16] is proposed, which assumes the alloy film to be macroscopically homogeneous but microscopically heterogeneous. For this purpose the EMA expression of Eq. (3.19) along with the expression $\sum \rho_i v_i = \rho_{exp}$ is used, where ρ_i and ρ_{exp} are the density of the ith component and of the composite respectively. The components of the composite are proposed to be void, amorphous polymeric, amorphous graphitic and amorphous tetrahedral, each with its own dielectric response. The volume fractions of the components are v_v, v_{ap}, v_{ag} and v_{at} respectively.

In order to apply the EMA expressed in Eq. (3.19) to our measured ϵ_1 and ϵ_2 spectra so that the volume fractions v_i of the proposed components can be obtained, we first need ϵ_i spectra of the individual components. For the void component we have used ϵ_1=1 and ϵ_2= 0 . For the polymeric component, smoothed ϵ_1 and ϵ_2 spectra of polyethylene[54] with a density of 0.92 gm/cm^3 are used. For the amorphous graphitic component, measured ϵ_1 and ϵ_2 spectra for an a-C:H

film[15] annealed at 500°C, with a measured density of 1.47 gm/cm^3, are used. The dielectric response of this annealed a-C:H film is believed to reflect more accurately the localized nature of the graphitic π-like electrons than did the evaporated C film previously used.[15]

For the amorphous tetrahedral component, a Si- and C-centered tetrahedron model[55] has been developed to predict the optical constants ϵ_1 and ϵ_2 of the tetrahedral component as a function of the Si/C ratio by applying the approach of Aspnes and Theeten[17] to the hydrogenated silicon carbon alloy system. The approach of Aspnes and Theeten, in essence, has combined the Si centered tetrahedral model of Philipp[56] with composite media theory. The predicted ϵ_1 and ϵ_2 spectra for the tetrahedral component have been obtained by scaling from our ϵ_1 and ϵ_2 data for a-Si:H, and as a result, the dielectric response of the amorphous tetrahedral component can be considered to reflect the contribution of approximately 10 at % hydrogen. The details of finding ϵ_1 and ϵ_2 of the tetrahedral component are given in the Appendix I

F. Infrared Absorption

There is much interest in finding the microscopic bonding configurations of hydrogen in the amorphous network because the bonded hydrogen in a-Si was a significant factor in transforming a-Si to a new optoelectronic material[22] a-Si:H. The prime method used to investigate the

local bonding configuration has been the infrared absorption. The frequency of a fundamental infrared absorption mode depends on both the mass of the oscillating dipole and the strength of the bond between the atoms comprising the dipole. The wavenumber of the oscillator depends upon the mass of the atoms.

$$\nu(cm^{-1}) = \frac{1}{2\pi c}\left[K\left(\frac{1}{m_1}+\frac{1}{m_2}\right)\right] \qquad (3.20)$$

where ν is the wavenumber of the oscillator in cm^{-1}, c is the speed of light, K is the force constant directly related to bond strength, and m_1 and m_2 are the masses of the vibrating atoms.

The infrared spectra of $a\text{-}Si_{1-x}C_x:H$ exhibit rich structure[12] in four main absorption regions in the range from 400-4000 cm^{-1} (described earlier). The number of bonds of Si-H, C-H, Si-C, Si-O are proportional to the intensity of the integrated absorption of Si-H, C-H, Si-C, Si-O stretching modes, respectively. The proportionality constant represents the cross section of the above said stretch modes. The theory and the procedure of determining the cross sections of these modes will be discussed in turn:

1. Cross section of Si-H Stretch

The density of Si-H bonds, N_{Si-H}, is proportional to the integrated intensity of Si-H stretch (I_{Si-H}) and is given by

$$N_{Si-H} = A_S I_{Si-H} \qquad (3.21)$$

The proportionality constant A_S, which is the cross section

of Si-H stretch, is determined as follows:

$$I_{Si-H} = \int \frac{\alpha(\omega)}{\omega} d\omega = \frac{2.303}{\langle\omega\rangle d} \int A(\nu) d\nu \quad (3.22)$$

where $\langle\nu\rangle$ is the wave number at which Si-H stretch is peaked and $A(\nu)$ is the absorbance at wave number v and d is the thickness of the film.

Following Shanks et al[57] and Fang et al[58] the cross section used for Si-H stretch is $1.4\times10^{20}cm^{-2}$. The cross section[57,58] is determined by measuring hydrogen concentration and the integrated absorption under Si-H stretch peak. The hydrogen concentration of the sample is measured using the (n,p) reaction.[58] This gives the absolute hydrogen content of the films which has been recalculated in terms of a relative hydrogen concentration C_H using the atomic density of crystalline silicon ($5\times10^{22}cm^{-3}$). The integrated strength of Si-H stretching band I_{Si-H} is plotted versus C_H. The relationship between I_{Si-H} and C_H is approximated by a straight line and the proportionality constant, which is the Si-H cross section, is calculated to be $1.4\times10^{20}cm^{-2}$.

2. Cross section of C-H Stretch

The cross section for C-H mode is taken to be $(1.35 \pm 0.35)\times10^{21}cm^{-2}$, which is an average of the results of $1.7\times10^{21}cm^{-2}$ and $1.0\times10^{21}cm^{-2}$ given by Nakazawa et al[59] and Fujimoto et al[60] respectively. The density of C-H bonds (N_{C-H}) is proportional to the integrated intensity of C-H stretch (I_{C-H}) and is given by

$$N_{C-H}=A_C I_{C-H} \quad (3.23)$$

The proportionality constant A_C, which represents the cross section for C-H stretch mode, is determined[59] by combining the results of the NMR and IR measurement as follows. The hydrogen, whose total amount is determined by NMR measurement, is assumed to be bonded to either Si or C in a-$Si_{1-x}C_x$:H. The number of H bonded to Si is estimated using the cross section of Si-H . Thus, the number of H bonded to C, N_{C-H} is obtained by subtracting N_{Si-H} from the total amount of H determined by NMR. N_{C-H} thus determined is plotted against the absorption intensity of the CH_n stretching mode. A roughly linear relationship is obtained between them, and proportionality constant is given as $A_C=1.7\times10^{21}cm^{-2}$ by averaging the slopes of lines connecting data points to the zero point.

3. Cross section of Si-C Stretch

The intensity of the integrated absorption of Si-C stretch I_{Si-C} is related to the number of Si-C bonds N_{Si-C} by the relation.

$$N_{Si-C}=B_S I_{Si-C} \tag{3.24}$$

The proportionality constant B_S represents the cross section for Si-C stretch mode. However, the proportionality constant B_S between the number of Si-C bonds and integrated intensity of IR absorption is determined to be 2.13×10^{19} cm^{-2} which is as follows. $N_{Si-C}= B_s \int \frac{\alpha(\omega)}{\omega} d\omega$

$$\text{But } \int \frac{\alpha(\omega)}{\omega} d\omega = \frac{2.303}{\langle\nu\rangle d} \int A(\nu)\, d\nu$$

Following Mogab[61], we write absorbance $A(\nu)$ to be

$$A(\nu) = \log\left[1 + \frac{C}{(1-\nu/\langle\nu\rangle)^2 + (\gamma/2)^2}\right] \quad (3.25)$$

where $C = \pi^2 \rho\left[2\gamma\langle\nu\rangle d + 4\pi^2\rho(\langle\nu\rangle d)^2\right]$

and ν is the wave number of the incident radiation, $\langle\nu\rangle$ is the wave number at which Si-C stretch is peaked for cubic SiC crystal, d is the thickness of the film, γ is the dimensionless damping constant and ρ is the dimensionless parameter reflecting the strength of absorption and is related to the static (low frequency) dielectric constant, ϵ_0 and high frequency dielectric constant ϵ_∞ as $P=(\epsilon_0-\epsilon_\infty)/4\pi$. We get

$$\int\frac{\alpha(\omega)}{\omega}d\omega = \frac{1}{\langle\nu\rangle d}\int_{-\infty}^{\infty}\ln\left[1 + \frac{C}{(1-\nu/\langle\nu\rangle)^2 + (\gamma/2)^2}\right]d\nu \quad (3.26)$$

Using the value of C and carrying out the integration and neglecting higher order terms in ρ we obtain, $\int\frac{\alpha(\omega)}{\omega}d\omega = 4\pi^3\rho\langle\nu\rangle$

$$N_{Si-C} = 4\pi^3 B_S \rho\langle\nu\rangle \quad (3.27)$$

The number of Si-C bonds per cm^3 N_{Si-C} is calculated for cubic SiC crystal to be 5.52×10^{23}. Using the value of $P=0.263$ and $\langle\nu\rangle=793 cm^{-1}$ for cubic SiC crystal as given by Mogab[61] and using the above equation we obtain $B_S=2.13\times10^{19}$ cm^{-2}

4. Cross section of Si-O Stretch

The intensity of the integrated absorption of Si-O stretch I_{Si-O} is related to the number of Si-O bonds N_{Si-O} by the relation

$$N_{Si-O} = B_o\int\frac{\alpha(\omega)}{\omega}d\omega \quad (3.28)$$

where B_O is the cross section for Si-O stretch mode. Carrying out the same analysis as we have done for Si-C we obtain

$$N_{Si-O} = 4\pi^3 B_o P \langle \nu \rangle \tag{3.29}$$

where P is the dimensionless parameter reflecting the strength of absorption for Si-O stretch and $\langle \nu \rangle$ is the wave number at which Si-O stretch is peaked for SiO_2 crystal. The number of Si-O bonds N_{Si-O} is calculated to be $10.62 \times 10^{22} cm^{-3}$ for SiO_2 crystal. Using the value of $P=0.0533$ and $\langle v \rangle = 1072 cm^{-1}$ for SiO_2 as given by Spitzer[62] and using the above equation we obtain $B_O = 1.5 \times 10^{19} cm^{-2}$.

CHAPTER IV

EXPERIMENTAL PROCEDURE

A.Experimental Apparatus

1. Description of Glow Discharge Technique

There are many ways to prepare amorphous films, some of which are 1) Glow discharge plasma deposition, 2) Reactive sputtering, and 3) Pyrolytic decomposition of gases which is known as Chemical Vapour Deposition (CVD). The glow discharge technique has attracted the most attention in recent years mainly because (1) this technique was used in the first successful doping experiments[22] on amorphous silicon, and (2) the early work suggested that a-Si:H films produced by this technique have better optoelectronic properties than films produced by other techniques.

Glow discharge is a type of electrical discharge where an rf or dc electric field is used to generate a weakly-ionized plasma. The electron and ion densities in the plasma at a typical pressure of 0.1 Torr are of the order of $10^{10} cm^{-3}$. The electron temperature may be 10 to 100 times that of the ions so that the electrons possess sufficient energy (1-10 eV) to break molecular bonds to produce ions and chemically active neutral species in the ground state and the excited state. The reactive species of the gas (SiH_4) for a-Si and (SiH_4, GeH_4, C_2H_4) for alloys condense on a heated substrate to produce amorphous films still rich in hydrogen.

Discharge-produced amorphous silicon, currently referred to as hydrogenated amorphous silicon (a-Si:H), is known to contain typically 5 to 40 at % hydrogen. Discharge produced amorphous silicon alloy films contain silicon, hydrogen, and alloying elements like carbon or germanium. The materials produced by the rf glow discharge technique have certain intrinsic advantages over the other techniques:
1) The materials like a-Si and its alloy produced by glow-discharge have remarkably good semiconductor qualities like continuously adjustable band gap, a usable carrier lifetime and diffusion length , efficient optical transitions, and the capability of employing either n- or p- type dopants. This is due to the low density of dangling bonds, passivated by hydrogen, and the correspondingly low density of localized states in the gap.[63]
2) The hot electrons in the plasma of glow discharge lower the temperature of the reaction compared to conventional CVD. This facilitates the use of a lower substrate temperature. Use of lower substrate temperature can prevent the bonded hydrogen from being thermally emitted into the gas phase from the film as encountered in CVD technique. This make the density of dangling bonds quite low compared to CVD films prepared under similar conditions.
3) The operating frequency of rf glow discharge is usually 13.56 MHz. At this high frequency the electrons oscillating in the glow space acquire sufficient energy to

cause ionizing collisions which reduces the breakdown voltage. Also as the operating frequency increases, the minimum operating pressure begins to fall, reaching values of less than 1 mTorr at 13.56 MHz. Another manifestation of the same effect is that, for a given pressure, the impedance of a discharge decreases with increasing frequency, so that one can drive more current through the discharge with a given voltage. This makes it possible to operate the system at low rf voltages.

4) Uniform films can be deposited on any substrate (insulator and conductor) over large areas.

Disadvantages associated with the rf glow discharge technique include:

1) The deposition rates are very low (1 to 10 Å/sec). This is acceptable at the laboratory level but for large scale applications, high deposition rates are required to achieve the high throughput.

2) As a deposition process, the glow discharge technique is inferior to reactive sputtering for the following reason. By reactively sputtering c-Si in an Ar and H atmosphere, hydrogenated amorphous silicon is produced. The two source materials Si and H can be uncoupled and independently optimized in relation to the role each plays in forming the network. This type of control is not possible in glow discharge decomposition because the source materials are initially chemically bonded in the feed gas.

2. Description of Glow Discharge Chamber

The samples studied here were prepared using a rf glow discharge apparatus (see Fig.4.1). The configuration is that of a flow through device, i.e. a continuous flow of reactant gases is passed through the region of discharge from the top and the pressure is measured by Baratron capacitance vacuum gauge. It was found previously[64] that maintainence of such a flow reduced the chances of building up of the contaminants such as the radicals of the reactive gases within the reactant gas during a discharge. The pumping of the discharge chamber is accomplished by two systems. For preliminary pumpdowns a Veeco VS-9 pumping station, containing a diffusion and a fore pump, is used. Its two inch air cooled diffusion pump is capable of achieving final pressures of the order of 10^{-7} Torr. Pumping during the discharge involving reactive gases, to be described later in detail, is accomplished via a separate neutralization and disposal system (see Fig.4.5). Use of such a system is necessitated by the presence of explosive gas like silane.

The plasma reactor for the deposition of the film is a parallel-plate system in which the discharge is generated between two parallel disk copper electrodes, the power electrode and unpowered sample electrode (see Fig.4.1). The two electrodes are separated by 2 inches, and have diameters of 3 inches. The electrodes are shielded from the plasma

except for their front surfaces by encircling them with the grounded plasma shield made up of stainless steel (see Fig.4.3). To generate the plasma in this flow through device, the rf power (5 to 15 Watt) at 13.56 MHz is capacitively-coupled to the power electrode through an rf matching network from model HF-300 rf power supply of eni power system, Inc. The 'Heathkit' matching network consists of two variable capacitors and a variable inductor. The purpose of this matching network is to increase the power dissipation and to reduce reflected power in the discharge.

The potentials[65] that are of importance in an rf glow discharge are 1) the plasma potential V_p, 2) the floating potential V_f 3) and the sheath potential V_s also called the d.c potential. The spatial distribution of the average potential in a parallel plate rf reactor is shown in Fig.4.2. The plasma potential V_p is the potential of the glowing part of the discharge and is the most positive potential anywhere in the reactor. The potential V_p is at least as large as the first ionization potential of the gas, with respect to the grounded electrode in contact with the glow discharge, and it is regarded as the reference potential of the system. The ground potential is always negative with respect to the plasma, and hence the substrate surface on the grounded electrode should more or less suffer the positive ion bombardment. The potential on the powered electrode is also negative with respect to the plasma

potential. This is because when an external body (power electrode) is immersed in a plasma, it self biases negatively due to the large difference in the ion and electron mobilities. When the rf voltage is applied to the power electrode, it results in a large electron current during one-half of the cycle and a small ion current on the other half of the cycle. The large electron current is due to the high mobility of the electrons. The negative potential so built up repels the electrons and attracts the ions and ultimately the external body reaches a dynamic equilibrium with the plasma with potential V_f (floating potential) such that the current due to electrons and ions are equal so that the net current is zero. Near the wall of the external body there is a boundary layer in which the potential increases monotonically from negative value on the wall of the external body to unperturbed plasma. This potential is the sheath potential. The sheath potential V_s, being equal to V_f+V_p on the powered electrode, accelerates ions that enter the sheath, and the electrode surface is bombarded. In the standard parallel-plate electrode plasma reactor powered with an rf source, the substrate is placed on the grounded electrode to reduce the influence of the ion bombardment. However, the plasma potential is still important to determine the energy of ions impinging onto the substrate surface.

3. Description of the sample electrode

The sample electrode (see Fig.4.3), consists of a heatable copper block with a recessed chromel-alumel thermocouple, isolated electrically by a ceramic tube, placed just below the sample substrate for temperature measurement. This copper block is placed on the substrate heater constructed of Macor, a Dow Corning ceramic, with heat supplied by the ohmic heating of an ARI heater in the form of a spiral, sandwiched between the Macor pieces. Macor is well suited to such applications as it is a machinable, non-porous insulator that conducts heat and is stable upto 1000°C, sufficent for this application. The sample substrates are mounted on the grounded, unpowered electrode (copper block). The sample substrates are polished clear fused quartz for optical constants measurement, oxygen free high conductivity (OFHC) copper for dencity and composition measurements, and intrinsic Si for infrared studies (resistivity of 2500 ohm cm, polished both sides). The dimensions of the sample substrates are typically (0.75", 0.5", 0.02"). The substrates are mounted on the grounded electrode because the powered rf electrode is selfbiased and suffers ion bombardment, which may deteriorate the film quality. For minimizing such bombardment, the applied rf power is kept as low as possible (5 to 10 Watt). The whole assembly is shielded from the plasma except for their front surfaces by encircling them by

grounded plasma shields made up of stainless steel.

4. Gas mixing and flow control system

Gas mixing and flow control are provided by a gas handling system, a schematic of which appears in Fig. 4.4 . The system can provide three gases at a time. In the first phase of the experiments the gases are argon (99.9%) commercial grade acetylene (C_2H_2, 96.6% purity, Linde) and silane (SiH_4, diluted to 10.2% in argon, Linde). In the second phase of the experiment the gases are argon (99.9%), ethylene (C_2H_4) and 100 % silane electronic grade. All system components are constructed of materials rated for corrosive service. Flow control for the system is provided by an electronic mass flow controller. Provision has also been made for the purging of the system with an inert gas (Ar) before and after use, as corrosive and reactive compounds may be formed. The key fact to realize is that the bulk of the gas absorbed on the system walls while exposed to the laboratory environment is water vapor. This necessitates the provision for the baking of the vacuum system to remove the surface contaminants such as water vapor.

5. Gas neutralization and disposal system

The schematic of gas neutralization and disposal system is given in Fig. 4.5. The gas neutralization and disposal system will be described in two sections. The first section corresponds to the initial phase when silane diluted with

argon was used and only a rotary vane pump was used for pumping the waste gases. The second section corresponds to final version, where we have used pure silane and have enhanced the pumping speed by incorporating a Roots pump (WS150 LH) in conjunction with rotary vane pump (Trivac D8AC) to prepare high quality film. The Roots pump consists of two identical impellers that rotate in opposite direction. The high speed of rotation leads to large volumetric efficiency. The Root pumps have maximum pumping speed in 10^{-2} to 1 Torr range and falls off above and below this range. Further, an electronically controlled exhaust valve was incorporated into the system in the final phase for precise control of pressure.

Neutralization of the reactive gas like SiH_4 during its flow through the system is accomplished via both pyrolysis at 750^oC in a mullite furnace tube as well as by bubbling the gas through a neutralizing solution. At the very outset the gases from the reaction chamber are broken down to smaller radicals by pyrolysis at 750° in a mullite furnance tube. Quartz wool is placed in the path of the gas to reduce the mean free path of the molecules, and thereby increasing the probability of neutralization. The gases are diluted with nitrogen and passed through a scrubber, containing the neutralizing solution like NaOH. In the scrubber the bubbles are formed by the nitrogen gas and the radicals of the reactive gas like SiH_4 are neutralized and

finally the gases are passed to the hood through the mechanical pump (Trivac D8AC). Though pyrolysis should completely decompose the gas, the bubbling process serves as a backup in the event of oven failure or powerloss, as the bubbles would continue to function in either case.

The use of pure silane led to mechanical pump seizures which led us to have a more elaborate neutralization and disposal procedure. The seizure may be due to particulates within the pump or to formation of tar like substances by decomposition of oil. Procedures as outlined[66] have been followed to minimize the occurrence of seizures.

Due to large clearance, any oil entering the Roots pump exhaust from the mechanical pump can find its way into Roots pump inlet by creep. Thus the usual cautions must be observed to minimize oil backstreaming from the mechanical pump.[67] This can prevent particulate matter from adhering to the impellers, and will avoid varnish like deposits on the impellers in the presence of explosive gas like silane. To prevent oil backstreaming we introduce nitrogen to a pressure of 100 to 150 mTorr between the Roots pump and the mechanical pump. When the Roots pump is at blank-off, the inlet pressure of the Roots pump increases slightly, but the oil from the mechanical pump can not enter the exhaust of the Roots pump.

B. Substrate preparation:

Substrates utilized in these experiments are varied according to the analysis technique to be applied. The quartz substrates (0.75", 0.50", 0.02"), used for optical measurements, are cleaned by boiling them in Transene for 10 to 15 minutes, then rinsed in triple distilled, deionized water after which they are blown dry with nitrogen gas. The silicon substrates, used for infrared measurements, are also cleaned in the same manner as the quartz substrate. The copper substrates, used for density and composition measurements, are cleaned by dipping them in concentrated nitric acid diluted with water and then rinsed in triple distilled, deionized water and are finally blown dry with nitrogen after rinsing.

C. Sample preparation:

Once the substrates are prepared as described in the preceding section, they are mounted on the face of the sample electrode. The sample electrode is then mounted in the deposition system. The fore pump of VS-9 pump station is used for rough pump down and then the diffusion pump is used to pump down the system (G.D chamber and GHS). The system is pumped down overnight to the final pressure of about 2×10^{-7} Torr with liquid nitrogen in cold trap. The substrate is heated to the stable desired temperature. The system is baked out for about 45 minutes to remove any surface contaminant like water vapor.

The gas mixing system is isolated and the two gases like silane diluted with argon and acetylene in the first phase and silane and ethylene in the final phase are used for making hydrogenated amorphous silicon-carbon alloy films. By varing the gas ratio, the composition of carbon and silicon can be varied to any desired value. To reduce the risk of back diffusion of contaminants into the cylinder, the valve is first opened and closed, thus pressurizing the regulator. This enables the gas to be drawn to the mixing chamber from the high pressure side of the regulator with the valve closed.

Prior to the film deposition, the argon discharge is carried out for about 5 minutes to clean the substrate by bombardment due to argon ions. After this cleaning, the system is pumped to approximately 2×10^{-7} Torr. Once the mixing and the argon discharge are over the next step is to run the discharge to deposit the film.

By closing the gate valve, the Veeco VS-9 pump station was isolated, and by opening the backing pump, Roots pump and the exhaust control valve the gas disposal system was put into operation. The toggle valve for nitrogen gas to scrubber was opened. The valve separating the mixing system from the discharge chamber was opened. A stable pressure of 0.15 Torr with a flow rate of 1 sccm (cubic centimeters per minute at standard temperature and pressure) in the first phase and a stable pressure of 0.075 Torr with a flow rate

of 20 sccm in the final phase, was established. The rf power was set to the desired value of 15 Watt in the first phase and 5 Watt in the final phase. The discharge was turned on and kept on for the desired time, typically between few minutes to few hours depending on the thickness requirement. These deposition times resulted in the films ranging from several hundred angstroms to several thousand angstrom thick.

Upon completion of the discharge, the rf power and the substrate heater were turned off. The entire contents of the gas mixing system were then pumped out via the gas disposal system, and the entire system was purged with argon. Closing the exhaust control valve, the system was then pumped below 10^{-6} Torr, and the gas mixing system was sealed off, leaving it under vacuum when not in use. The Roots pump and the backing pump were flushed with nitrogen. After this, the pumps were turned off and filled with nitrogen at atmospheric pressure. When the substrate was cooled below $50^{o}C$, the gate valve of the GD chamber was closed and the GD chamber was filled with nitrogen to minimize the adsorption of water vapor on the system walls during its exposure to the laboratory environment.

D. Analysis procedure

1. Composition

Film compositions have been determined from Auger spectra which were obtained using a Perkin Elmer Corp.

Electronics Division PHI 600 scanning Auger Microprobe. All Auger spectra were measured with a primary electron beam energy of 3KeV, an electron beam of diameter of 400 nm, and on electron beam current, measured at the sample, of 35nA. The depth profile of Si, C, and Cu in each film was obtained by sputtering using a 3KeV Ar ion beam. The vacuum chamber pressure was $1x10^{-8}$ Torr during sputtering.

For composition measurement the films are deposited on a OFHC copper to do away with the problem of charging due to an impinging beam of electrons on a non-conductor. This is because charging and the instability of the charged surface prevent a meaningful Auger spectrum. The atomic fractional concentrations, F_x of Si, C, and Cu are calculated using Eq. (4.1).

$$F_x = (I_x/S_x)/(\sum_n I_n/S_n) \qquad (4.1)$$

where I_x is the Auger peak-to-peak intensity after a five-point differentiation of data collected in a 20eV electron kinetic energy region about the peak energy for each element, S_x is the Auger sensitivity factor for each element at 3KeV and n sums over the three elements C, Si and Cu. Standard values for the Auger sensitivity factors were used.[68] After subtracting the baseline atomic fractions of Si and C observed in the substrates from the values observed in the films, the resulting values, f(Si) and f(C), are normalized to their sum to obtain the Si and C fractional concentrations.

2. Density measurement

Film density (ρ) measurements are undertaken using the flotation method. The films had been removed by dissolving the OFHC copper substrates in concentrated ferric chloride solution. For film densities $\rho<1.5$ gm/cm^3, mixtures of carbon tetrachloride and ethanol are used, while solutions of zinc bromide in water are used for higher densities. The typical uncertainty in the measurement of ρ is 2 to 4%.

3. Infrared Absorption

The films deposited on intrinsic silicon, with resistivity 2500 ohm cm and polished on both sides, are used for the infrared absorption studies. These are carried out in Digilab 50 FTIR spectrophotometer in the range 400 to 4000 cm^{-1}. The FTIR spectrum of the intrinsic silicon is recorded and stored and is subtracted from the FTIR spectrum of the film on silicon. The FTIR spectra of these films show rich structure[12] (different IR modes) ranging from 400 to 4000 cm^{-1} in four absorption regions (described previously).

Estimates of the bonded hydrogen contents of the films are obtained from the integrated absorbances of the carbon-hydrogen and silicon-hydrogen infrared stretching modes using the cross sections described in the previous chapter.

To find the hydrogen atomic concentration for the a-C:H film, the cross section of C-H stretch used is $(1.35 \pm 0.35) \times 10^{21}$cm^{-2}. The measured film density is used to

determine the total hydrogen atomic percentage.

Similarly for the a-Si:H film, the cross section of Si-H stretch used is 1.4×10^{20} cm^{-2} and the measured density of silicon film is used to determine the total hydrogen atomic percentage. For the a-$Si_{1-x}C_x$:H film with 50 % carbon determined by Auger microprobe, the cross sections of Si-H and C-H stretch as mentioned above are used. To determine the total hydrogen atomic percentage, equal density of carbon and silicon atoms in the film is assumed and the measured film density is used.

4. Optical constants measurement

For the optical constants measurement the film deposited on the fused quartz is used. The transmission as well as the reflectances from both air (R_a) and substrate (R_s) sides of the film are measured. These measurements are carried out on a Perkin Elmer Lambda 3 spectrophotometer in the range 2550 Å to 8950 Å. A specular reflectance accessory calibrated using NBS SRM 2023 specular reflectance standard is employed for the determination of R_a and R_s.

For the determination of the values of n, k and d (film thickness) from the measured T, R_a, R_s (see Fig. 4.6) we have employed a computer fitting procedure based on the theory[47] as outlined in previous chapter for the exact amplitudes of the reflected and transmitted waves in the films, including the effects of interference. The fitting procedure used for determining the correct film thickness d, and simultaneously

n and k, is similar to that outlined by Nagendra and Thutupalli.[69] We have, however, used the exact expressions for transmission and reflectance T, R_a, R_s, including the effect of interference[47] as described in the previous chapter. This procedure employs the two dimensional Newton-Raphson technique for the determination of the set of values n and k which, for a given d and wavelength, produce exactly two of the measured quantities R_a, R_s, and T. The main advantage of the Newton-Raphson technique is its rapid convergence. For a given d and λ , there can exist multiple solutions for n and k, and choosing the correct values for n, k and d involves an examination of the variation of n and k with for given d. When the best thickness d is employed, smooth, continuous curves for n and k as functions of are obtained. As a further check, the values of d determined above were used in a previously employed fitting procedure[10] which makes use of all three measured quantities R_a, R_s, and T simultaneously and good agreement has been obtained for n and k from these two procedures. The typical uncertainties in d were from $\pm$ 2% to $\pm$ 5%, while for n and k they were $\pm$ 0.04 and up to $\pm$ 0.02, respectively.

5. Optical energy gap

We have used the Tauc relation[18] $\epsilon_2(E)=B_1(E-E_{opt})^2/E^2$ to obtain the optical energy gap E_{opt}. If we plot $E(\epsilon_2)^{1/2}$ vs E, and extrapolate the region of absorption above the optical edge (the energy above which strong absorption sets in) back

to the E axis where E(E) equals zero (see Fig. 4.7), we should find E_{opt}, the optical energy gap.

E. Annealing

To study the change in property of the film with annealing the films are annealed at different annealing temperature(T_a). To remove the possibility of oxidation, the annealing is done in an oven in argon atmosphere. Argon is allowed to flow for one hour and then the samples are put in the oven and annealed for one hour at the desired temperature ranging from 350 to 1200°C, maintaining the flow of argon during and after the annealing till the sample cools down to room temperature.

CHAPTER V

OPTICAL CONSTANTS, MICROSTRUCTURE, AND CHEMICAL ORDERING

A.Results:

1. Film composition

The Si and C contents of the films prepared on Cu substrates have been determined directly by means of a scanning Auger Microprobe (SAM). Depth profiles of Si,C, and Cu were obtained throughout the films and into the substrate for eight of the nine alloy films studied. The results for the fractional carbon concentrations in these a-$Si_{1-x}C_x$:H alloys, $x=f(C)/[f(C)+f(Si)]$, are listed in Table 5.1, along with the estimated uncertainties. We note that for the two Si-rich samples for which SAM studies were undertaken, with $x=0.07$ and 0.38, evidence for a buildup of carbon at the film-substrate interface was observed from the depth profile. This carbon enrichment of the film-substrate interface could also be detected from the optical measurement (see below). In addition, excess carbon was typically observed on the film surfaces which had been exposed to air. Using the optically measured thickness for each film and a sputtering time for each film measured from the surface to where either the C or Si content has decreased to 50% of its average original value, sputtering rates for the various a-$Si_{1-x}C_x$:H films have been calculated. No definite trend in sputtering rate with increasing C concentration (decreasing Si concentration) is

observed. The average sputtering rate, excluding the 100% a-Si:H and a-C:H films, is calculated to be 9.2 Å/sec.

Also listed in Table 5.1 are carbon fractional concentrations, X(EMA), which were determined by means of the effective medium approximation, in which the film was considered to be composed of amorphous polymeric, graphitic, tetrahedral, and void components. Details of how these values for X(EMA) were obtained will be presented below.

2. Hydrogen content and film density

Estimates of the bonded hydrogen contents of some of these films have been obtained from the integrated absorbances of the carbon-hydrogen and silicon-hydrogen infrared stretching modes. For the a-C:H film prepared from 100% C_2H_2, $C-H_n$ stretching modes were observed between 2800 to 3000 cm^{-1}. Using a cross section for these modes of $(1.35 \pm 0.35)x10^{21}$ cm^{-2}, a hydrogen atomic concentration of $(7.4 \pm 1.9)x10^{22}$ cm^{-3} and hydrogen atomic percent of (54 ± 14) at % were obtained. The H atomic percentage is based on a measured density of 1.36 gm/cm^3 for this a-C:H film (see below). The ratio of C-H bonds to C atoms in the film, [C-H/C], was found to be $7.4x10^{22}cm^{-3}/6.2x10^{22}cm^{-3}=1.2$. In addition to the $C-H_n$ stretching modes, $C-H_n$ bending modes were observed at 1390 and 1460 cm^{-1}.

For a film prepared from 56% C_2H_2 and 44% SiH_4, in addition to C-H stretching modes in the range 2800-3000 cm^{-1} bending and scissoring modes are observed between 1200

and 1500 cm^{-1}. The silicon-hydrogen stretching mode at 2095 cm^{-1} was observed along with the $SiC-H_n$ wagging mode near 990 cm^{-1} and Si-C stretching mode at 775 cm^{-1}. The Si-C stretching mode was the dominant absorption feature in the spectrum. Integrated absorbances of the C-H and Si-H stretching modes [using the cross sections of C-H and Si-H to be $(1.35 \pm 0.35)x10^{21}cm^{-2}$ and $1.4x10^{20}$ cm^{-2}] yielded 3.4 and $1.0x10^{22}$ hydrogen atoms/cm^3, respectively in these bonds, for a total hydrogen atomic percentage of 46 at %. To determine the latter we have assumed equal densities of carbon and silicon atoms in the film and a film density of 1.78 gm/cm^3. The [C-H/C] and [Si-H/Si] ratios for this films were found to be 1.3 and 0.4 respectively.

For the film prepared from 100% SiH_4, Si-H stretch modes at 2000 and 2090 cm^{-1}, weak bending modes at 840 and 900 cm^{-1}, and the wagging mode at 640 cm^{-1} were observed. From the stretching modes, a hydrogen concentration of $3.5x10^{21}$ cm^{-3} was obtained, yielding 7.6 at % hydrogen for a measured film density of 2.07 gm/cm^3. The [Si-H/Si] ratio for this film was found to be 0.08.

The detailed and careful investigation of the IR modes of a-$Si_{1-x}C_x$:H as a function of annealing temperature and composition will be described in the following chapter.

The measured densities of these films are listed in Table 5.1. Film density increases smoothly from the value 1.36 gm/cm^3 for a-C:H to 2.07 gm/cm^3 for a-Si:H, with the

most rapid increase in density occurring as the Si fractional content increases in the range 0.2 to 0.6.

3. Optical constants

For the determination of values of n, k, and d (film thickness) from the optical measurements, we have employed the procedure as outlined by Nagendra and Thutupalli,[69] which has been described earlier. For several alloy concentrations on the Si-rich end of the alloy series (where n and k vary appreciably with photon energy), it was necessary to deposit films of differing thicknesses so that smooth values of n and k could be obtained over the entire photon energy range from 1.5 to 4.75 eV. Typical uncertainties in d were from ± 2% to ± 5%, while for n and k they were ± 0.04 and ±0.02, respectively.

The previously mentioned carbon enrichment of the film-substrate interface was also apparent from these optical measurements for the Si-rich films with C fractions of 0.07, 0.28 and 0.38. For these films, measured values of R_a yielded values for n and k which were not consistent with those determined from R_s for high photon energies (greater than 4 eV) . Values of R_s were instead consistent with lower n and k values for these films at the film-substrate interface, which would be the case if the region of the film next to the interface had a higher C content than the bulk of the film.

Results for n and k for the nine films studied are

presented in Figs. 5.1 and 5.2 as functions of photon energy E. Both n and k show a significant variation with concentration, with both increasing from a-C:H to a-Si:H . ϵ_1 and ϵ_2 as functions of photon energy are shown in Figs. 5.3 and 5.4 . Our results for k show an initial small decrease as Si is added to a-C:H, signaling a decrease in film absorption. This decrease is also apparent in Fig.5.5 where the absorption coefficient α is presented for all nine films as a function of energy.

4. Optical band gap

We have used the Tauc[18] plot of $E(\epsilon_2)^{1/2}$ versus E to obtain the optical energy gap E_{opt}, defined by $\epsilon_2(E)=B_1(E-E_{opt})^2/E^2$, for these films. Values for E_{opt} and B_1, (dimensionless) are listed in Table 5.1. E_{opt} increases from 2.24 eV for a-C:H (x=1) to a value of 2.68 eV for x=0.68, before decreasing to a value of 1.8 eV for a-Si:H (x=0). The slope B_1, which is inversely proportional to the width of the tail state band, first shows a slight decrease (1.63 to 1.59) as Si is added to a-C:H before increasing to a value of 5.5 for a-Si:H.

Other workers[1,2,5,70] who measure only film absorption typically employ the Tauc plot in the form $(\alpha E)^{1/2} = B(E-E_{opt})$. We have used our results for the absorption coefficient $\alpha=4\pi k/\lambda$, to test this expression and have found that it gives essentially the same values for E_{opt} as the more correct expression which makes use of $E(\epsilon_2)^{1/2}$ and which explicitly

takes into account the energy dependence of the index of refraction n. The constant B_T in the expression involving α is related to the corresponding constant B_1 by $B_T=(B_1/nhc)$ where n is the average index of refraction in the energy region where the Tauc plot is applicable (typically 3 to 5 eV for carbon-rich samples and 2.5 to 3.5 eV for silicon-rich samples). For comparison with the results of other workers, our results for B_T obtained from $(\alpha E)^{1/2}$ plot are also included in Table 5.1. Values for B_T calculated directly from B_1 and n using the above expression are systematically lower by 20% to 100% than those listed in Table 5.1 . Also included in Table 5.1 are values for E_{04}, the energy at which the absorption coefficient α is equal to 10^4 cm^{-1}.

5. Effective Medium Approximation

To obtain information concerning the types of bonding of carbon, silicon, and hydrogen atoms in these films from the measured optical constants,we have used the Bruggemann effective medium approximation (EMA) for composite heterogeneous media,[49] which is represented mathematically as (see Eq. 3.19)

$$\sum_i v_i \frac{\epsilon_i - \epsilon}{\epsilon_i + 2\epsilon} = 0 \qquad \sum_i v_i = 1 \tag{3.19}$$

where ϵ is the complex dielectric function of the composite medium and v_i and ϵ_i are the volume fraction and complex dielectric function of component i, respectively. The rational for applying the Bruggemann effective medium

approximation to a-$Si_{1-x}C_x$:H alloy series is described in the Theory section.

For the a-$Si_{1-x}C_x$:H alloy films, we propose that the following components will determine the dielectric response: amorphous polymeric (a-CH_m $m \sim 2$ with volume fraction v_{ap}), amorphous graphitic (a-C, v_{ag}), amorphous tetrahedral (a-Si:C:H, v_{at}) and void (v_v). We wish to emphasize that these a-$Si_{1-x}C_x$:H films, although assumed to be heterogeneous on a microscopic level, are nevertheless macroscopically homogeneous.

In order to apply the EMA expressed by Eq.(3.19) to our measured ϵ_1 and ϵ_2 spectra so that the volume fractions v_i of the proposed components can be obtained, we first need the ϵ_i spectra for the individual components. For the amorphous polymeric components we use ϵ_1 and ϵ_2 based on smoothed data[54] for polyethylene with a density of 0.92 gm/cm^3. For the amorphous graphitic component we have chosen to use the measured ϵ_1 and ϵ_2 spectra[15] for an a-C:H film annealed at 500°C, with a measured density of 1.47 gm/cm^3.

As there exist no measured spectra for completely tetrahedrally-coordinated a-$Si_{1-x}C_x$:H, a Si- and C-centered tetrahedron model[55] has been developed to calculate ϵ_1 and ϵ_2 spectra for the a-$Si_{1-x}C_x$:H tetrahedral component as a function of its composition. This is described in the Appendix(I).

These ϵ_1 and ϵ_2 spectra for the amorphous tetrahedral components have been obtained by scaling from our ϵ_1 and ϵ_2 data for a-Si:H and as a result, the dielectric response of the amorphous tetrahedral component can be considered to reflect the contribution of approximately 10 at % hydrogen.

An additional aspect of the problem of obtaining appropriate ϵ_1 and ϵ_2 spectra for the amorphous tetrahedral components involves the issue of whether or not chemical ordering occurs in the bonding between C and Si atoms. The cases of no chemical ordering, homogeneous chemical ordering, and phase-separated chemical ordering lead to significantly different ϵ_1 and ϵ_2 spectra for the amorphous tetrahedral component. Our measured ϵ_1 and ϵ_2 spectra along with the EMA not only determine v_i of various components but also provide information on whether or not the Si and C atoms in the amorphous tetrahedral component have a tendency to be chemically ordered.

Our experimental results for ϵ_1 and ϵ_2, along with the ϵ_i spectra for the proposed components specified as described above, have been used in Eq. (3.19) for the EMA in order to determine the volume fractions v_i (i.e., v_{ag}, v_{ap}, v_{at}, v_v) of the four components present in these a-$Si_{1-x}C_x$:H films, as functions of film composition x. A least mean-square fitting procedure, which involved minimizing not only the real and imaginary parts of Eq. (3.19), but also the difference between the measured film density (Table 5.1) and

the calculated film density (equal to $\sum_i \rho_i v_i$), where the ρ_i are the densities of the individual components, has been employed to obtain the best values for v_i. Thus the measured film densities have been crucial in setting constraints on the possible v_i of the various components. In this fitting procedure, the film stoichiometry x as well as the volume fractions v_i of the components have been allowed to vary in order to obtain a best fit.

In addition to determining the film stoichiometry x and the volume fractions v_i, the fitting procedure has also enabled us to test for the existence or absence of chemical ordering in the amorphous tetrahedral component for these a-$Si_{1-x}C_x$:H films. We illustrate the effect of chemical ordering on ϵ_1 and ϵ_2 for the film which, according to the Auger measurement, contained a carbon fraction of 0.38. Assuming complete chemical ordering with homogeneous dispersion in the amorphous tetrahedral component, the best fit to the measured ϵ_1 and ϵ_2 was obtained for a carbon fraction of 0.38 ± 0.01, in excellent agreement with the Auger result. This fit to the experimental ϵ_1 and ϵ_2 is shown in Fig 5.6 and 5.7, along with the best fits to the data under the assumptions of complete chemical ordering with phase separation and of no chemical ordering. It is clear from Figs. 5.6 and 5.7 that complete chemical ordering with homogeneous dispersion gives the best fit to the data for this sample.

The results obtained from the EMA for the volume fractions of the various components present in these a-$Si_{1-x}C_x$:H films are listed in Table 5.2 and plotted in Fig 5.8 as functions of film composition. For all the alloy samples studied, the best possible fits to the data using the EMA favored complete chemical ordering with homogeneous dispersion over no chemical ordering. Also listed in Table 5.2 are the EMA results for x(EMA), the carbon fraction in the film which gave the best fit in the EMA, and x_{at}, the corresponding carbon fraction in the amorphous tetrahedral component. We note that x_{at} is less than x(EMA) for films in which a fraction of the carbon atoms are in the amorphous polymeric and graphitic components.

Beginning with a-C:H (x=1.0), the major component in the film is found to be the amorphous polymeric one (67%), with significant amounts of amorphous graphitic (17%) and amorphous tetrahedral or diamond-like (16%) components also found to be present. This results are quite consistent with previous results[15] obtained for an a-C:H film prepared via a dc glow discharge technique, where corresponding percentages of 75%, 11% and 14% for these three components were obtained. As Si is added to the a-C:H film, it can be seen from Table 5.2 and Fig. 5.8 that the amorphous polymeric and amorphous graphitic components gradually decrease essentially to zero at a Si fractional content of 0.62 (x=0.38). At the same time, the amorphous tetrahedral

component increases, reaching 100% for x=0 (a-Si:H). These variations of v_{ap}, v_{ag}, and v_{at} are observed to be essentially linear in the Si content of the films (see Fig 5.8). A void component appears as Si is added, reaching a maximum value of 26% for x=0.38 before falling to zero for x=0 (a-Si:H)

The carbon concentrations in the films determined via EMA, x(EMA) are in very good agreement with the values obtained from the Auger measurements, with two films requiring additional comment. An Auger analysis of the composition of the x(EMA)= 0.28 film was not undertaken, so that no comparision is possible for this sample. In addition, the sample for which a carbon fraction of x=0.07 was determined via Auger was prepared under somewhat different discharge conditions (higher dc bias voltage on powered electrode) than the sample for which optical measurements were made and for which x(EMA)=0.16 was determined . The carbon content of the amorphous tetrahedral component, x_{at}, shows the expected decrease from x_{at}=1.0 for a-C:H to x_{at}=0.0 for a-Si:H, see Table 5.2 .

In addition to obtaining the volume fractions v_i for the various components in the films from the EMA, we can also obtain information about the fractional atomic concentrations of carbon, hydrogen, and silicon in the films by combining the EMA results for the v_i with the bonded hydrogen concentrations obtained from the IR measurements.

For $x=0$ (a-Si:H) we found about 8 at % H in the film and have used this for the hydrogen content of the amorphous tetrahedral component for all compositions $0 \leqslant x \leqslant 1$. For $x=1$ (a-C:H) we found 54 at% H, which, when attributed to the amorphous polymeric component (a-CH_m) with volume fraction of 0.67, is equivalent to a stoichiometry of approximately $CH_{2.5}$ for this component. For consistency with our use of the smoothed polyethylene spectrum for the amorphous polymeric component, we have chosen instead to use CH_2 as its stoichiometry.

In Fig. 5.9 we show the resulting Si, C and H fractions in the films as functions of the Si content(excluding hydrogen). For $x=1$, a-C:H, the film is found to have a composition corresponding to 54 at % C and 46 at % H, which is in reasonable agreement with our IR determination of (54±14) at % H. It is clear from Fig 5.9 and our IR results that the C- rich films contain three to four times as much hydrogen as the Si-rich films. In Fig 5.10 and 5.11 we show both the measured ϵ_1 and ϵ_2 and also the results of the EMA for ϵ_1 and ϵ_2, assuming complete chemical ordering with homogeneous dispersion, for the $x=0.68$ and $x=0.16$ samples, respectively.

B. Discussion

Film composition is a critical parameter for understanding and developing a model for the optical constants of these hydrogenated amorphous silicon and carbon

alloy films. The carbon concentrations determined via Auger, x, and via the EMA, x(EMA), have been found to be in very good agreement with each other, to within ± 0.03 (see Table 5.1) thus strengthening the conclusions which we have reached basing on the results of our EMA model.

In addition to quantitative agreement on composition, the Auger and optical results have also both been found to be sensitive to film inhomogeneity in that both gave evidence for an enhancement of the C concentration at the film-substrate interface in the Si- rich films. This initial C buildup may be due to an enhanced initial breakdown of C_2H_2 in the discharge relative to SiH_4.

Hydrogen also plays a crucial role in the properties of these films, and we have used our IR results along with the results of the EMA model to determine the atomic fractions of the three elements present in these films, Si,C and H. These results, presented in Fig. 5.9 as funtions of Si content (1-x), indicate that the hydrogen atomic fraction decreases from about 0.5 for x=1 (a-C:H) to about 0.1 for x=0 (a-S:H). The IR modes observed are consistent with a considerable amount of the hydrogen in the a-C:H film bonded in CH_3 and CH_2 groups. These IR results for the amount of H bonded and the presence of CH_3 and CH_2 groups in a-C:H are consistent with the presence of a significant amorphous polymeric component,[15,71] with composition given approximately by a-CH_2. In the a-Si:H film, most of the

hydrogen is bonded in SiH_2 groups.

The observed increase in film density from 1.36 gm/cm^3 for a-C:H to 2.07 gm/cm^3 for a-Si:H is consistent with a decrease in the volume fraction of the low-density amorphous polymeric component and the incorporation of increasing amounts of Si into the higher density amorphous tetrahedral component as a-Si:H is approached. Our measured low value for the density of a-Si:H, 2.07 relative to 2.33 gm/cm^3 for crystalline Si, results from the porous nature of the film, as evidenced by the predominance of dihydride, SiH_2, groups in the film as observed via IR. The use of Ar to dilute the SiH_4 in the glow-discharge deposition of a-Si:H, as we have employed, is known to result in the production of porous films.[72]

The optical constants n and k, ϵ_1 and ϵ_2 show a systematic variation with film composition from a-C:H (x=1) to a-Si:H (x=0). The index of refraction n is low for a-C:H, 1.7, and increases as the Si concentration increases, see Fig. 5.1. This increase in n, which is consistent with the observations of previous workers,[5,13,73] can be attributed to the decrease in the average energy gap parameter E_g, which is related to n via the expression[74]

$$n^2 = 1 + A\left(\frac{\hbar\omega_p}{E_g}\right)^2 \tag{5.1}$$

where w_p is the plasma frequency (proportional to the square root of the valence electron concentration in the film), and A is a constant. According to the Si- and C- centered

tetrahedron model,[55] E_g decreases from 13.62 to 4.76 eV as x decreases from 1 to 0 in the a-$Si_{1-x}C_x$:H alloy series (i.e. from a-C:H to a-Si:H). This decrease in E_g is also responsible for the increasing dispersion observed in n as the Si content increases from a-C:H to a-Si:H, see Fig. 5.1

The imaginary part of the index k initially shows a small decrease, about 15 % at 4.75 eV, as Si is added to a-C:H (see Fig. 5.2). This decrease in absorption results from the replacement of strongly absorbing graphitic C-C bonds by Si-C bonds which absorb at higher energies. At higher Si concentrations, k increases again as Si-C bonds are replaced by Si-Si bonds which absorb at lower energies. The dependence of $\epsilon_1 = n^2 - k^2$ and $\epsilon_2 = 2nk$ on x (see Figs. 5.3 and 5.4) essentially reflect the previously discussed dependences of n and k on x.

Comparisions between the ϵ_1 and ϵ_2 spectra predicted by the microstructural model and the measured spectra are presented in Figs. 5.6, 5.7, 5.10, and 5.11. In Figs. 5.6 and 5.7 the measured ϵ_1 and ϵ_2 spectra for the film with a carbon fraction of 0.38 are compared with three separate predictions of the microstructural model, each corresponding to a different form of chemical ordering between the carbon and silicon atoms in the amorphous tetrahedral component: (1) Complete chemical ordering with homogeneous dispersion (2) complete chemical ordering with phase separation and (3) no chemical ordering. The latter two

predictions both yield spectra with peaks in ϵ_1 and ϵ_2 at energies which are too low by at least 0.5 eV when compared to the measured ϵ_1 and ϵ_2. This stronger absorption at lower energies for predictions (2) and (3) can be attributed to the presence of highly absorbing $Si\text{-}Si_4$ tetrahedra in the amorphous tetrahedral component. In particular, for this film with a carbon fraction of x_{at}=0.365 in the amorphous tetrahedral component (see Table 5.2), the fraction of all tetrahedra which are $Si\text{-}Si_4$ tetrahedra is only 0.021 for complete chemical ordering with homogeneous dispersion, 0.103 for no chemical ordering and 0.270 for complete chemical ordering with phase separation.[55] It is clear that the measured spectra are quite consistent with the low fraction of $Si\text{-}Si_4$ tetrahedra as given by complete chemical ordering with homogeneous dispersion.

Figures 5.10 and 5.11 show comparisions between the measured ϵ_1 and ϵ_2 for films with carbon fractions of 0.68 and 0.16, respectively, and the microstructural model predictions for the case of complete chemical ordering with homogeneous dispersion in the amorphous tetrahedral component. For the carbon rich sample with x=0.68, the agreement between experiment and microstructural model prediction is good for ϵ_1 but not as satisfactory for ϵ_2. The higher ϵ_2 at low energies of the predicted spectrum as compared to that of the measured spectrum is due to the amorphous graphitic component in the microstructural model

with volume fraction v_{ag}=0.11 for this film (see Table 5.2). Clearly the spectrum we use in the microstructural model for amorphous graphitic component is too highly absorbing at low energies. This was also observed in case of a-C:H[15] and remains an area for improvement in the model. In Fig. 5.11 the measured spectra for ϵ_1 and ϵ_2 are both seen to be in very good agreement with the predictions of the microstructural model. The spectra of films with such a low carbon content of only 0.16 are not, however, very sensitive to the degree or type of chemical ordering present in the film.

The addition of Si to a-C:H leads to an initial increase in E_{opt} and from Tables 5.1 and 5.2 and Fig. 5.12 where E_{opt} is plotted as a function of the volume fraction of the amorphous graphitic component v_{ag}, it can be seen that the increase in E_{opt} is associated with a decrease in v_{ag}. Also included in Fig. 5.12 are previous results for an annealed a-C:H film[15], where it was found that E_{opt} goes to zero when v_{ag} reaches a value of 0.75. The increase in E_{opt} as Si is added to a-C:H reaches a maximum value of 2.68 eV for a Si fraction of 0.32, in good agreement with the results of other workers.[1,5,70] E_{opt} then decreases as the Si concentration increases further. This decrease in E_{opt} for Si fractions greater than 0.32 starts at the point where the amorphous tetrahedral component becomes Si-rich (ie, x_{at} <0.5; see Table 5.2), and hence, even for the case of

complete chemical ordering, Si-Si bonds must be present in the film. Since Si-Si bonds absorb at lower energies than either Si-C or tetrahedral C-C bonds, their presence in the films shifts the absorption edge to lower energies, leading to lower values of E_{opt} for a Si fraction greater than 0.32.

It is important to note that the observed increase in E_{opt} from 2.24 to 2.68 eV as the Si fraction increases from 0 to 0.32 is associated with only very small changes in absorption, i.e. small decreases in k and ϵ_2, see Figs. 5.2 and 5.4 . In addition, the film with highest E_{opt} of 2.68 eV actually has higher absorption for all energies in the measured range, 1.5-4.75 eV, than does the film with Si fraction of 0.16 which has E_{opt}=2.38 eV. The higher E_{opt} for a Si fraction of 0.32 clearly results from a sharper absorption edge rather than from lower overall optical absorption. We conclude that the increase in E_{opt} with Si concentration results not from shifts of the band edges (E_c or E_v), but from changes in the regions of the localized tail states where the energy levels of the localized π electrons associated with the amorphous graphitic component are located. These localized tail state bands will become narrower as Si is added and v_{ag} decreases. This picture is consistent with the observed increase in the slope parameters B_1 and B_T (see Table 5.1) with increasing Si concentration.

E_{opt} also increases as C is added to a-Si:H, which

can be understood as due to the replacement of weaker Si-Si bonds by stronger Si-C bonds in the amorphous tetrahedral component.[16] Ultimately, as the C content increases further, graphitic C-C bonds appear in the film and E_{opt} begins to decrease. The slope parameters B_1 [from $E(\epsilon_2)^{1/2}$ versus E] and B_T [from $(\alpha E)^{1/2}$ versus E] both decrease (see Table 5.1) as C is added to a-Si:H, signaling increasing widths for the bands of localized tail states. This increase in width arises from increased compositional disorder in the films. Si-C bonds are much shorter (1.88 A) than Si-Si bonds (2.35 A) and so bond angle distortions will be enhanced in $a\text{-}Si_{1-x}C_x$:H as compositional disorder is added to the topological disorder already present in a-Si:H.[75] It is also to be noted that the low values of B_1 and B_T for a-Si:H result from the predominantly dihydride (SiH_2) bonding for hydrogen in the film.

Additional confirmation for the existence of complete chemical ordering with homogeneous dispersion in the films comes from the observed experimental variation of E_{opt} with carbon fraction x, shown in Fig. 5.13 along with prediction of the EMA[55] assuming the amorphous tetrahedral component to be the only component present in the films. The observed value of E_{opt} up to x=0.4 are in much better agreement with the predicted values assuming complete chemical ordering with homogeneous dispersion than with the predicted values assuming either phase separation or no

chemical ordering. Deviations between the model and experiment begin for x> Ø.4, the carbon concentration above which the amorphous graphitic component begins to appear in the film (see Table 5.2 and Fig. 5.8). Again, it is the appearance of this amorphous graphitic component which limits E_{opt} as the carbon fraction x increases in the films.

Our use of the EMA to describe the optical spectra of these a-$Si_{1-x}C_x$:H films has provided useful information on the variations of the volume fractions of the four proposed components (amorphous polymeric, amorphous graphitic, amorphous tetrahedral, and void) as functions of film composition. Although clearly an oversimplification for the structure of these films, our model is a successful first approximation to the local bonding and has provided, for the first time, a useful framework for understanding the properties of this technologically important alloy series.

There exists additional experimental evidence supporting our use of amorphous polymeric, graphitic, and tetrahedral components in our microstructural model. IR studies[76-78] including our own results, have indicated that the majority of the hydrogen in the films is bonded to C, as opposed to Si, thus supporting the use of an amorphous polymeric component with approximate composition CH_2 and an amorphous tetrahedral component with a much lower H content, 1Ø at %. We note here that an additional improvement to our

model would be to allow the hydrogen content of the amorphous tetrahedral components to increase as the C content of this component increases. NMR studies[79] also point to the existence of two hydrogen containing phases in a-$Si_{1-x}C_x$:H alloys: heavily hydrogenated C clusters (the amorphous polymeric component) and a weakly hydrogenated a-Si lattice (the amorphous tetrahedral component).

The microstructural model indicates that a void component appears in these a-$Si_{1-x}C_x$:H films from the Si-rich end as C is added to a-Si:H and also from the C-rich end as Si is added to a-C:H. The increased compositional disorder[75] in the films as a result of alloying leads to the generation of voids due to the inability of the various components to fit together perfectly. The maximum void volume fraction of 0.26 occurs for a C fraction of 0.38, the composition at which the volume fraction of the amorphous polymeric component drops to a very low value (0.03). The amorphous polymeric component is thus proposed to be effective in helping to relax the amorphous network so that the components fit together better, with less of a tendency for the presence of voids.

Relaxation of the amorphous network by the hydrogen-containing amorphous polymeric component can also be understood in terms of the average coordination number Z for a particular alloy, e.g., a-$Si_wC_yH_z$. Here $w+y+z=1$ and the carbon fraction can be written as the sum of tetrahedral

(y_t) and graphitic (y_g) parts, i.e., $y=y_t+y_g$. With this notation we have $Z=4-y_g-3z$. Using our results for the volume fractions (Table 5.2) and atomic fractions (Fig. 5.9), we calculate $z=2.4+0.2$ for a-C:H and $z=3.75+0.1$ for a-Si:H, with z increasing smoothly between these two limits as the Si content increases. This result for a-C:H is very close to the value z=2.45 given by Phillips[80] as the average coordination number for an alloy in which all bond-length and bond-angle constraints are satisfied, thereby reducing the strain in the alloy.

From our use of microstructural model for the ϵ_1 and ϵ_2 spectra, we have clear evidence for a strong tendency for homogeneous chemical ordering of the C and Si atoms for our Si-rich samples where the amorphous tetrahedral component is dominant. The situation on the C-rich side of the alloy series is complicated by the presence of the amorphous polymeric and graphitic components. Still, we do see a tendency toward at least partial chemical ordering both from our ϵ_1 and ϵ_2 results. The driving force for chemical ordering, i.e. , the presence of the maximum possible number of Si-C bonds in a film, is likely to be lowering of the free energy. The Si-C bond is more stable than the average of Si-Si and C-C bonds[81]. In a particular a-$Si_{1-x}C_x$:H sample, however, the degree of chemical ordering present will be critically dependent on the deposition conditions.

CHAPTER VI

INFRARED ABSORPTION, STRUCTURAL CHANGE, AND LOCAL ATOMIC BONDING

A.Results

To understand the change in local bonding and the structural changes leading to crystallization, hydrogenated amorphous silicon-carbon alloy films $a\text{-}Si_{1-x}C_x:H$ are studied as a function of annealing temperature (T_a) and as a function of composition (x) by means of FTIR and UV-VIS spectroscopy.

I. Effect of Annealing Temperature.

1. Infrared Spectra

The IR spectra of the films exhibit rich structure in four main absorption regions[12].

a. Absorption band from 2000-2300 cm^{-1} is due to Si-H stretch.

b. The band from 2800-3000 cm^{-1} is ascribed to C-H stretch.

c. Absorption bands from 1200 to 1500 cm^{-1} are due to bending and scissoring modes of CH_2, CH_3, $Si(CH_3)$ and $C(CH_3)$.

d. Absorption bands from 600-1200 cm^{-1} are ascribed to Si-C stretch, Si-O stretch, SiH_2 and $(SiH_2)_n$ bending and Si-H group rocking.

Each absorption region will now be discussed in turn:

a. Absorption band from 2000 to 2300 cm^{-1}

The absorption band from 2000-2300 cm^{-1} is due to Si-H

stretch. Fig 6.1 shows the result for absorbance in the region of the Si-H stretch mode for different annealing temperature (T_a) for an a-$Si_{1-x}C_x$:H film, with x=0.17. The deconvoluted Si-H peak positions, widths (FWHM, Full Width at Half Maximum), and the total area under these peaks are presented in Table 6.1. The Si-H mode (see Fig. 6.2) is observed to have a large peak at 2085 cm^{-1} and a small peak at 2151 cm^{-1} for the as-deposited film, T_s=250°C. Initially (see Table 6.1) the peaks shift only slightly to lower wavenumber (2073 cm^{-1} and 2132 cm^{-1}) for T_a=350°C and then shift to higher wavenumber with subsequent anneal to higher temperature. When T_a is above 350°C another small peak appears near 2230 cm^{-1}. The normalized area (area/thickness of the film) under the peaks decreases from 7.36×10^{-4} cm^{-1}/Å for the as-deposited film at T_s=250°C to 9.35×10^{-5} cm^{-1}/Å for T_a=550°C. Above T_a=550°C the Si-H stretch mode can be barely observed.

The 2085 cm^{-1} peak[30,31] of the a-$Si_{1-x}C_x$:H film can be assigned either to SiH_2 stretching modes and or to a shift of monohydride (SiH) bond stretching frequency in a different environment[3] where the Si is bonded to carbon. The peaks observed (see Table 6.1) near 2150 cm^{-1} and 2230 cm^{-1} are attributed to the situation when one or more oxygen[82] atoms are attached to SiH or to SiH_2. Using the relation obtained by Lucovsky[83], the SiH and SiH_2 stretching frequencies in a-$Si_{1-x}C_x$:H films can be represented as

$$\nu_{Si-H}(cm^{-1}) = 1740.7 + 34.7\sum_{i=1}^{3} X(R_i) \qquad (6.1)$$

$$\nu_{Si-H_2}(cm^{-1}) = 1956.3 + 25.4\sum_{i=1}^{2} X(R_i)$$

where ν is the wavenumber of SiH stretch and $X(R_i)$ is the electronegativity of the attached atom. From the above equation one can estimate the frequency shift of SiH and SiH_2 due to neighboring atoms like silicon, carbon and oxygen (see Appendix II).

The width (FWHM) of the 2085cm^{-1} peak decreases from 80 to 72 cm^{-1} for T_a=350°C and then increases with subsequent anneal to higher temperature. No definite trends in the widths of the 2150 and 2230 cm^{-1} peaks with T_a are observed.

b. Absorption band from 2800 to 3000 cm^{-1}

The absorption between 2800-3000 cm^{-1} is due to the C-H stretching mode. Fig. 6.3 represents the results for the absorbance for C-H stretch for different T_a. The deconvoluted peak positions, widths and the areas are presented in Table 6.2. The deconvoluted spectrum of the as-deposited film (see Fig 6.4) is observed to peak at 2950 cm^{-1}, 2915 cm^{-1}, 2870 cm^{-1}, and 2800 cm^{-1}. The peaks at 2950 cm^{-1} and 2870 cm^{-1} are assigned to CH_3 asymmetric and symmetric stretch, respectively. The assignment of these modes are in agreement with Wieder et al,[3] Tawada et al[12] and McKenzie[33]. The peaks at 2915 cm^{-1} and 2800 cm^{-1} are assigned to CH_2 asymmetric and symmetric stretch, respectively. The assignment of the 2915 cm^{-1} peak is in good agreement with Tawada et al[12] with the exception of

the 2800 cm^{-1} peak which we assign to CH_2 symmetric stretch. The normalized area under these peaks decrease from $3.9x10^{-4}$ $cm^{-1}/Å$ for as deposited film at T_s=250°C to $5.4x10^{-5}$ $cm^{-1}/Å$ for T_a=550°C with increase in T_a (see Table 6.2). Above T_a=550°C the C-H stretch mode can be barely observed. This decrease in area is due to the loss of hydrogen. No definite trend in the widths of the peaks as functions of T_a are observed. Thus, it seems that CH_3 and CH_2 stretching modes are responsible for the absorption in the region from 2800-3000 cm^{-1}.

c. Absorption bands between 1200-1500 cm^{-1}

The absorption bands between 1200-1500 cm^{-1} are ascribed to the bending and scissoring modes of CH_2, CH_3, $Si(CH_3)$ and $C(CH_3)$. The small peaks appear at 1250 cm^{-1}, 1346 cm^{-1}, 1373 cm^{-1}, 1404 cm^{-1}, and 1454 cm^{-1} (see Fig.2.3) These peaks are assigned to $Si(CH_3)$ symmetric bond bending, CH_3 symmetric bending, $-C(CH_3)_2$ symmetric scissors, $Si-CH_2$ scissoring and CH_2 scissoring, respectively. The assignments of these modes are in agreement with McKenzie[33] with the exception of the 1373 cm^{-1} mode which is assigned to -$C(CH_3)_2$ symmetric scissors which is in agreement with Alpert et al.[84] The areas under these peaks decrease due to the removal of hydrogen with increase in T_a. When T_a reaches 450°C, the 1373 cm^{-1} peak which is due to CH_3 symmetric scissors disappears. When the annealing temperature is increased further to 550°C, the 1450 cm^{-1} and 1400 cm^{-1}

peaks disappear and the modes left behind are CH_3 symmetrical bending (1350 cm^{-1}) and Si-CH_3 symmetrical bending (1250 cm^{-1}). This Si-CH_3 symmetrical bending mode shifts to higher wavenumber from 1250 cm^{-1} to 1273 cm^{-1} as the annealing temperature is increased from 450°C to 550°C. All of these bending modes disappear when the annealing temperature is increased above 650°C. Thus we see that the modes in this region are due to bending and scissoring modes of CH_3 and CH_2.

d. Absorption bands between 600-1200 cm^{-1}.

The absorption bands between 600-1200 cm^{-1} are ascribed to Si-H group rocking or wagging, SiH_2 and $(SiH_2)_n$ bending, and Si-C and Si-O stretch modes. Figs. 6.5a and 6.5b represent the results for absorbance for these modes for different T_a. The deconvoluted spectrum (see Fig. 6.6a) in this range is observed to peak at 655 cm^{-1}, 766 cm^{-1} and 989 cm^{-1} for the as-deposited film at T_s=250°C. The peak positions and the widths of Si-C and Si-O modes as a function of T_a are shown in Figs. 6.6b and 6.6c respectively.

The absorption band at 655 cm^{-1} is assigned to SiH group rocking or wagging. The peak position, width, and the area under the peak as functions of T_a are presented in Table 6.3. The normalized area under this mode decreases from 1.14 x 10^{-3} cm^{-1}/Å for the as-deposited film at T_s=250°C to 3.21x10^{-4} cm^{-1}/Å at T_a=650°C. Above 650°C, i.e. at 800°C, this mode disappears. This clearly agrees with

the observation that no other-hydrogen related modes are present above 650°C.

The absorption band at 766 cm^{-1} is assigned to Si-C stretch. The position, width, and the area of this mode along with the density of Si-C bonds as functions of T_a are presented in Table 6.4. The remarkable features associated with this mode are: (see Table 6.4 and Fig 6.6b)

1) The normalized area under this peak (Si-C) increases from 1.22×10^{-3} cm^{-1}/Å for the as-deposited film at T_s=250°C to 11.5×10^{-3} cm^{-1}/Å for T_a=1200°C.

2) The peak shifts to higher wavenumber with increase in T_a. The peak is at 766 cm^{-1} at T_s=250°C and shifts to 808 cm^{-1} for T_a=1000°C and then decreases to 798 cm^{-1} for T_a=1200°C.

3) The peak width increases from 124 cm^{-1} for T_s=250°C to 160 cm^{-1} for T_a=650°C, decreases to 126 cm^{-1} for T_a=800°C, and keeps decreasing with increase in T_a.

4) The line shape of this mode appears to be Gaussian up to T_a=650°C and above this temperature it changes to Lorentzian. The mathematical expressions for the Gaussian and Lorentzian line shape are given as

$$y = h \exp\left[-(x-x_0)^2/\sigma^2\right]$$
$$y = \frac{h\sigma^2}{(x-x_0)^2 + \sigma^2} \qquad (62)$$

where σ = HWHM/$\sqrt{\ln 2}$ for the Gaussian and σ = HWHM for the Lorentzian line shape. The peak width corresponds to the Full Width at Half Maximum (FWHM) which is twice the Half Width at Half Maximum (HWHM), x_0 is the position at which the

curve is peaked, and h is the height at x_o

Estimates of the density of Si-C bonds in the film as a function of annealing temperature (see Table 6.4), have been obtained from the integrated absorbance of the Si-C infrared stretching mode. The cross-section of the Si-C stretch is determined to be 2.13×10^{19} cm^{-2} as described earlier (see Chapter III)

The absorption band at 989 cm^{-1} is assigned to Si-O stretch. The position, width, and the area of this mode along with the density of Si-O bonds as functions of T_a are presented in Table 6.5. The notable features associated with this mode are:(see Table 6.5 and Fig. 6.6c)

1) The normalized area under this peak (Si-O) increases from 7.08×10^{-4} $cm^{-1}/Å$ for the as-deposited film at $T_s=250^oC$ to 5.22×10^{-3} $cm^{-1}/Å$ for $T_a=1000^oC$. Above $T_a=1000^oC$ this mode disappears.

2) The peak shifts to higher wavenumber with increases in T_a. The peak is at 989 cm^{-1} for $T_s=250^oC$ and shifts to 1070 cm^{-1} for $T_a=1000^oC$.

3) The peak width increases from 158 cm^{-1} for $T_s=250^oC$ to 192 cm^{-1} for $T_a=650^oC$, decreases to 148 cm^{-1} for $T_a=800^oC$, and keeps decreasing with increase in T_a.

4) The line shape of this mode appears to be Gaussian up to $T_a=650^oC$ and above this temperature it changes to Lorentzian.

Estimates of the density of Si-O bonds in the film

as a function of annealing temperature (see Table 6.5), have been obtained from the integrated absorbance of the Si-O infrared stretching mode. The cross-section of the Si-O stretch is determined to be 1.5×10^{19} cm^{-2} which is described in chapter III

The change in the line shape of Si-C and Si-O along with the variation of the width seems to indicate the change from amorphous to microcrystalline and then to crystalline phase with increasing in T_a.

Other features that are present in this region are the 860-890 cm^{-1} bands, assigned to the SiH_2 and $(SiH_2)_n$ bending modes by Brodsky[30] and Fritzsche[31]. These modes disappear with increasing T_a. These peaks are very weak and we have not analyzed them. The normalized area of IR modes as a function of T_a are shown in Fig. 6.I . Typical uncertainty in their area is about ±10% .

2. Optical Constants

For determining the values of n,k and d (film thickness) from the optical measurements, we have employed the procedure as outlined by Nagendra and Thutupalli,[69] which has been described earlier (see chapter IV). Smooth values of n and k are obtained over the entire photon energy from 1.5 eV to 4.75 eV. The film thickness d (see Table 6.5a) remains essentially constant upto T_a=550°C. The thickness decreases by about 21% (from the average value of 3275 Å for T_a < 550°C to 2580 Å for T_a=1200°C for the

$a\text{-}Si_{1-x}C_x$:H (x=0.17) film used for IR measurements) and decreases by about 29% (from the average value of 1221 Å for $T_a \leqslant 550^{\circ}C$ to 866 Å for T_a=1200°C for the $a\text{-}Si_{1-x}C_x$:H (x=0.17) film used for optical constants measurements) upon further anneal upto 1200°C. This decrease in film thickness is due in part to film densification but may also signal a partial volatization of the film at higher T_a. Typical uncertainties in d are from ±2% to ±5% while for n and k they are +0.04 and +0.02, respectively. Results for n, k, ϵ_1, ϵ_2 and α are presented in Figs. 6.7, 6.8, 6.9, 6.10, and 6.11, as functions of photon energy E. The optical constants show slight variations with annealing temperature.

3. Hydrogen content and the optical band gap

Estimates of the bonded hydrogen content of this film, as a function of annealing temperature, have been obtained from the integrated absorbances of the carbon-hydrogen and silicon-hydrogen infrared stretching modes. The cross sections of the C-H and Si-H modes used are $(1.35 \pm 0.35)\times10^{21}$ cm^{-2} and 1.4×10^{20}cm^{-2}, respectively as described earlier (see chapter III). The amount of hydrogen bonded to C is approximately four times larger than that bonded to Si. The hydrogen content and the optical band gap as functions of annealing temperature are presented in Table 6.6.

We have used the Tauc[18] relation $\epsilon_2(E)=B(E-E_{opt})^2/E^2$ to obtain the optical energy gap E_{opt} for the annealed films which has been described earlier (see chapter IV). Typical

uncertainties in E_{opt} ranges from ±2% to ±4% . Fig. 6.12 shows the results for the E_{opt} for different annealing temperature. The value of E_{opt} decreases from 2.35 eV for the as-deposited film at T_s=250°C to 2.1 eV for T_a=550°C and the hydrogen content decreases from $5.27 \times 10^{22} cm^{-3}$ for T_s=250°C to $7.34 \times 10^{21} cm^{-3}$ for T_a=550°C (see Table 6.6). Thus we see a correlation of E_{opt} with hydrogen content (see Fig.6.13). A similar correlation of E_{opt} with hydrogen content is also observed by Beyer et al[85]. When T_a=650°C the band gap decreases to 2.0 eV and with further increase in T_a the band gap increases and reaches 2.2 eV for T_a=1200°C. We also observe an interesting correlation between the optical band gap and the inverse of the widths of Si-C (see Fig. 6.14) and Si-O (see Fig. 6.15) stretch bands. The optical band gap E_{opt} and the inverse of the widths of Si-C and Si-O are given in Table 6.7 .

II. Effect of Composition

1. Infrared Spectra

The spectra of the films as a function of composition exhibit rich structure in four absorption regions, as observed for annealing.
Each absorption region will now be discussed in turn :
a. Absorption band from 2000-2300 cm^{-1}

The absorption band from 2000-2300cm^{-1} is due to Si-H stretch. Fig. 6.16 shows the results for absorbance of Si-H stretch for different compositions (x). The deconvoluted

Si-H peak positions, widths, and the areas are shown in Table 6.8 . The Si-H peak is observed to be near 2000 cm^{-1} for a-Si:H (x=0) film made under same conditions. Addition of 5% of carbon (x=0.05) shifts the peak to 2082 cm^{-1}. Along with this 2082cm^{-1} peak two small peaks are observed at 2006cm^{-1} and 2132cm^{-1} (see Table 6.8) and further addition of carbon eliminates the 2006cm^{-1} peak and shifts the 2082 cm^{-1} and 2132 cm^{-1} peaks to higher wavenumber. These modes are observed to peak at 2099 cm^{-1} and at 2184 cm^{-1} for x=0.38. The normalized area increases from $5.5x10^{-4}cm^{-1}/\AA$ for a-Si:H (x=0) to $7.1x10^{-4}$ $cm^{-1}/\AA$ for x=0.05 and decreases ultimately to $5.2x10^{-4}$ $cm^{-1}/\AA$ for x=0.38 (see Table 6.8)

The 2082-2099 cm^{-1} peaks[30,31] of a-$Si_{1-x}C_x$:H films can be assigned either to SiH_2 stretching modes and or to the shift of SiH monohydride in a different environment[3] due to bonding of the Si to carbon. The observed peaks (see Table 6.8) at 2132, 2150 and 2184 cm^{-1} are due to the attachment of carbon and oxygen to SiH or SiH_2. Using the relation obtained by Lucovsky[83] the shift in the frequency can be estimated (see AppendixII). The width (FWHM) of the 2082cm^{-1} peak increases with increase in the carbon content in the film. It increases from 76 cm^{-1} for x=0.05 to 90 cm^{-1} for x=0.38. No definite trend in the width of the oxygen related peak is observed.

b. Absorption band from 2800-3000 cm^{-1}.

The absorption between 2800-3000 cm^{-1} is the C-H stretching mode. Fig 6.17 shows the result for absorbance of C-H stretch mode for different compositions. The deconvoluted C-H peak position, width, and the area under the peaks are shown in Table 6.9. The deconvoluted spectra are observed to peak at 2950 cm^{-1}, 2915cm^{-1}, 2870cm^{-1} and 2800cm^{-1}. The peaks at 2950cm^{-1} and 2870cm^{-1} are assigned to CH_3 asymmetric and symmetric stretch and the peaks at 2915cm^{-1} and 2800cm^{-1} are assigned to CH_2 asymmetric and symmetric stretch (described previously). The normalized area under these peaks increases with the increase in the carbon content of the film from 1.7×10^{-4} $cm^{-1}/\AA$ for x=0.05 to 4.6×10^{-4} $cm^{-1}/\AA$ for x=0.38. No definite trend in the widths of these peaks as a function of composition is observed. It seems that CH_3 and CH_2 stretching modes are responsible for explaining the region from 2800 cm^{-1} to 3000 cm^{-1}.

c. Absorption band between 1200- 1500 cm^{-1}.

The absorption bands between 1200-1500cm^{-1} are ascribed to the bending and scissoring modes of CH_2, CH_3, $Si(CH_3)$, $C(CH_3)$. The small peaks appear at 1250cm^{-1}, 1346cm^{-1}, 1373cm^{-1}, 1404cm^{-1},and 1454cm^{-1}. These small peaks are assigned to $Si(CH_3)$ symmetric bond bending, CH_3 symmetric bending, $C(CH_3)$ symmetric scissors, and Si-CH_2 scissoring and CH_2 scissoring, respectively (as described previously)

Thus we see that the modes in this region are due to the bending and scissoring modes of CH_3 and CH_2.

d. Absorption between 600-1200 cm^{-1}.

The absorption bands between 600-1200 cm^{-1} are ascribed to Si-H group rocking or wagging, SiH_2 and $(SiH_2)_n$ bending, Si-C and Si-O stretch modes. Fig. 6.18 represents the result for absorbance for the modes for different compositions. The deconvoluted spectra (see Fig.6.6) are observed to peak at 655 cm^{-1}, 766 cm^{-1}, and 989 cm^{-1} for the film with composition x=0.17.

The absorption band near 650 cm^{-1} is assigned to SiH group rocking or wagging. The position, width, and the area of this peak as functions of composition are presented in (Table 6.10). The normalized area under this mode increases from 9.6×10^{-4} $cm^{-1}/Å$ for x=0 to 1.59×10^{-3} $cm^{-1}/Å$ for x=0.05 and then decreases ultimately to 8.9×10^{-4} $cm^{-1}/Å$ for x=0.38. Further, the peak position also shifts to higher wavenumber from 649cm^{-1} to 678cm^{-1} with increase in the carbon content. No definite trend is observed in the width of this mode.(see Table 6.10)

The absorption band near 770 cm^{-1} is assigned to Si-C stretch. The peak position, width, and the area of this mode along with the density of Si-C bonds as functions of composition are presented in Table 6.11. The normalized area increases from 3.9×10^{-4} $cm^{-1}/Å$ to 2.51×10^{-3} $cm^{-1}/Å$ as x increases from x=0.05 to x=0.38. The peak position shifts

from 767 cm^{-1} to 785 cm^{-1} and the width increases from 76 cm^{-1} to 150 cm^{-1} as x increases from 0.05 to 0.38 (see Table 6.11). Estimates of the density of Si-C bonds in the film as a function of composition (see Table 6.11), have been obtained from the integrated absorbance of the infrared stretching mode. The cross-section of the Si-C stretch is determined to be 2.13×10^{19} cm^{-2} as described earlier (see chapter III).

The absorption band near 989 cm^{-1} is assigned to Si-O stretch. The position, width, and the area of this mode along with the density of Si-O bonds as functions of composition are presented in Table 6.12. The normalized area increases from 2.71×10^{-4} $cm^{-1}/Å$ to 1.96×10^{-3} $cm^{-1}/Å$ as x increases from x=0.05 to x=0.38. The peak position shifts from 944 cm^{-1} to 1003 cm^{-1} and the width increases as x increases from x=0.05 to x=0.38. Estimates of the density of Si-O bonds in the film as a function of composition (see Table 6.12), have been obtained from the integrated absorbance of the Si-O infrared stretching mode. The cross-section of the Si-O stretch is determined to be 1.5×10^{19} cm^{-2} as described earlier (see chapter III). Other features which are present in this region are the 860-890 cm^{-1} bands, assigned to the SiH_2 and $(SiH_2)_n$ bending modes by Brodsky[30] and Fritzsche[31]. The normalized area of various IR modes as a function of composition is shown in Fig. 6.II. Typical uncertainty in their area is about ±10% .

2. Optical Constants

For determining the values of n,k, and d from the optical measurement, we have employed the procedure of Nagendra and Thutupalli[69], which has been described earlier. Smooth values of n and k are obtained over the entire photon energy range from 1.5 eV to 4.75 eV. Typical uncertainties in d are from ± 2% to ±5% , while for n and k they are ±0.04 and ±0.02 respectively. Results for n, k, ϵ_1 , ϵ_2 and α are presented in Figs 6.19, 6.20, 6.21, 6.22, and 6.23 as functions of photon energy E. The optical constants show significant variations with composition (x).

3. Hydrogen content and the optical band gap

Estimates of the bonded hydrogen content of the films as a function of composition have been obtained from the integrated absorbances of the carbon-hydrogen and silicon-hydrogen infrared stretching modes. The cross sections of C-H and Si-H modes used are $(1.35\pm0.35)\times10^{21}$ cm^{-2} and $1.4\times10^{20} cm^{-2}$ respectively, as described earlier. The hydrogen content along with the optical band gap as a function of composition are presented in Table 6.13 .

We have used Tauc[18] relation $\epsilon_2(E)=B_1(E-E_{opt})^2/E^2$ to obtain the optical energy gap E_{opt}. Fig. 6.24 shows the results for E_{opt} for different x. The value of E_{opt} increases from 2.1 eV to 2.49 eV and the hydrogen content increases from $2.89\times10^{22} cm^{-3}$ to $5.75\times10^{22} cm^{-3}$ with increase in x from 0.05 to 0.38. Thus we see a correlation of E_{opt} with hydrogen

content (see Fig. 6.25). The correlation of E_{opt} with hydrogen content and with C content is also observed by Beyer et al.[85] The results of hydrogen content for different x is shown in Fig. 6.26 .

B. Discussions

I. SiH Stretch Vibrations

There are three effects which result in the variations of the frequency of the Si-H stretch vibrations: 1. The ligand effect arising from the electronegativity difference between silicon and its neighboring atoms 2. a solid state effect caused by the kind of environment or embedding into a dielectric medium and 3. the mechanical stress. The first effect has been exploited by Lucovsky[83] in order to rationalize the shift to higher frequencies of Si-H stretch mode for SiC_x and SiO_x. The second effect has been treated by Wagner et al[32] to elaborate the frequency difference of the stretch mode for SiH_x groups incorporated in the amorphous network and located at the inner surfaces associated with voids. Wagner et al[32] suggest that SiH_2 groups only occur on the internal surfaces due to voids. SiH groups in turn are found in compact material as well as on the inner surfaces associated with voids.

Our expermental results seem to indicate that the shift of SiH stretch originate from the change in the force constant of SiH bonds and hence reflect the contribution of both ligand and solid state effect (discussed below). There

are three factors that possibly affect the effective force constant and thus give rise to the shift in the SiH peak:

1. The presence of more electronegative neighboring atoms[83] reduces the SiH bond length caused by a transfer of valence electron on the Si atom to more electronegative neighboring atoms. This reduction in the bond length results in the increase in the effective force constant.

2. The solid state effect[32], i.e. the response of the surrounding dielectric medium, reduces the effective force constant due to the polarization of the medium surrounding the Si-H dipole.

3. Mechanical stress[86] present in the amorphous material changes the effective force constant (increases for compressive stress and decreases for tensile stress)

When the a-$Si_{1-x}C_x$:H film with x=0.17 is annealed at 350°C, the mode shifts only slightly from 2085 cm^{-1} to 2073 cm^{-1} (see Table.6.1). This strongly suggests that the remaining peak at 2073 cm^{-1} is not due to SiH_2 as commonly believed[30,83,87] but due to SiH in a different environment[32] associated with carbon and silicon. Similar observation of the shift of this mode to lower wavenumber with annealing is observed by Lin et al[88]. The commonly observed peak of a-Si:H at 2000 cm^{-1} may be due to the stretching mode of an isolated monohydride in an silicon environment. This assignment also explains why 2000 cm^{-1} peak did not appear while 2085 cm^{-1} peak shifts to lower

wavenumber and decreases. Since one would expect that once a hydrogen atom leaves SiH_2 bonds during annealing, the newly formed SiH monohydride should give rise to its characteristic peak, which is now at 2073 cm^{-1}, rather than 2000 cm^{-1}. This is because SiH monohydride is in a different environment which leads to an increase in the force constant caused by more electronegative neighboring atom like carbon. Further, if this peak is associated with SiH bonded to carbon then it should shift to higher wave number with increase in the number of more electronegative neighboring atom like carbon. This is what we observe experimentally. With increase in T_a the number of Si-C bonds increases , as evidenced from the increase in the area under this peak, and the peak position shifts to 2079 cm^{-1} for T_a=450°C and to 2095 cm^{-1} for T_a=550°C.

Thus we assign 2085 cm^{-1} peak to SiH monohydride and its variation to change in the effective force constant caused by the local environment. Initially the local environment is due to the inner surfaces associated with voids and finally the environment is due to silicon and carbon. If the local environment is due to silicon and carbon only then we can not explain the decrease in frequency from 2085 cm^{-1} to 2073 cm^{-1}.

When a small amount of carbon x=0.05 is added to a-Si:H , the normalized area under the peak (~2000 cm^{-1} for a-Si:H and ~2085 cm^{-1} for a-$Si_{1-x}C_x$:H) increases from $5.5x10^{-4}$

$cm^{-1}/Å$ to $7.1x10^{-4}$ $cm^{-1}/Å$ and decreases ultimately to $5.2x10^{-4}$ $cm^{-1}/Å$ for x=0.38 (see Table 6.8). This enhancement in the normalized area of 2082 cm^{-1} peak in the presence of small amount of carbon is due to the promotion of SiH monohydride located at the inner surfaces associated with voids. This agrees with our observation[16] that the addition of carbon to a-Si:H leads to the formation of void. Further, at a higher carbon concentration the probability of hydrogen bonded to silicon decreases whereas the preferential bonding of hydrogen and silicon with carbon takes place. This results in the decrease in the normalized area at higher carbon concentration. The variation of the normalized area of 2082 cm^{-1} peak with composition is similar to the variation of the normalized area of 650 cm^{-1} peak with composition (discussed later). Thus our observation seems to indicate that the addition of carbon to a-Si:H leads to the formation of SiH monohydrides located at the inner surfaces associated with voids but not to the formation of SiH_2 as commonly believed[4,7]. Further, the presence of a small peak at 2006 cm^{-1} along with the 2082 cm^{-1} peak for x=0.05 and the shifting of the 2082 cm^{-1} peak to 2099 cm^{-1} for x=0.38 (see Table 6.8) corroborate our assignment of 2085 cm^{-1} peak to SiH monohydride in a different environment.

The variation in the width of 2085 cm^{-1} SiH peak with annealing temperature is ascribed to the role played by hydrogen. The hydrogen compensates dangling bonds, thus

reduces the mid gap state density. Further, hydrogen also facilitates a structure with less topological disorder by reducing the average coordination number. The over all result for the change in the width (FWHM), inverse of which is a measure of order, of SiH with T_a should take into account both the effects of changing hydrogen concentration and the explicit temperature effect on the amorphous network. Following MacKenzie et al,[89] we speculate that up to T_a=350^oC the major effect of annealing is the removal of the defects associated with the network (healing of the network) which more than compensate for any loss of hydrogen content. After this process is completed the effect of hydrogen content reduction dominates the outcome. For T_a=350^oC the order caused by healing of the network outweighs the disorder caused due to the formation of dangling bonds due to hydrogen removal. This results in the decrease in the width of Si-H peak from 80 cm^{-1} to 72 cm^{-1}. Above this temperature the disorder increases by the formation of dangling bonds due to the loss of hydrogen and also due to the increase in the bond angle distortion caused by the Si-C bonds as evidenced from the increase in area under Si-C stretch, resulting in the increase in the width of SiH stretch.

The width of SiH stretch increases systematically from 76 cm^{-1} to 90 cm^{-1} as the composition x increases from 0.05 to 0.38 (see Table 6.8). This is ascribed to the disorder

caused by the bond angle distortion (discussed later) due to the formation of Si-C bonds with increase in carbon concentration.

The small peak associated with 2150 cm^{-1} is due to oxygen attached to SiH monohydride. The small oxygen related modes are formed because oxygen from the atmosphere[89] diffuses into the film through low density region of the film and forms chemical bonds with Si. With increase in T_a dangling bonds are formed and more than one oxygen atom is bonded to Si which results in the 2230 cm^{-1} peak.

The oxygen-related peak is also observed near 2132 cm^{-1} for x=0.05 and it shifts to 2184 cm^{-1} for x=0.38. This shift is due to the increase in the force constant due to carbon and oxygen (see Appendix II).

II. CH Stretch Vibrations:

The asymmetric component of the stretching vibration is higher in wavenumber than the symmetric one[30,90]. Thus it is reasonable (see Table 6.2) to attribute the 2950 cm^{-1} and 2870 cm^{-1} peaks to CH_3 asymmetric and symmetric stretch respectively. This is consistent with the fact that asymmetric and symmetric stretching modes of CH_3 in the gas phase[91], i.e 2970 and 2880 cm^{-1}, are higher than those actually measured in the film (discussed later). The 2915 and 2800 cm^{-1} peaks are attributed to $-CH_2$ asymmetric and symmetric stretch respectively. The reason we assign 2915

and $2800cm^{-1}$ to be CH_2 related is due to the fact that asymmetric and symmetric stretching mode of CH_2 in the gas phase[91], i.e. 2920 and $2830cm^{-1}$, are higher than those actually measured in the film. This is because the vibrational frequencies in solid should shift to slightly lower values due to the increase of the dielectric constant[83]. It seems that CH_3 and CH_2 stretching modes are responsible for explaining the region from 2800 cm^{-1} to 3000 cm^{-1}. When T_a increases from 250^oC to 550^oC the normalized area decreases from $3.9x10^{-4}$ to $5.4x10^{-5}$ $cm^{-1}/Å$. This decrease is due to the removal of hydrogen on annealing.

The CH modes are observed to peak at 2800, 2870, 2915, and 2950 cm^{-1} for various compositions and are ascribed to CH_2 and CH_3 symmetric and asymmetric modes, respectively (discussed above).

We have shown[16] that a void component appears in $a\text{-}Si_{1-x}C_x$:H films and increases as carbon is added to a-Si:H. The increased compositional disorder in the film as a result of alloying leads to the generation of voids due to the inability of the various components[16] to fit together perfectly. The normalized area under C-H stretch increases from $1.7x10^{-4}$ to $4.6x10^{-4}cm^{-1}/Å$ with the increase of x from 0.05 to 0.38.

The increase in the carbon content leads to an increase of void and also to the increase of normalized area under CH_3 and CH_2 stretch. This tempts one to associate voids

with CH_3 and CH_2 stretch. This association seems reasonable because during the deposition of the film, approximately 50% of the carbon atoms are introduced into the film in CH_3 configuration, as evidenced by 2870 and 2950 cm^{-1} peaks. With no available bonds to support the subsequent growth, a microvoid is definitely formed around CH_3. The association of voids with CH_3 and CH_2 stretch gets further confirmation from the observation that these modes, along with the CH_3 and CH_2 bending modes, are absent in the highly photosensitive $a\text{-}Si_{1-x}C_x$:H (x=0.16) films[92] which are compact and have higher density network. Thus we associate the void with CH_3 and CH_2 stretch and bending modes present in the amorphous network.

When T_a is increased, the hydrogen bonded in the $a\text{-}Si_{1-x}C_x$:H network is removed. This results in the elimination of all the small hydrogen related bending modes present in the range 1200 to 1500 cm^{-1}. Further, the variation in composition also led to slight changes in these modes. The small peaks in this regions are associated with CH_3 and CH_2 bending and scissoring modes. Absence of these modes in the highly photosensitive[92], dense $a\text{-}Si_{1-x}C_x$:H film led one to speculate that these modes are also void-related (discussed previously).

III. Modes in the 600-1200 cm^{-1} Region:

A lot of controversy exists in the assignment of modes in the region from 600-1200 cm^{-1}. The assignment of the 650

cm^{-1} mode to SiH group rocking or wagging differs from that of Wieder et al[3] but is in agreement with McKenzie[33]. Tavada et al[12] have not assigned this mode. Wieder et al[3] have assigned this mode to Si-C stretch. This is clearly a wrong conclusion as evidenced by our annealing study (see Tables 6.3 and 6.10). If this 650 cm^{-1} peak is assigned to Si-C stretch then there is no reason why the normalized area under this mode should drop with increase in T_a when Si and C will have an increased tendency to bond to each other. Our assignment of this 650 cm^{-1} mode to SiH rocking or wagging is reasonable because with the removal of the hydrogen from the amorphous network by annealing to high temperature, this mode should drop and should vanish ultimately. This is what we observe experimentally (see Table 6.3). The normalized area under this peak decreases from 1.14×10^{-3} $cm^{-1}/Å$ for the as-deposited film to 3.21×10^{-4} $cm^{-1}/Å$ for T_a=650°C and then vanishes ultimately, above this temperature (see Table 6.3)

When a small amount of carbon x=0.05 is added to a-Si:H , the normalized area under the 650 cm^{-1} peak increases from 9.6×10^{-4} $cm^{-1}/Å$ to 1.59×10^{-3} $cm^{-1}/Å$ and decreases ultimately to 8.9×10^{-4} $cm^{-1}/Å$ for x=0.38 (see Table 6.10). This enhancement in the normalized area of the 650 cm^{-1} peak in the presence of a small amount of carbon is due to the promotion of SiH monohydride located at the inner surfaces associated with voids (discussed previously).

This agrees with our observation[16] that the addition of carbon to a-Si:H leads to the formation of void. It may be seen that at a higher carbon concentration the probability of hydrogen bonded to silicon decreases whereas the preferential bonding of hydrogen and silicon with carbon takes place. This results in the decrease in the normalized area under 650 cm^{-1} peak at higher carbon concentrations (discussed earlier).

A lot of controversy also exists in the assignment of the 780 cm^{-1} peak. The peak is assigned to the $Si-CH_3$ rocking or wagging mode by Wieder et al.[3] However, Katayama et al[34] concluded that this peak should be assigned to the Si-C stretching mode, because this peak could be seen in the sputtered a-SiC without hydrogen. Fagen[93] showed that the SiC mode is very much broadened from that of the crystal but centered at the same frequency, 780 cm^{-1}. It should be noted, however, that Borders et al[35] found that for an ion-implanted $a\text{-}Si_{1-x}C_x$ sample, the absorption maximum for the SiC mode occurred at a somewhat lower wavenumber 700-725 cm^{-1}. They explained their result by supposing that the composition may affect the position of the absorption maximum, since their ion-implanted material was silicon-rich. McKenzie[33], however, assigned the Si-C stretching mode to have a range of wave numbers (700-800 cm^{-1})

The annealing study of the a-$Si_{1-x}C_x$:H film with x=0.17 demonstrates clearly that the 780 cm^{-1} peak should be assigned to Si-C stretch, not to Si-CH_3 rocking or wagging as done by Wieder et al[3].

If the 780 cm^{-1} peak is assigned to Si-CH_3 rocking or wagging, then the area under this peak should drop with increase in T_a due to removal of hydrogen and should vanish above T_a=650°C when all the hydrogen is removed from the network. However, the normalized area of this peak increases with T_a from $1.22x10^{-3}$ cm^{-1}/Å for the as-deposited film to $11.5x10^{-3}$ cm^{-1}/Å for T_a=1200°C (see Table 6.4). Thus we can assign the 780 cm^{-1} peak to Si-C stretch. This assignment is reasonable because when the film is annealed to higher and higher temperature, more and more hydrogen is removed from the film with the breaking of Si-H and C-H bonds. Since Si and C have an increased tendency to bond to each other, more and more Si-C bonds are formed which leads to an increase in the area under this peak. (see Table 6.4)

When the sample is annealed stress is removed. Further, due to the breaking of the Si-H and C-H bonds with increase in T_a and due to an increased tendency for Si and C to bond to each other, more and more electronegative neighboring atoms (C) are bonded to Si which is reflected in the increase in the area under Si-C stretch peak (see Table 6.4). These result in the shift in the peak position to

higher wavenumber with increase in T_a (discussed previously) and it shifts from 766 cm^{-1} for the as-deposited film to 783 cm^{-1} for T_a=650°C (see Table 6.4). Thus we assign the 780 cm^{-1} peak to the Si-C stretch and explain its variation. Too much stress along with the Si environment in the ion-implanted sample of Borders et al[35] is the reason for the shift of Si-C stretch to lower wavenumber. Thus our assignment of Si-C stretch is conclusive and, it also explains the assignment of McKenzie[33] for it to have range of wavenumbers (700-800 cm^{-1}).

Si-C bonds are much shorter (1.88 Å) than Si-Si bonds (2.35 Å) so the bond angle distortion in the amorphous network is enhanced with the formation of Si-C bonds. An increase in T_a leads to an increase in the number of Si-C bonds (see Table 6.4) which results in an increase in the bond angle distortion. This increase in the bond angle distortion increases the width (FWHM) from 124 cm^{-1} for the as-deposited film at T_s=250°C to 160 cm^{-1} for T_a=650°C. Similar observations of increases in the width of the TO peaks of Raman spectra with increase in bond angle distortion for a-Si:H are reported by Beeman et al[94].

When T_a is increased above 650°C, the following remarkable things happen :

1) There is a drop in the width (FWHM) and the width keeps decreasing with increase in T_a.

2) The Si-C peak shifts to 796 cm^{-1} for T_a=800^oC, increases to 808 cm^{-1} for T_a=1000^oC, and finally decreases to 798 cm^{-1} for T_a=1200^oC

3) The line shape changes from Gaussian to Lorentzian at 800 ^oC and remains Lorentzian with increase in T_a above 800 ^oC

These observations seems to indicate that above T_a=650^oC i.e. for T_a=800^oC there is a change from the amorphous phase to a microcrystalline phase for the following reasons:

The line shape of the SiC mode can be fitted well with a Gaussian as opposed to a Lorentzian line shape until T_a=650^oC. The fit to the Gaussian line shape indicate a Gaussian distribution of bond lengths and bond angles and hence of force constants. The distribution of bond lengths and bond angles characterizes the amorphous phase. For T_a=800^oC, the fit to the line shape changes from Gaussian to Lorentzian, which we propose as indicating the onset of crystallization, because a symmetrical Lorentzian is predicted by Nemanich et al[95] and Richter et al[96] in the Raman peak for the crystallites of boron nitride.

Further evidence for the onset of a phase change is that at T_a=800^oC there is a sudden drop in the line width, indicating increasing order due to the formation of microcrystallites. This agrees with the calculation that the TO width of the Raman spectra of Si and Ge for very small crystallites are substantially less then that of amorphous

solid[97]. With increase in T_a until 1000°C, the Si-C peak width decreases and also the peak position shifts to higher wavenumber. This we believe is due to the increase in the size of the crystallites. A similar observation of peak shift to higher wave number along with the decrease in the width with increase in the crystallite size of the TO mode of polycrystalline Si is reported by Iqbal et al[98].

When annealed to 1200°C the line shape and the frequency of a-$Si_{1-x}C_x$:H film coincides with the crystalline SiC as observed by Spitzer et al[99] (see Fig. 6.27). Thus at T_a=1200°C, SiC crystal is formed and again the peak shifts to lower wavenumber. This shift to lower wavenumber is due to the decrease in the effective force constant caused by tensile stress. The thermal expansion coefficient of the SiC crystal is greater than that of the Si crystal which generates tensile stress[100] and this leads to the decrease in the force constant and shifting of Si-C stretch to lower wavenumber. This observation seems to indicate that SiC crystal is formed at 1200°C.

We also observe a similar increase in the Si-C normalized area, peak position, and the width of Si-C from 3.9×10^{-4} $cm^{-1}/Å$, 767 cm^{-1} and 76 cm^{-1} for x=0.05 to 2.5×10^{-3} $cm^{-1}/Å$, 785 cm^{-1} and 150 cm^{-1} for x=0.38 (see Table 6.11). The shifting of the peak to the higher wavenumber with increase in carbon content is due to the increase in the effective force constant caused by the incorporation of

more electronegative neighboring atoms like carbon. The increase in the area and the width with increase in carbon content is ascribed to the increase in the number of Si-C bonds and to the increase in the bond angle distortion, respectively (discussed previously).

In addition to the 650 cm^{-1} and 780 cm^{-1} peaks another strong peak occurs near 1000 cm^{-1}. The peak near 1000 cm^{-1} is assigned to Si-O stretch. Like Si-C stretch, the area under the Si-O stretch peak increases with increase in T_a (see Table 6.5). In the a-$Si_{1-x}C_x$:H alloy films, loosely bonded hydrogen, incorporated in the inner surfaces of voids, is present. With increase in T_a, this loosely bonded hydrogen escapes and dangling bonds are created. Oxygen from the atmosphere[89] diffuses into the film through the low density region of the film and satisfies some of the dangling bonds. This is possible because Si can form polymer-like chains with oxygen. When the film is annealed to higher temperature, more and more hydrogen is removed and in the process more and more dangling bonds are produced. This results in the incorporation of more and more oxygen leading to the increase in the number of Si-O bonds which results in the increase in the area under this peak.

Like Si-C stretch, the Si-O peak shifts from 989 cm^{-1} for the as-deposited film at T_s=250^oC to 1024 cm^{-1} for T_a=650^oC and the width increases from 158 cm^{-1} for T_s=250^oC to 192 cm^{-1} for T_a=650^oC (see Table 6.5). The shifting of

the Si-O peak to higher wavenumber is due to the increase in the effective force constant caused by the reduction in stress and the incorporation of more electronegative neighboring atoms like oxygen. The increase in the width of the Si-O peak is due to the increase in the bond angle distortion (described above). When T_a is increased above 650°C, i.e T_a=800°C, there is sudden drop in the width of the Si-O stretch from 192 cm^{-1} at T_a=650°C to 148 cm^{-1} at T_a=800°C and the line shape changes from Gaussian to Lorentzian. These observations seem to indicate the formation of microcrystallites of SiO_2. Above T_a=800°C the shift of the Si-O stretch to higher wavenumber along with the decrease in its width is ascribed to the increase in the size of the crystallites.

When T_a is increased to 1200°C the Si-O bonds disappear from the film. This is because at higher temperature (~1200°C) Si react with SiO_2 forming SiO (Si + SiO_2 = 2 SiO) which volatizes at that temperature and results in the elimination of Si-O stretch.

We also observe a similar increase in the normalized area, peak position of the Si-O with increase in x, from 2.71×10^{-4} cm^{-1}/Å, 944 cm^{-1} for x=0.05 to 1.96×10^{-3} cm^{-1}/Å 1003 cm^{-1} for x=0.38. The width of Si-O peak is 188 cm^{-1} for x=0.05. Further the Si-O peak width increases from 150 cm^{-1} to 168 cm^{-1} as x increases from 0.15 to 0.38. The large value of Si-O peak width for x=0.05 is possibly due to

the uncertainty for the peak is very small compared to 649 and 767 cm^{-1} peaks (see Table 6.12). Addition of carbon in a-Si:H results in the increase in the void, leading to an increase in the presence of loosely bonded hydrogen incorporated in the inner surfaces associated with voids. When this loosely bonded hydrogen escapes and the dangling bonds are created, oxygen from the atmosphere[89] is incorporated into the film and satisfies some of the dangling bonds. The increase in x leads to an increase in the void and hence to the loosely bonded hydrogen. This loosely bonded hydrogen escapes also with time (IR spectra of the a-$Si_{1-x}C_x$:H film with x=0.05 was taken immediately after it is made and that for x=0.38 after few weeks) and creates dangling bonds and more and more oxygen are incorporated to satisfy the dangling bonds, resulting in an increase in the number of Si-O bonds. The increase in the Si-O bonds leads to an increase in the area under this peak. A similar observation of increase of the area under Si-O stretch with time is also reported by MacKenzie et al[89]. The peak shift to higher wavenumber is due to the increase in the effective force constant caused by the incorporation of more electronegative neighboring atoms like oxygen. The increase in width is ascribed to the increase in the bond angle distortion (discussed above).

The optical constants n, k, ϵ_1, ϵ_2, and α show slight variations with annealing temperature. The index of

refraction is 2.25 for the as-deposited a-$Si_{1-x}C_x$:H film (x=0.17) at T_s=250°C and it decreases to 2.15 for T_a=550°C, remains essentially constant with subsequent anneal to higher temperature till T_a=1000°C and finally drops suddenly for T_a=1200°C (see Fig. 6.7).

This slight variation in n (decrease of ~7%) with annealing temperature can be explained in the following manner. When the film is annealed to higher temperature, hydrogen leaves and presumably voids are created and these voids tend to saturate after the hydrogen is removed from the film. A similar observation of the increase of voids and subsequent saturation with increase in the annealing temperature for the a-C:H films was reported by Smith[15]. The increase of voids via the loss of hydrogen results in the decrease in n till T_a=550°C. When T_a is increased further, as the voids tends to saturate n remains essentially constant until T_a=1000°C. When T_a is increased from 1000 to 1200°C there is a sudden decrease of n which we associate with crystallization because we have clear evidence of crystallization at 1200°C from IR studies. A similar decrease of n on crystallization was observed by Brodsky et al[101] for a-Si:H films. Further, this observation agrees with the fact[102] that n values at lower energies are larger in amorphous than in crystalline phase.

The imaginary part of the index k decreases and the peak shifts to higher energy with increase in T_a (see Fig.

6.8). This decrease in k is due to the formation of much stronger Si-C and Si-O bonds with the removal of hydrogen with increase in T_a. This is in agreement with IR studies for the number of Si-C and Si-O bonds increases with increase in T_a. (see Tables 6.4 and 6.5)

At lower energies the imaginary part of the index k shows a small increase till $T_a=650^oC$ (see Fig.6.8). This may be due to the presence of some strongly absorbing Si-Si bonds which are formed with the removal of hydrogen. With increase in T_a from 650^oC to 1000^oC, k at lower energies decrease (see Fig. 6.8). This is because the weaker Si-Si bonds are broken at high T_a and are replaced by much stronger Si-C and Si-O bonds which absorbs at higher energies. When $T_a=1200^oC$ again the absorption at lower energies increases due to the removal of Si-O bonds as evidenced from the absence of Si-O stretch in the IR spectrum. The dependence of $\epsilon_1=n^2-k^2$ and $\epsilon_2=2nk$ on T_a (see Figs. 6.9 and 6.10) essentially reflect the previously discussed dependence of n and k on T_a. The absorption coefficient α (see Fig.6.11) as function of T_a essentially reflects the behavior of ϵ_2 with T_a.

The optical constants n and k, ϵ_1 and ϵ_2, and α show a significant and systematic variations with film composition from x=0.00 (a-Si:H) to x=0.38. The index of refraction n is ~3.5 for x=0.0 and decreases to ~2.0 for x=0.38 (decrease of ~43%) as the C concentration increases, see

Fig. 6.19. This decrease in n, which is consistent with the previous workers[5,13,16,73] can be attributed to the increase in the average energy gap parameter E_g which is related to n via the expression as given by the Eq. (5.1). According to the Si- and C- centered tetrahedron model[55] E_g increases from 4.76 to 13.61 eV as x increases from 0 to 1 in the a-$Si_{1-x}C_x$:H alloy series. This increase in E_g is also responsible for decreasing dispersion observed in n as the C content increases (see Fig. 6.19)

The imaginary part of the index k decreases with increase in the C concentration. This is because Si-Si bonds are replaced by Si-C bonds which absorb at higher energies (see Fig.6.20). The dependence of ϵ_1 and ϵ_2 on x (see Figs. 6.21 and 6.22) essentially reflect the previously discussed dependences of n and k on x. The α (see Fig. 6.23) essentially reflects the behavior of E with x.

The incorporation of hydrogen leads to an increase in the optical band gap (E_{opt}) of a-Si:H. This effect has been widely observed and essentially two models have been proposed for its explanation. Cody et al[41] suggest that the optical band gap is controlled by the amount of disorder and that hydrogen affects the band gap indirectly through its effect on disorder. Ley[103], on the other hand, relates gap widening mainly to the recession of the valence band edge due to hydrogenation. The recession is ascribed to the replacemant of weaker, strained Si-Si bonds by stronger Si-H

bonds. This replacement moves states from the top of the valence band to energies deep in the band, where they appear as characteristic features depending on the bonding configuration.[104] Our data (see Tables 6.6, 6.7) agree closely with Cody et al[41] where disorder is due to thermal, structural and composition effects. Further, we observe a striking correspondence between phonon order and electronic order. The phonon order is measured by the inverse of the width of the IR peak of Si-C and Si-O and the electronic order is measured by the optical band gap. The optical band gap is determined using Tauc[13] plot.

With increase in T_a, hydrogen is removed from the network (see Table 6.6) and the number of Si-C and Si-O bonds increases (see Table 6.4 and 6.5) and this results in the increase in the bond angle distortion. Disorder caused by the bond angle distortion results in the increase in the width of the Si-C and Si-O stretch peaks. This disorder also result in the decrease in the optical band gap. When T_a=800^oC and above, the bond angle distortion decreases leading to a decrease in the width of Si-C and Si-O peaks. This results in order which results in the increase in the optical band gap. (see Table 6.7)

Because the width of the Si-C stretch and the Si-O stretch have been shown to be a measure of disorder, its inverse provides a convenient measure of phonon order to which the electronic order via E_{opt}, may be compared. The

linear variation of the inverse of the widths of Si-C (Δ^{-1}_{Si-C}) and of Si-O (Δ^{-1}_{Si-O}) with E_{opt} (see Figs. 6.14 and 6.15) indicate a direct correspondence between changes in the vibrational spectra and the electronic spectra of a-$Si_{1-x}C_x$:H film. These results also indicate that the changes in E_{opt} are structural in origin and are not due to the void as has been suggested by Connell[19]. Similar observation of the narrowing of the bond angle distribution on increasing E_{opt} and narrowing of the width of TO mode of a-Si and a-Ge is reported by Ching et al[105]

The variation of hydrogen content with carbon fractional content x (see Fig. 6.26) seems to indicate that it is the carbon content which determines at a given substrate temperature the hydrogen concentration for an amorphous hydrogenated silicon carbon alloy film. This can be understood (see Beyer et al[85]) if we assume that the films form from rather hydrogen-rich plasma species and that the hydrogen content is determined by the degree of hydrogen elimination during the film growth. As the C-H binding energy (3.5 eV) is larger than the Si-H binding energy (3.1 eV), at an elevated temperature mainly hydrogen bound to carbon will remain in the film. Our data (see Table 6.13 and Fig. 6.25) seems to demonstrate that carbon content determines the hydrogen concentration which in turn controls the optical band gap. The predominance of bond-breaking hydrogen in a-$Si_{1-x}C_x$:H is in agreement with Cody's

model for a widening of the optical band gap due to hydrogen-induced strain relief.

CHAPTER VII

CONCLUSIONS AND SUGGESTIONS FOR FURTHER RESEARCH

The results for the as-deposited hydrogenated amorphous silicon carbon alloy films are given below :

1) We have undertaken an experimental determination of the optical constants (n, k, ϵ_1 , ϵ_2) for the entire a-$Si_{1-x}C_x$:H alloy series, from a-C:H (x=0) to a-Si:H (x=1).

2) We have successfully employed our proposed microstructural model based on four components (amorphous polymeric, graphitic, tetrahedral, and void) to model the measured ϵ_1 and ϵ_2 spectra. The resulting volume fractions for these four components show systematic variations with film composition and provide a very useful framework for understanding the properties of this technologically important alloy series. In particular, the use of the EMA has provided a convincing demonstration that it is the appearance of the amorphous graphitic component which limits the optical energy gap E_{opt} as the carbon content of the film increases.

3) Our experimental results for ϵ_1 and ϵ_2 are consistent with complete homogeneous chemical ordering for the Si-rich films, in which every C atom is surrounded by four Si atoms. Although the question of chemical ordering is more complicated in the C-rich films due to the presence of amorphous polymeric and graphitic components, there still appears to be a tendency for at least partial chemical

ordering. Thus we have provided for the first time a new experimental approach to the issue of chemical ordering in binary amorphous semiconducting alloy films.

Having established the result that optical constants measurements are a sensitive probe both of film microstructure and of chemical ordering in the a-$Si_{1-x}C_x$:H alloy series, an annealing study has been undertaken to study the changes in the local bonding and the structural changes in the network leading to crystallization. The results of this study are summarized below :

1) It is established that the frequency shift of Si-H stretch originates from the change in the force constant of Si-H bonds and reflects the contribution of both the ligand effect arising from the electronegativity difference between the silicon and carbon atom and a solid state effect caused by the kind of environment or embedding into a dielectric medium.

2) We have resolved the controversy regarding the assignment of various modes of a-$Si_{1-x}C_x$:H and proved conclusively that the 780 cm^{-1} peak must be assigned to Si-C stretch. We have also explained the shift of the Si-C peak with annealing temperature. Further, the controversy of the assignment of the 650 cm^{-1} peak is also resolved. This peak is assigned to Si-H group rocking or wagging modes.

3) It is established that there is a change from amorphous to microcrystalline and then to crystalline phase

with increase in the annealing temperature.

4) It is demonstrated that silicon carbide crystals can be produced from glow discharge deposition of $a\text{-}Si_{1-x}C_x{:}H$ film with subsequent anneal. This outcome is quite interesting in view of the importance of SiC in high temperature electronic devices.

5) We have undertaken an experimental determination of the optical constants (n, k, ϵ_1, ϵ_2) of an $a\text{-}Si_{1-x}C_x{:}H$ film as a function of annealing temperatures from 250 to 1200°C. A correlation of E_{opt} with hydrogen content is observed. In particular, the decrease of E_{opt} correlates well with the decrease in the hydrogen concentration. Further, a striking correspondence between phonon order and electronic order is observed. The phonon order is measured by the inverse of the width like Si-C and Si-O IR stretch and the electronic order is measured by E_{opt}.

6) It is established that the optical band gap E_{opt} is controlled by the amount of disorder and that hydrogen affects the band gap indirectly through its effect on disorder.

There still remains a considerable amount of work that could be performed to understand this technologically important alloy series. The first line of work I believe should be the improvment of our model.

Although our microstructural model is the first successful attempt to understand local bonding in terms of

optical response and has provided a useful framework for understanding the properties of this technologically important alloy series, our model is clearly an oversimplification for the structure of these films. Improvements to the model should focus on a better treatment of the optical absorption due to the localized π-like electrons associated with the amorphous graphitic component and the explicit calculations of the effects of hydrogen incorporation on the optical response of the amorphous polymeric and tetrahedral components.

Hydrogenated amorphous silicon carbon alloys are attractive materials for application in solar cells, photoreceptors, and graphic devices, since their optical gap can be continuously controlled by changing the alloy composition. However, in contrast to a-Si:H, the alloy a-$Si_{1-x}C_x$:H prepared from a conventional glow discharge decomposition technique is shown to have inferior photoelectric properties. It will be profitable to link up the photoresponses, such as photoconductivity and photoluminesence, of a-$Si_{1-x}C_x$:H alloys with the volume fractions of the microstructure like void, graphitic, polymeric and tetrahedral components. The procedure of the determination of the volume fraction of different microstructures is described in detail in this thesis. This linkage of microstructure to photoresponse will identify the microstructures and the roles they play in the deterioration

of the photoresponse of the material.

It will be highly interesting to identify the microstructures that are present in the highly photosensitive a-$Si_{1-x}C_x$:H alloys prepared recently from glow-discharge plasma using the H_2 dilution technique[92] and to link it with photoresponse. This might give clues regarding the modulation of the preparation conditions and the techniques for producing highly photosensitive a-$Si_{1-x}C_x$:H films. The realization of this will give fundamental understanding of this material and open up further possibilities for the utilization of this material.

In conclusion, even though we have asserted for the first time that optical constants measurements are sensitive probes both of film microstructure and of chemical ordering, the doors for further improvments, like the linkage of microstructure with the photoresponse and the further improvement of the model, are wide open. It is quite conceivable that a good deal of advance may yet be made in the further modification and study of hydrogenated amorphous silicon carbon alloys.

TABLE CAPTIONS

Table 5.1 Compositions, densities, and energy gaps of $a\text{-}Si_{1-x}C_x$:H films

Table 5.2 Results of EMA for volume fractions of film components for $a\text{-}Si_{1-x}C_x$:H films

Table 6.1 Variation of peak position, width, and area of Si-H stretch related mode for an $a\text{-}Si_{1-x}C_x$:H film (x = 0.17) with annealing temperatures

Table 6.2 Variation of peak position, width, and area of C-H stretch related mode for an $a\text{-}Si_{1-x}C_x$:H film (x = 0.17) with annealing temperatures

Table 6.3 Variation of peak position , width, and area of Si-H rocking or wagging for an $a\text{-}Si_{1-x}C_x$:H film (x = 0.17) with annealing temperatures

Table 6.4 Variation of peak position, width, area, and density of Si-C bonds for an $a\text{-}Si_{1-x}C_x$:H film (x=0.17) with annealing temperatures

Table 6.5 Variation of peak position, width, area, and density of Si-O bonds for an $a\text{-}Si_{1-x}C_x$:H film (x=0.17) with annealing temperatures

Table 6.5a Variation of film thickness with annealing temperatures

Table 6.6 Variations of Optical band gap and hydrogen concentration with annealing temperature for an $a\text{-}Si_{1-x}C_x$:H film (x=0.17)

Table 6.7 Variations of Optical band gap and inverse of width of Si-C, Si-O stretch with annealing temperature for an a-$Si_{1-x}C_x$:H film (x=0.17)

Table 6.8 Variation of peak position, width, and area of Si-H stretch with composition for a-$Si_{1-x}C_x$:H films

Table 6.9 Variation of peak position, width, and area of C-H stretch with composition for a-$Si_{1-x}C_x$:H films

Table 6.10 Variation of peak position, width, and area of Si-H rocking or wagging with composition for a-$Si_{1-x}C_x$:H films

Table 6.11 Variation of peak position, width, and area of Si-C stretch with composition for a-$Si_{1-x}C_x$:H films

Table 6.12 Variation of peak position, width, and area of Si-O stretch with composition for a-$Si_{1-x}C_x$:H films

Table 6.13 Variation of Optical band gap and hydrogen concentration with composition for a-$Si_{1-x}C_x$:H films

Table A.I Tetrahedron probabilities P_i for $Si_{1-x}C_x$

Table A.II Parameters for Si- and C- centered tetrahedra (defined in text)

TABLE 5.1
Compositions, densities, and energy gaps of a-$Si_{1-x}C_x$:H films.

$f(C_2H_2)$[a]	x[b]	x(EMA)[c]	ρ(g/cm)[d]	E_{opt}(eV)[e]	B_1[e]	B_T(cmeV)$^{1/2}$[f]	E_{04}(eV)[g]
1.00	1.00±0.02	1.00±0.02	1.36±0.03	2.24±0.04	1.63	273	2.81
0.91	0.96±0.03	0.96±0.01	1.36±0.03	2.36±0.05	1.63	272	2.92
0.80	0.84±0.06	0.83±0.03	1.45±0.05	2.38±0.04	1.59	268	3.00
0.72	0.68±0.05	0.68±0.04	1.58±0.02	2.68±0.07	2.34	364	2.98
0.60	0.57±0.08	0.54±0.04	1.69±0.02	2.65±0.05	3.27	464	2.78
0.50	0.38±0.06	0.38±0.01	1.86±0.04	2.49±0.05	3.98	532	2.60
0.35		0.28±0.01	1.93±0.03	2.26±0.05	5.65	708	2.25
0.20	0.07±0.06	0.16±0.01	2.00±0.04	2.21±0.05	7.60	859	2.00
0.00	0.00±0.02	0.00	2.07±0.09	1.80±0.20	5.5	700	1.75

a Fraction of C_2H_2 in glow discharge.

b Carbon fractional content of film determined from scanning Auger microprobe.

c Carbon fractional content of film determined using the effective medium approximation (EMA), see text.

d Film density.

e Optical energy-gap parameters determined from $\alpha(E)=B_1(E-E_{opt})^2/E^2$.

f B_T determined from $(\alpha E)^{1/2}=B_T(E-E_{opt})$.

g E_{04} is the energy at which the absorption coefficient α is equal to $10^4 cm^{-1}$.

TABLE 5.2
Results of EMA for volume fractions of film components.

x^a	x^b(EMA)	v^c_{ap}	v^d_{ag}	v^e_{at}	v^f_{void}	x^g_{at}
1.00	1.0(a-C:H)	0.67	0.17	0.16	0.00	1.00
0.96	0.96±0.01	0.68	0.15	0.17	0.00	0.90
0.84	0.83±0.38	0.52±0.04	0.12	0.27±0.03	0.09±0.04	0.65
0.68	0.68±0.04	0.31±0.08	0.11	0.42±0.04	0.16±0.05	0.48
0.57	0.54±0.04	0.25±0.10	0.05	0.52±0.04	0.18±0.08	0.38
0.38	0.38±0.02	0.03±0.03	0.00	0.71±0.02	0.26±0.04	0.365
	0.28±0.01	0.00±0.02	0.00	0.80	0.20	0.28
0.07	0.16±0.01	0.00	0.00	0.85±0.02	0.15±0.02	0.16
0.00	0.0(a-Si:H)	0.00	0.00	1.00	0.00	0.00

a Carbon fractional content of film determined form scanning Auger microprobe.

b Carbon fractional content of film determined using the EMA, see text.

c Volume fraction of amorphous polymeric component.

d Volume fraction of amorphous graphitic component.

e Volume fraction of amorphous tetrahedral component.

f Volume fraction of void component.

g Carbon fractional content of amorphous tetrahedral component.

TABLE 6.1

Variation of peak position, width, and area of Si-H stretch for $a\text{-}Si_{1-x}C_x$:H film (x=0.17) with annealing temperature.

T_a (°C)[a]	S[b]	d(Å)[c]	Position[d] (cm^{-1})	Width[e] (cm^{-1})	Area[f] (cm^{-1})	Normalized Area[g] (cm^{-1}/Å)
250	G	3233	2085	80	2.12	
			2151	98	0.26	7.36×10^{-4}
350	G	3259	2073	72	1.35	5.52×10^{-4}
			2132	98	0.45	
450	G	3292	2079	78	0.69	
			2150	82	0.24	2.95×10^{-4}
			2231	58	0.04	
550	G	3316	2095	80	0.13	
			2157	84	0.13	9.35×10^{-5}
			2236	60	0.05	

a Annealing temperature

b G represents Gaussian line shape.

c Thickness of the films.

d Peak position of Si-H stretch.

e Peak width of Si-H stretch.

f Area under Si-H stretch peak

g Normalized Area is Area/Thickness.

TABLE 6.2
Variation of Peak position, width, and area of C-H stretch for $a\text{-}Si_{1-x}C_x:H$ film (x=0.17) with annealing temperature.

T_a[a] (°C)	S[b]	d[c] (Å)	Position[d] (cm^{-1})	Width[e] (cm^{-1})	Area[f] (cm^{-1})	Normalized Area[g] (cm^{-1}/Å)
250	G		2800	82	0.13	
		3233	2870	48	0.46	3.9×10^{-4}
			2915	48	0.35	
			2950	34	0.31	
350	G		2800	86	0.13	
		3259	2870	54	0.48	3.6×10^{-4}
			2915	52	0.27	
			2950	38	0.30	
450	G		2800	62	0.04	
		3292	2870	48	0.26	1.6×10^{-4}
			2915	48	0.12	
			2950	54	0.12	
550	G	3316			0.18	5.4×10^{-5}

a Annealing temperature.

b G represents Gaussian line shape.

c Thickness of the film.

d Peak position of C-H stretch.

e Peak width of C-H stretch.

f Area under C-H stretch.

g Normalized Area is Area/Thickness.

TABLE 6.3

Variation of Peak Position, width, and area of Si-H rocking or wagging modes for a-$Si_{1-x}C_x$:H film (x=0.17) with annealing temperature.

T_a (°C)[a]	S[b]	d(Å)[c]	Position(cm^{-1})[d]	Width(cm^{-1})[e]	Area(cm^{-1})[f]	Normalized Area(cm^{-1}/Å)[g]
250	G	3233	655	96	3.68	1.14×10^{-3}
350	G	3259	655	92	2.81	8.62×10^{-4}
450	G	3292	670	100	2.60	7.90×10^{-4}
550	G	3316	675	116	3.00	9.04×10^{-4}
650	G	3212	630	88	1.03	3.21×10^{-4}

a Annealing temperature.

b G represents Gaussian line shape.

c Thickness of the film.

d Peak Position of Si-H rocking or wagging.

e Peak width of Si-H rocking or wagging.

f Area under Si-H rocking or wagging mode.

g Normalized Area is Area/Thickness.

TABLE 6.4

Variation of Peak position, width, and area of Si-C stretch for a-$Si_{1-x}C_x$:H film (x=0.17) with annealing temperature.

T_a^{a} (°C)	S^{b}	d^{c} (Å)	Position^{d} (cm^{-1})	Width^{e} (cm^{-1})	Area^{f} (cm^{-1})	Normalized^{g} Area (cm)	N^{h}_{Si-C} (cm^{-3})
250	G	3233	766	124	3.93	1.22×10^{-3}	7.78×10^{21}
350	G	3259	768	132	4.17	1.28×10^{-3}	8.17×10^{21}
450	G	3292	771	130	6.20	1.88×10^{-3}	1.20×10^{22}
550	G	3316	779	148	13.4	4.04×10^{-3}	2.53×10^{22}
650	G	3212	783	160	20.9	6.50×10^{-3}	4.07×10^{22}
800	L	2980	796	126	26.4	8.86×10^{-3}	5.46×10^{22}
900	L	2855	803	116	27.2	9.53×10^{-3}	5.82×10^{22}
1000	L	2699	808	104	28.1	10.4×10^{-3}	6.32×10^{22}
1200	L	2580	798	68	29.6	11.5×10^{-3}	7.04×10^{22}

a Annealing temperature.

b G and L represent Gaussian and Lorentzian line shape respectively.

c Thickness of the film.

d Peak position of the Si-C stretch.

e Peak width of the Si-C stretch.

f Area under the Si-C stretch.

g Normalized Area is Area/Thickness

h Density of Si-C bonds is obtained using Eq. 3.24 (see text).

TABLE 6.5
Variation of Peak Position, width, and area of Si-O stretch for $a\text{-}Si_{1-x}C_x$:H film (x=0.17) with annealing temperature.

T_a[a] (°C)	S[b]	d[c] (Å)	Position[d] (cm^{-1})	Width[e] (cm^{-1})	Area[f] (cm^{-1})	Normalized[g] Area (cm/A)	N_{Si-O}[h] (cm^{-3})
250	G	3233	989	158	2.29	7.08×10^{-4}	2.46×10^{21}
350	G	3259	1004	148	3.89	1.19×10^{-3}	4.10×10^{21}
450	G	3292	1003	154	6.68	2.03×10^{-3}	6.98×10^{21}
550	G	3316	1013	168	10.2	3.08×10^{-3}	1.05×10^{22}
650	G	3212	1024	192	14.2	4.42×10^{-3}	1.49×10^{22}
800	L	2980	1042	148	14.1	4.73×10^{-3}	1.56×10^{22}
900	L	2855	1057	132	13.6	4.76×10^{-3}	1.56×10^{22}
1000	L	2699	1070	126	14.1	5.22×10^{-3}	1.68×10^{22}
1200			no longer present				

a Annealing temperature.

b G and L represent Gaussian and Lorentzian line shape respectively.

c Thickness of the film.

d Peak position of the Si-O stretch.

e Peak width of the Si-O stretch.

f Area under the Si-O stretch peak.

g Normalized Area is Area/Thickness.

h Density of Si-O bonds is obtained using Eq. 3.28 (see text).

Table 6.5a

T_a[a] (°C)	d[b] (Å)	d[c] (Å)
250	3233	1251
350	3259	1249
450	3292	1220
550	3316	1165
650	3212	1035
800	2980	963
900	2855	922
1000	2699	886
1200	2580	866

a Annealing temperature

b Corresponds to the thickness of the a-$Si_{1-x}C_x$:H (x=0.17) film used for IR measurements

c Corresponds to the thickness of the a-$Si_{1-x}C_x$:H (x=0.17) film used for optical constants measurements

TABLE 6.6

Variation of Optical band gap and hydrogen concentration for $a\text{-}Si_{1-x}C_x{:}H$ film (x=0.17) with annealing temperature.

T_a^{a} (°C)	E_{opt}^{b} (eV)	N_{Si-H}^{c} (cm^{-3})	N_{C-H}^{d} (cm^{-3})	N_{total}^{e} (cm^{-3})
250	2.35	1.13×10^{22}	4.14×10^{22}	5.27×10^{22}
350	2.27	8.45×10^{21}	3.88×10^{22}	4.73×10^{22}
450	2.2	4.58×10^{21}	1.72×10^{22}	2.18×10^{22}
550	2.1	1.52×10^{21}	5.82×10^{21}	7.34×10^{21}

a Annealing temperature

b Optical energy gap parameters determined from $\epsilon_2(E)=B_1(E-E_{opt})^2/E^2$ and the error associated with E_{opt} is ± 0.05

c Density of Si-H bonds is obtained using Eq. 3.21 (see text)

d Density of C-H bonds is obtained using Eq. 3.23 (see text)

e Total hydrogen atomic concentration bonded to silicon and carbon.

TABLE 6.7
Variation of Optical band gap, and inverse of width of Si-C and Si-O stretch for a-$Si_{1-x}C_x$:H (x=0.17) with annealing temperature.

T_a^a (°C)	E_{opt}^b (eV)	$\Delta^{-1\,c}$ Si-C (cm)	$\Delta^{-1\,d}$ Si-O (cm)
250	2.35	8.1×10^{-3}	6.3×10^{-3}
350	2.27	7.6×10^{-3}	6.8×10^{-3}
450	2.2	7.7×10^{-3}	6.5×10^{-3}
550	2.1	6.8×10^{-3}	6.0×10^{-3}
650	2.0	6.3×10^{-3}	5.2×10^{-3}
800	2.1	7.9×10^{-3}	6.8×10^{-3}
900	2.15	8.6×10^{-3}	7.6×10^{-3}
1000	2.2	9.6×10^{-3}	8.0×10^{-3}
1200	2.2	14.7×10^{-3}	

a Annealing temperature.

b Optical energy gap parameters determined from $\epsilon_2(E)=B_1(E-E_{opt})^2/E^2$ and the error associated with E_{opt} is ± 0.05

c Inverse of width of Si-C stretch.

d Inverse of width of Si-O stretch.

TABLE 6.8

Variation of Peak position, width, and area of Si-H stretch for $a\text{-}Si_{1-x}C_x{:}H$ film with composition.

x[a]	S[b]	d[c](Å)	Position[d](cm⁻¹)	Width[e](cm⁻¹)	Area[f](cm⁻¹)	Normalized[g] Area(cm⁻¹/Å)
0.0	G	13000	2004	102	6.25	
			2084	100	0.90	5.5×10^{-4}
			2006	102	0.31	
0.05	G	3282	2082	76	1.96	7.1×10^{-4}
			2132	110	0.06	
0.15	G	2255	2082	80	1.69	8.0×10^{-4}
			2153	88	0.13	
0.17	G	3233	2085	80	2.12	7.4×10^{-4}
			2151	98	0.26	
0.38	G	2135	2099	90	1.02	5.2×10^{-4}
			2184	74	0.10	

a Carbon fractional content of the film determined from scanning Auger microprobe.

b G represents Gaussian line shape.

c Thickness of the film.

d Peak position of Si-H stretch.

e Peak width of Si-H stretch.

f Area under Si-H stretch.

g Normalized Area is Area/Thickness.

TABLE 6.9

Variation of Peak Position, width, and area of C-H stretch for a-$Si_{1-x}C_x$:H with composition.

x[a]	S[b]	d(Å)[c]	Position(cm^{-1})[d]	Width(cm^{-1})[e]	Area(cm^{-1})[f]	Normalized Area(cm^{-1}/Å)[g]
			2800	84	0.05	
0.05	G	3282	2870	52	0.20	1.7×10^{-4}
			2915	48	0.15	
			2950	34	0.15	
			2800	74	0.07	
0.15	G	2255	2870	48	0.35	4.1×10^{-4}
			2915	48	0.21	
			2950	40	0.29	
			2800	82	0.13	
0.17	G	3233	2870	48	0.46	3.9×10^{-4}
			2915	48	0.35	
			2950	34	0.31	
			2800	94	0.05	
0.38	G	2135	2800	54	0.39	4.6×10^{-4}
			2915	60	0.24	
			2950	54	0.30	

a Carbon fractional content of the film determined from scanning Auger microprobe.

b G represents Gaussian line shape.

c Thickness of the film.

d Peak position of the C-H stretch.

e Peak width of C-H stretch.

f Area under the C-H stretch peak.

g Normalized Area is Area/Thickness.

TABLE 6.10

Variation of peak position, width, and area of Si-H rocking or wagging for a-$Si_{1-x}C_x$:H with composition

x[a]	S[b]	d[c](Å)	Position[d](cm^{-1})	Width[e](cm^{-1})	Area[f](cm^{-1})	Normalized[g] Area(cm^{-1}/Å)
0.00	G	13000	637	100	12.53	9.60×10^{-4}
0.05	G	3282	649	96	5.21	1.59×10^{-3}
0.15	G	2255	662	110	3.71	1.65×10^{-3}
0.17	G	3233	655	96	3.68	1.13×10^{-3}
0.38	G	2135	678	130	1.90	8.9×10^{-4}

a Carbon fractional content of the film determined from scanning Auger microprobe.

b G represents Gaussian line shape.

c Thickness of the film.

d Peak position of Si-H rocking or wagging mode.

e Peak width of Si-H rocking or wagging mode.

f Area under Si-H rocking or wagging mode.

g Normalized Area is Area/Thickness.

TABLE 6.11

Variation of Peak position, width, and area of Si-C stretch for a-$Si_{1-x}C_x$:H with composition.

x[a]	S[b]	d[c](Å)	Position[d](cm^{-1})	Width[e](cm^{-1})	Area[f](cm^{-1})	Normalized[g] Area(cm^{-1}/Å)	N_{Si-C}[h](cm^{-3})
0.05	G	3282	767	76	1.28	3.9×10^{-4}	2.5×10^{21}
0.15	G	2255	778	98	2.19	9.7×10^{-4}	6.12×10^{21}
0.17	G	3233	766	124	3.93	1.22×10^{-3}	7.70×10^{21}
0.38	G	2135	785	150	5.35	2.51×10^{-3}	1.57×10^{22}

a Carbon fractional content of the film determined from scanning Auger microprobe.

b G represents Gaussian line shape.

c Thickness of the film.

d Peak position of the Si-C stretch.

e Peak width of the Si-C stretch.

f Area under the Si-C stretch.

g Normalized Area is Area/Thickness

h Density of Si-C bonds is obtained using Eq. 3.24 (see text)

TABLE 6.12

Variation of Peak position, Width, and area of Si-O stretch for a-$Si_{1-x}C_x$:H with composition.

x[a]	S[b]	$d(\text{Å})$[c]	Position(cm^{-1})[d]	Width(cm^{-1})[e]	Area(cm^{-1})[f]	Normalized Area($cm^{-1}/\text{Å}$)[g]	N_{Si-O}(cm^{-3})[h]
0.05	G	3282	944	188	0.89	2.71×10^{-4}	9.94×10^{20}
0.15	G	2255	982	150	1.34	5.94×10^{-4}	2.08×10^{21}
0.17	G	3233	989	158	2.29	7.08×10^{-4}	2.44×10^{21}
0.38	G	2135	1003	168	4.19	1.96×10^{-3}	6.74×10^{21}

a Carbon fractional content of film determined from scanning Auger microprobe.

b G represents Gaussian line shape.

c Thickness of the film.

d Peak position of the Si-O stretch.

e Peak width of the Si-O stretch.

f Area under the Si-O stretch.

g Normalized Area is Area/Thickness.

h Density of Si-O bonds is obtained using Eq. 3.28 (see text)

TABLE 6.13
Variation of Optical band gap and hydrogen concentration with composition for a-$Si_{1-x}C_x$:H films

x^a	E_{opt}^b (eV)	N_{Si-H}^c (cm^{-3})	N_{C-H}^d (cm^{-3})	N_{total}^e (cm^{-3})
0.00	1.97	8.87×10^{21}		8.87×10^{21}
0.05	2.1	1.09×10^{22}	1.80×10^{22}	2.89×10^{22}
0.15	2.30	1.24×10^{22}	4.48×10^{22}	5.72×10^{22}
0.17	2.35	1.12×10^{22}	4.10×10^{22}	5.22×10^{22}
0.38	2.49	8.04×10^{21}	4.94×10^{22}	5.75×10^{22}

a Carbon fractional content of the film determined from scanning Auger microprobe.

b Optical energy gap parameters determined from $\epsilon_2(E)=B(E-E_{opt})^2/E^2$ and the error associated with E_{opt} is ± 0.05

c Density of Si-H bonds is obtained using Eq. 3.21 (see text)

d Density of C-H bonds is obtained using Eq. 3.23 (see text)

e Total hydrogen atomic concentration bonded to silicon and carbon

TABLE Tetrahedron probabilities P_i for $Si_{1-x}C_x$.

Tetrahedron	No chemical ordering	Complete chemical ordering with homogeneous dispersion		Complete chemical ordering with phase separation	
		Si-rich $(0 \le x \le 0.5)$	C-rich $(0.5 \le x \le 1)$	Si-rich	C-rich
(1) Si-Si_4	$(1-x)^5$	$(1-x)\left[\frac{1-2x}{1-x}\right]^4$	0	$(1-2x)$	0
(2) Si-Si_3C	$4x(1-x)^4$	$4(1-x)\left[\frac{1-2x}{1-x}\right]^3\left[\frac{x}{1-x}\right]$	0	0	0
(3) Si-Si_2C_2	$6x^2(1-x)^3$	$6(1-x)\left[\frac{1-2x}{1-x}\right]^2\left[\frac{x}{1-x}\right]^2$	0	0	0
(4) Si-SiC_3	$4x^3(1-x)^2$	$4(1-x)\left[\frac{1-2x}{1-x}\right]\left[\frac{x}{1-x}\right]^3$	0	0	0
(5) Si-C_4	$x^4(1-x)$	$(1-x)\left[\frac{x}{1-x}\right]^4$	$(1-x)$	x	$(1-x)$
(6) C-Si_4	$x(1-x)^4$	x	$x\left[\frac{1-x}{x}\right]^4$	x	$(1-x)$
(7) C-Si_3C	$4x^2(1-x)^3$	0	$4x\left[\frac{1-x}{x}\right]^3\left[\frac{2x-1}{x}\right]$	0	0
(8) C-Si_2C_2	$6x^3(1-x)^2$	0	$6x\left[\frac{1-x}{x}\right]^2\left[\frac{2x-1}{x}\right]^2$	0	0
(9) C-SiC_3	$4x^4(1-x)$	0	$4x\left[\frac{1-x}{x}\right]\left[\frac{2x-1}{x}\right]^3$	0	0
(10) C-C_4	x^5	0	$x\left[\frac{2x-1}{x}\right]^4$	0	$(2x-1)$

TABLE Parameters for Si- and C-centered tetrahedra (defined in text).

Tetrahedron	$\langle r \rangle$ (Å)	k_F (Å^{-1})	k_s (Å^{-1})	E_H (eV)	C (eV)	E_g (eV)	C_2	C_1	V_t (Å^3)
(1) Si-Si_4	1.176	1.809	2.085	4.76	0	4.76	1	1	20.02
(2) Si-Si_3C	1.118	1.910	2.142	5.40	0.84	5.46	0.871	0.893	17.01
(3) Si-Si_2C_2	1.059	2.016	2.201	6.18	1.78	6.43	0.740	0.759	14.45
(4) Si-SiC_3	1.001	2.133	2.264	7.11	2.85	7.66	0.621	0.632	12.21
(5) Si-C_4	0.942	2.257	2.329	8.26	4.08	9.21	0.517	0.520	10.30
(6) C-Si_4	0.942	2.257	2.329	8.26	4.08	9.21	0.517	0.520	10.30
(7) C-Si_3C	0.899	2.371	2.387	9.28	3.21	9.82	0.485	0.530	8.88
(8) C-Si_2C_2	0.856	2.492	2.447	10.47	2.26	10.71	0.444	0.516	7.65
(9) C-SiC_3	0.813	2.623	2.510	11.90	1.13	11.95	0.398	0.483	6.56
(10) C-C_4	0.771	2.762	2.576	13.62	0	13.62	0.349	0.434	5.62

FIGURE CAPTION

Fig. 2.1 (a) Schematic density of states in an amorphous semiconductor with localized states shown as the shaded regions.(b) Mobility gap, E_v to E_c, corresponding to accompanying density of states.

Fig. 2.2 Absorption edge of an amorphous semiconductor. Region A (G-B) represents a shoulder in the optical absorption for < 1 cm^{-1}, region B (T-B) corresponds to an exponential region for $1\ cm^{-1} < \alpha < 10^4\ cm^{-1}$, Region C (B-B) refers to a slowly varying regime for $> 10^4\ cm^{-1}$ (see text).

Fig. 2.3 Infrared spectrum of a hydrogenated amorphous silicon carbon alloy film, x=0.50

Fig. 3.1 Diagram of an amorphous film on a substrate.

Fig. 4.1 Schematic of rf glow discharge deposition system used in the preparation of samples used in this study.

Fig. 4.2 Spatial distribution of potentials in an rf reactor. V_p, V_f, and V_s are the plasma potential, floating potential and sheath potential, respectively.

Fig. 4.3 Detailed diagram of the sample electrode assembly used in sample preparation.

Fig. 4.4 Gas mixing and flow control system.

Fig. 4.5 Gas neutralization and disposal system.

Fig. 4.6 The measured transmittance (T) and the reflectances from both air (R_a) and substrate (R_s) side of an a-$Si_{1-x}C_x$:H (x=0.17) film vs wavelength.

Fig. 4.7 Tauc plot for the determination of the optical energy gap parameter E_{opt} from the energy dependence of ϵ_2 for an a-$Si_{1-x}C_x$:H film.

Fig. 5.1 Index of refraction n vs photon energy for nine a-$Si_{1-x}C_x$:H films. Carbon contents as listed have been determined via the EMA (see text and Table 5.1)

Fig. 5.2 Extinction coefficient k vs photon energy for nine a-$Si_{1-x}C_x$:H films. Carbon contents as listed have been determined via the EMA (see text and Table 5.1)

Fig. 5.3 Real part ϵ_1 of the dielectric constant vs photon energy for nine a-$Si_{1-x}C_x$:H films. Carbon contents as listed have been determined via the EMA (see text and Table 5.1)

Fig. 5.4 Imaginary part ϵ_2 of the dielectric constant vs photon energy for nine a-$Si_{1-x}C_x$:H films. Carbon contents as listed have been determined via the EMA (see text and Table 5.1)

Fig. 5.5 Absorption coefficient vs photon energy for nine a-$Si_{1-x}C_x$:H films. Carbon contents 1: x=0.00 ; 2: x=0.16 3: x=0.28 ; 4: x=0.38 ; 5: x=0.54 ; 6: x=0.68 ; 7: x=0.83 ; 8: x=0.96 ; 9: x=1.00

Fig. 5.6 ϵ_1 vs photon energy for a-$Si_{0.62}C_{0.38}$:H. Curve 1: experimental points; Curve 2: complete chemical ordering with homogeneous dispersion; Curve 3: no chemical ordering; Curve 4: complete chemical ordering with phase separation.

Fig. 5.7 ϵ_2 vs photon energy for a-$Si_{0.62}C_{0.38}$:H see Fig. 5.6 for labelling of curves.

Fig. 5.8 Volume fractions of the various components of the a-$Si_{1-x}C_x$:H films as functions of 1-x (Si content). v_{at} represent amorphous tetrahedral, v_{ap} represents amorphous polymeric, v_{ag} represents amorphous graphitic, and v_v represents void.

Fig. 5.9 Atomic fractions of the three elements present in these a-$Si_{1-x}C_x$:H films, as function of 1-x (Si content)

Fig. 5.10 ϵ_1 and ϵ_2 vs photon energy for a-$Si_{0.32}C_{0.68}$:H Comparison between experiment and theoretical prediction of EMA for complete chemical ordering with homogeneous dispersion.

Fig. 5.11 ϵ_1 and ϵ_2 vs photon energy for a-$Si_{0.84}C_{0.16}$:H Comparison between experiment and theortical prediction of EMA for complete chemical ordering with homogeneous dispersion.

Fig. 5.12 Optical energy gap E_{opt} vs volume fraction v_{ag} of amorphous graphitic component for two sets of samples: a-$Si_{1-x}C_x$:H (this work) and a-C:H (Ref 15)

Fig. 5.13 Optical energy gap E_{opt} vs carbon fraction x both for experiment and theory. Curve 1: prediction for complete chemical order with homogeneous dispersion; Curve 2: Complete chemical order with phase separation; Curve 3: no chemical order.

Fig. 6.1 Absorbance of Si-H stretch vs wavenumber for an as-deposited (T_s=250^oC) a-$Si_{1-x}C_x$:H film with x=0.17 and following anneals at the indicated temperatures.

Fig. 6.2 Deconvoluted spectrum for the absorbance of Si-H stretch vs wavenumber for an as-deposited (T_s=250°C) a-$Si_{1-x}C_x$:H film, with x=0.17. Curve 1: experimental points; Curve 2: corresponds to 2035 cm^{-1} peak; Curve 3: corresponds to 2151cm^{-1} peak; Curve 4: corresponds to the fit (see text)

Fig. 6.3 Absorbance of C-H stretch vs wavenumber for an as-deposited (T_s=250°C) a-$Si_{1-x}C_x$:H film, with x=0.17 and following anneals at the indicated temperatures.

Fig. 6.4 Deconvoluted spectrum for the absorbance of C-H stretch vs wavenumber for an as-deposited (T_s=250°C) a-$Si_{1-x}C_x$:H film, with x=0.17. Curve 1: experimental points; Curve 2: corresponds to 2800 cm^{-1} peak; Curve 3: corresponds to 2870 cm^{-1} peak; Curve 4: corresponds to 2915 cm^{-1} peak; Curve 5: corresponds to 2950 cm^{-1} peak; Curve 6: corresponds to the fit (see text)

Fig. 6.5a Absorbance of Si-H rocking or wagging, Si-C, and Si-O stretch vs wavenumber for an as-deposited (T_s=250°C) a-$Si_{1-x}C_x$:H film, with x=0.17 and following anneals at the indicated temperatures.

Fig. 6.5b Absorbance of Si-H rocking or wagging, Si-C, and Si-O stretch vs wavenumber for an a-$Si_{1-x}C_x$:H film, with x=0.17 and following anneals at the indicated temperatures.

Fig. 6.6a Deconvoluted spectrum for the absorbance of Si-H rocking or wagging, Si-C, and Si-O stretch vs wavenumber for an as-deposited (T_s=250^oC) a-$Si_{1-x}C_x$:H film with x=0.17. Curve 1: experimental points; Curve 2: corresponds to Si-H rocking or wagging (655 cm^{-1}); Curve 3: corresponds to Si-C stretch (765 cm^{-1}); Curve 4: corresponds to Si-O stretch (989 cm^{-1}); Curve 5: corresponds to the fit (see text).

Fig. 6.6b The peak positions and the widths of Si-C stretch vs annealing temperature for an a-$Si_{1-x}C_x$:H film with x=0.17

Fig. 6.6c The peak positions and the widths of Si-O stretch vs annealing temperature for an a-$Si_{1-x}C_x$:H film with x=0.17

Fig. 6.7 Index of refraction n vs photon energy for an as-deposited (T_s=250^oC) a-$Si_{1-x}C_x$:H film, with x=0.17 and following anneals at the indicated temperatures.

Fig. 6.8 Extinction coefficient k vs photon energy for an as-deposited (T_s=250^oC) a-$Si_{1-x}C_x$:H film, with x=0.17 and following anneals at the indicated temperatures.

Fig. 6.9 Real part ϵ_1 of the dielectric constant vs photon energy for an as-deposited (T_s=250^oC) a-$Si_{1-x}C_x$:H film, with x=0.17 and following anneals at the indicated temperatures.

Fig. 6.10 Imaginary part ϵ_2 of the dielectric constant vs photon energy for an as-deposited (T_s=250^oC) a-$Si_{1-x}C_x$:H film with x=0.17 and following anneals at the indicated temperatures.

Fig. 6.11 Absorption coefficient vs photon energy for an as-deposited (T_s=250°C) a-$Si_{1-x}C_x$:H film, with x=0.17 and following anneals at the indicated temperatures.

Fig. 6.12 Optical energy gap E_{opt} vs annealing temperature for an as-deposited (T_s=250°C) a-$Si_{1-x}C_x$:H film, with x=0.17

Fig. 6.13 Optical energy gap E_{opt} vs hydrogen concentration for an as-deposited (T_s=250°C) a-$Si_{1-x}C_x$:H film, with x=0.17 and following anneals at the indicated temperatures.

Fig. 6.14 Inverse of the width (FWHM) of Si-C stretch (Δ^{-1}_{Si-C}) vs optical energy gap E_{opt} for an as-deposited (T_s=250°C) a-$Si_{1-x}C_x$:H film, with x=0.17 and following anneals at the indicated temperatures (see text).

Fig. 6.15 Inverse of the width (FWHM) of Si-O stretch (Δ^{-1}_{Si-O}) vs optical energy gap E_{opt} for an as-deposited (T_s=250°C) a-$Si_{1-x}C_x$:H film, with x=0.17 and following anneals at the indicated temperatures (see text).

Fig. 6.16 Absorbance of Si-H stretch vs wavenumber for a-$Si_{1-x}C_x$:H films. Carbon contents as listed have been determined via SAM (see text).

Fig. 6.17 Absorbance of C-H stretch vs wavenumber for a-$Si_{1-x}C_x$:H films. Carbon contents as listed have been determined via SAM (see text).

Fig. 6.18 Absorbance of Si-H rocking or vagging, Si-C, and Si-O stretch vs wavenumber for a-$Si_{1-x}C_x$:H films. Carbon contents as listed have been determined via SAM (see text).

Fig. 6.19 Index of refraction n vs photon energy for $a\text{-}Si_{1-x}C_x{:}H$ films. Carbon contents as listed have been determined via SAM (see text).

Fig. 6.20 Extinction coefficient k vs photon energy for $a\text{-}Si_{1-x}C_x{:}H$ films. Carbon contents as listed have been determined via SAM (see text).

Fig. 6.21 Real part ϵ_1 of the dielectric constant vs photon energy for $a\text{-}Si_{1-x}C_x{:}H$ films. Carbon contents as listed have been determined via SAM (see text).

Fig. 6.22 Imaginary part ϵ_2 of the dielectric constant vs photon energy for $a\text{-}Si_{1-x}C_x{:}H$ films. Carbon contents as listed have been determined via SAM (see text).

Fig. 6.23 Absorption coefficient vs photon energy for $a\text{-}Si_{1-x}C_x{:}H$ films. Carbon contents as listed have been determined via SAM (see text).

Fig. 6.24 Optical energy gap E_{opt} vs carbon content (x) for $a\text{-}Si_{1-x}C_x{:}H$ films. Carbon contents as listed have been determined via SAM (see text).

Fig. 6.25 Optical energy gap E_{opt} vs hydrogen concentration for $a\text{-}Si_{1-x}C_x{:}H$ films. Carbon contents as listed have been determined via SAM (see text).

Fig. 6.26 Hydrogen concentration vs carbon content (x) for $a\text{-}Si_{1-x}C_x{:}H$ films. Carbon contents as listed have been determined via SAM (see text).

Fig. 6.27 a:IR spectra of crystalline SiC as observed in the a-$Si_{1-x}C_x$:H (x=0.17) film annealed at 1200°C b: IR spectra of crystalline SiC as shown in Spitzer (see Ref.99)

Fig. 6.I The normalized area (area/thickness) of various IR modes vs annealing temperature for an a-$Si_{1-x}C_x$:H film with x=0.17 . Curve 1: corresponds to Si-H stretch; Curve 2: corresponds to C-H stretch; Curve 3: corresponds to Si-H rocking or wagging; Curve 4: corresponds to Si-O stretch; Curve 5: corresponds to Si-C stretch (see text)

Fig. 6.II The normalized area (area/thickness) of various IR modes vs carbon content (x) for a-$Si_{1-x}C_x$:H films. Curve 1: corresponds to Si-H stretch; Curve 2: corresponds to C-H stretch; Curve 3: corresponds to Si-H rocking or wagging; Curve 4: corresponds to Si-O stretch; Curve 5: corresponds to Si-C stretch. Carbon contents as listed have been determined via SAM (see text)

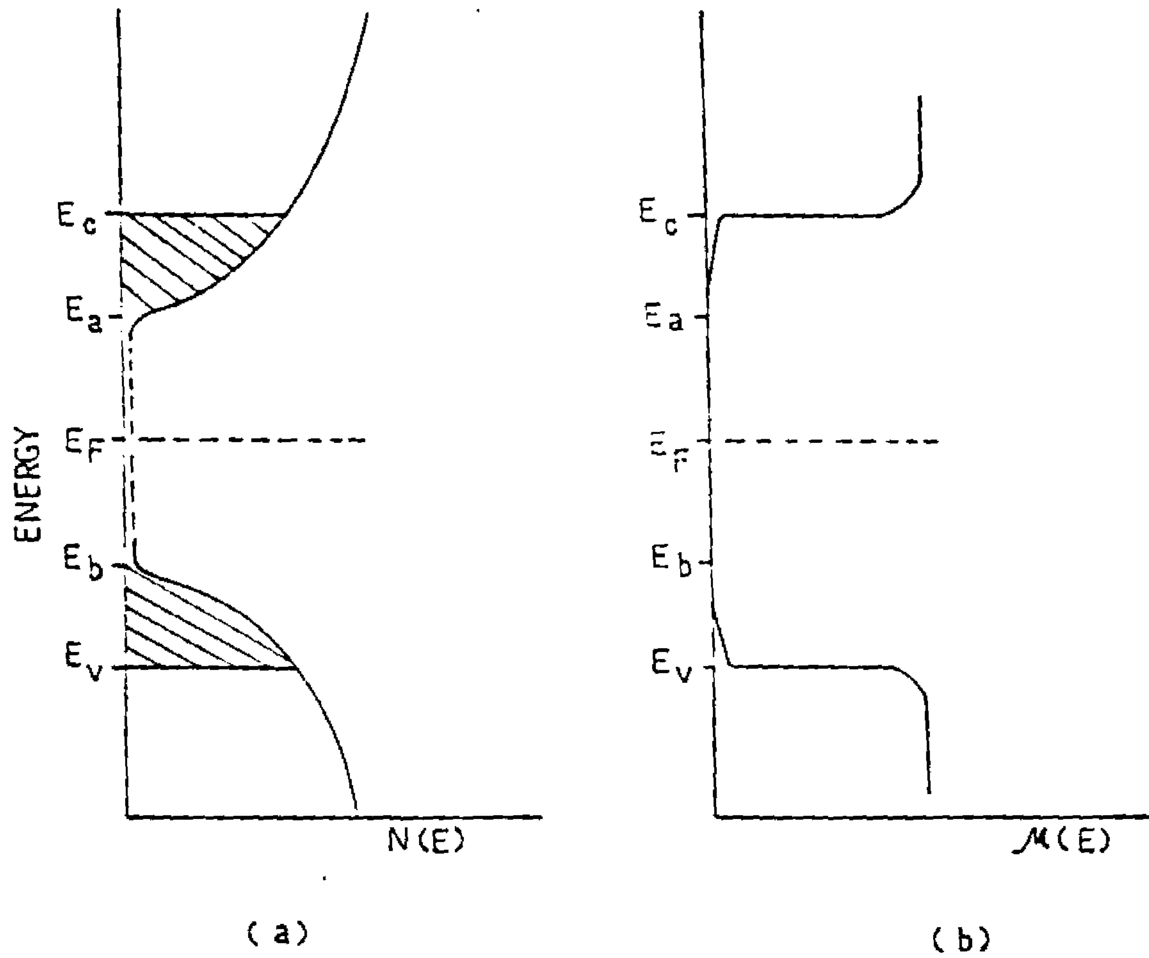

FIG. 2.1

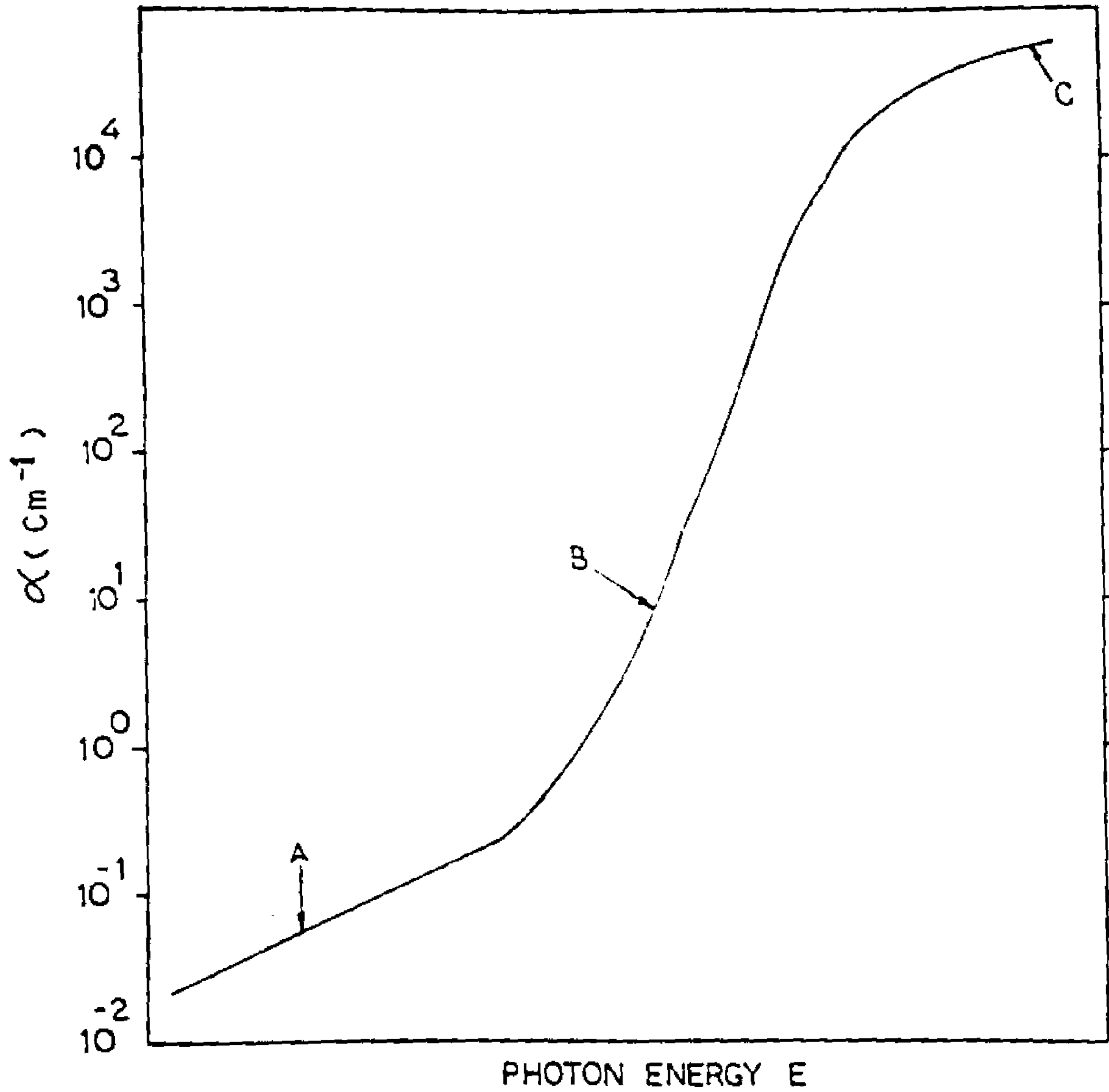

FIG. 2.2

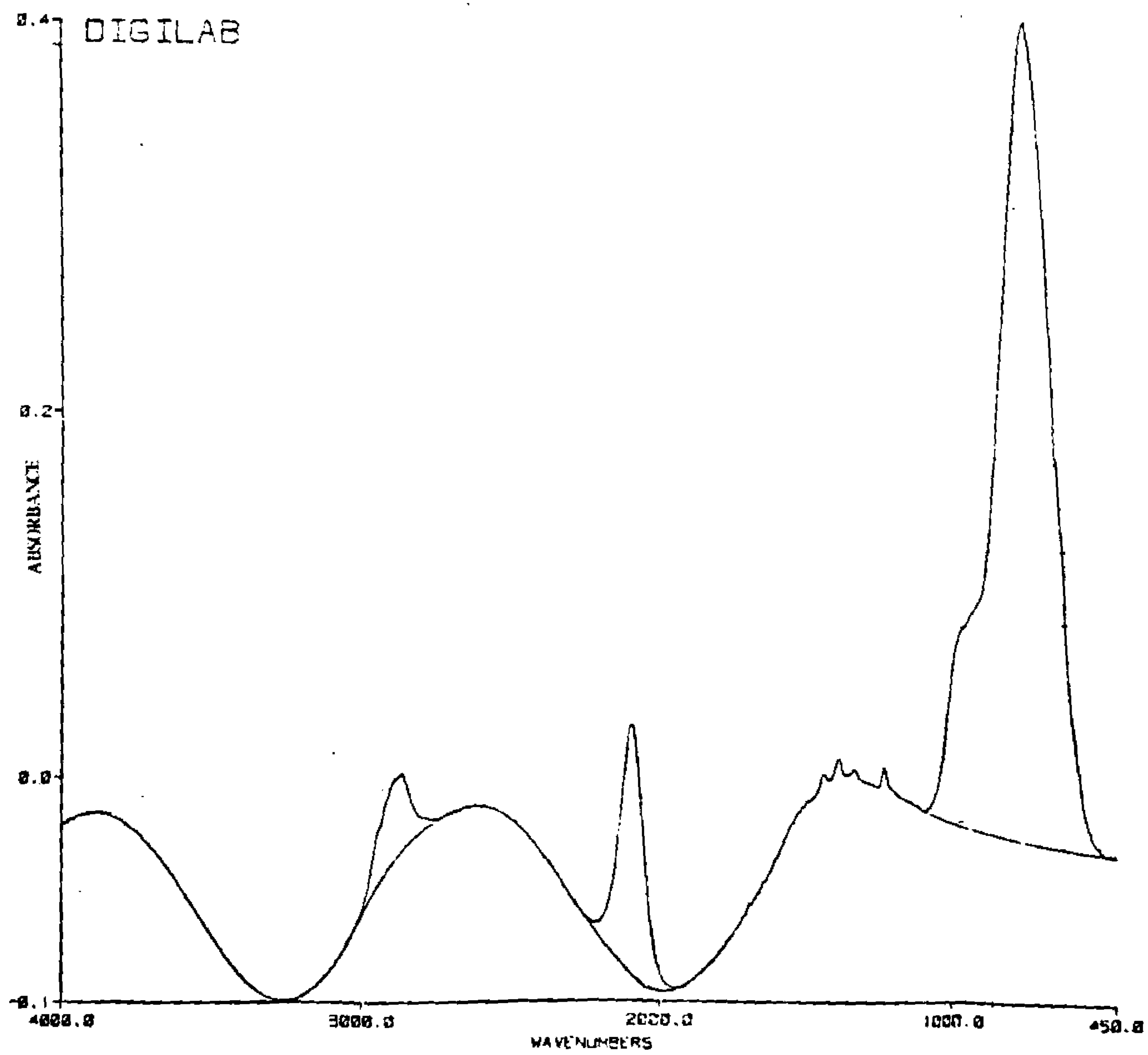

FIG. 2·3

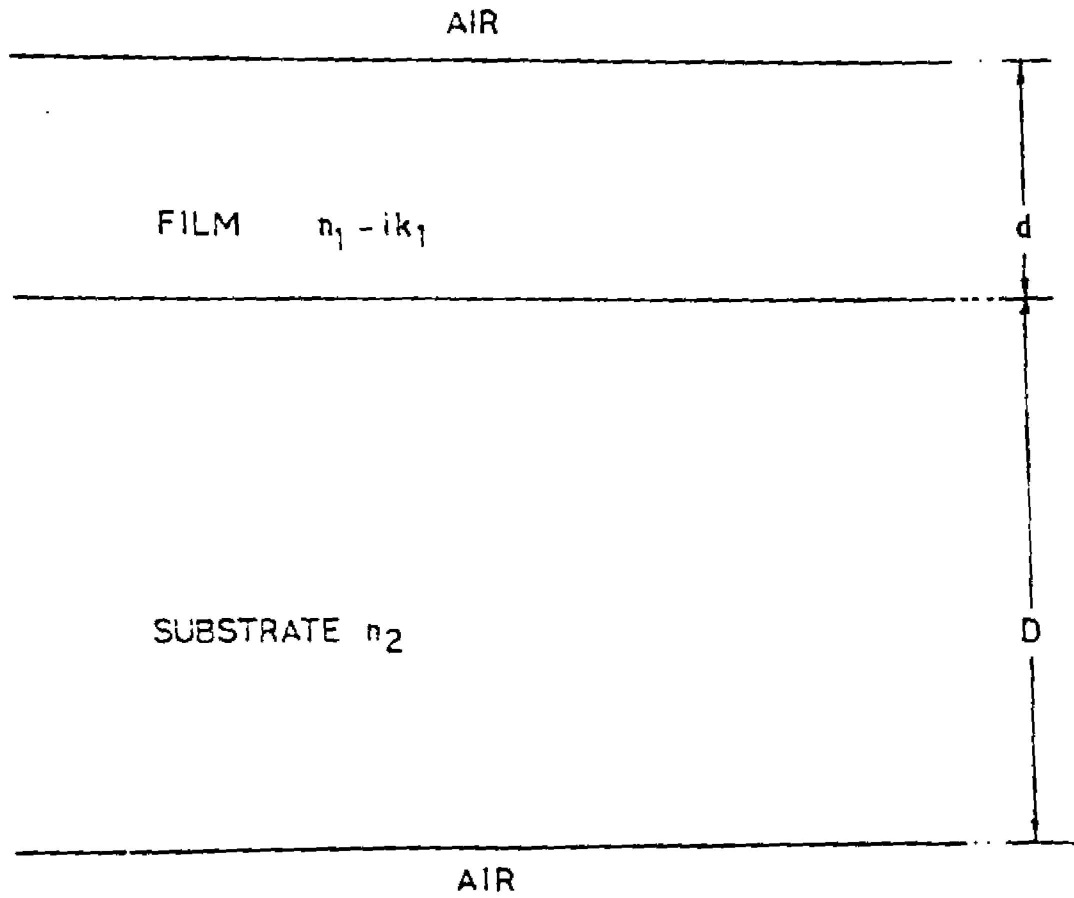

FIG-3.1

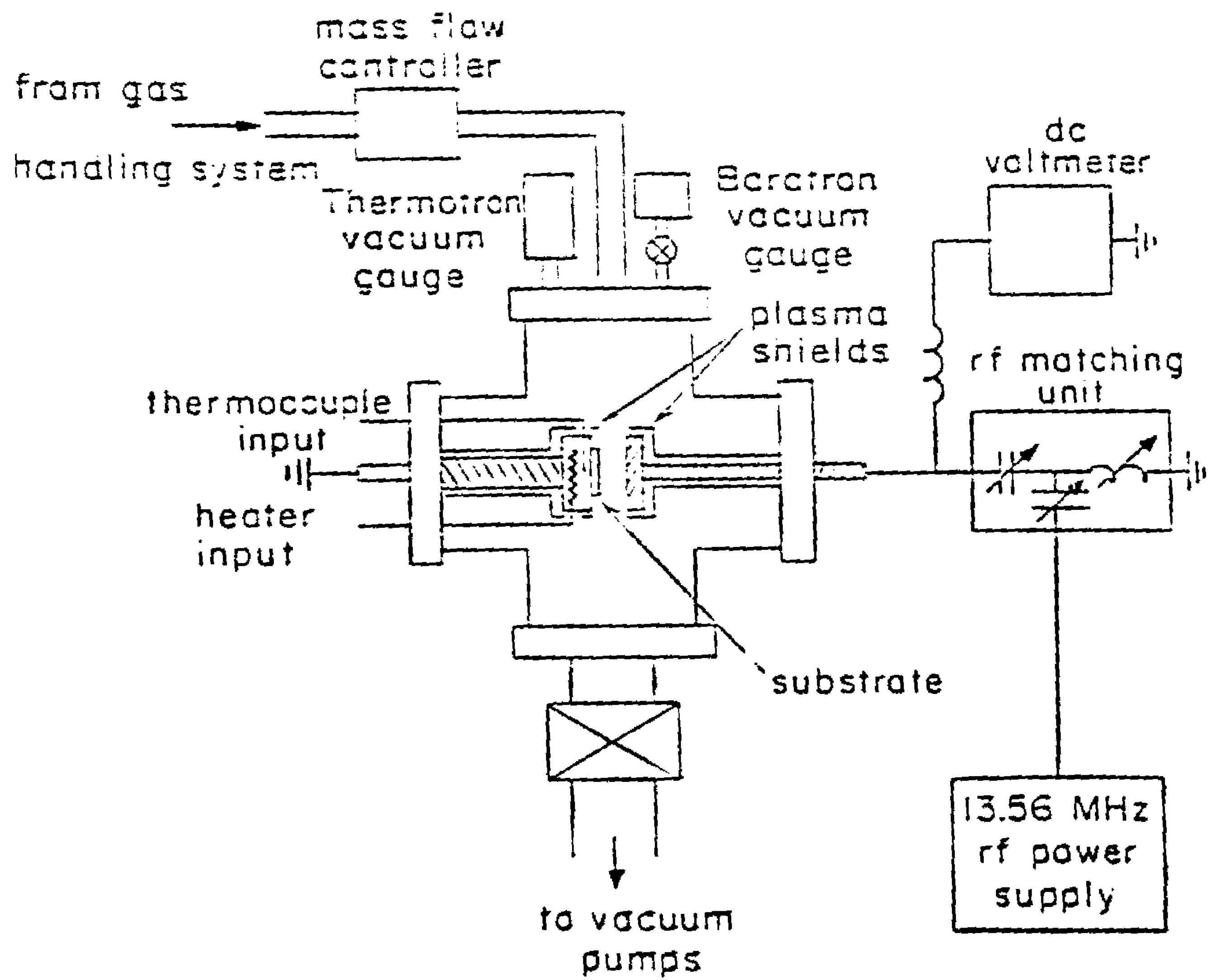

FIG. 4-1

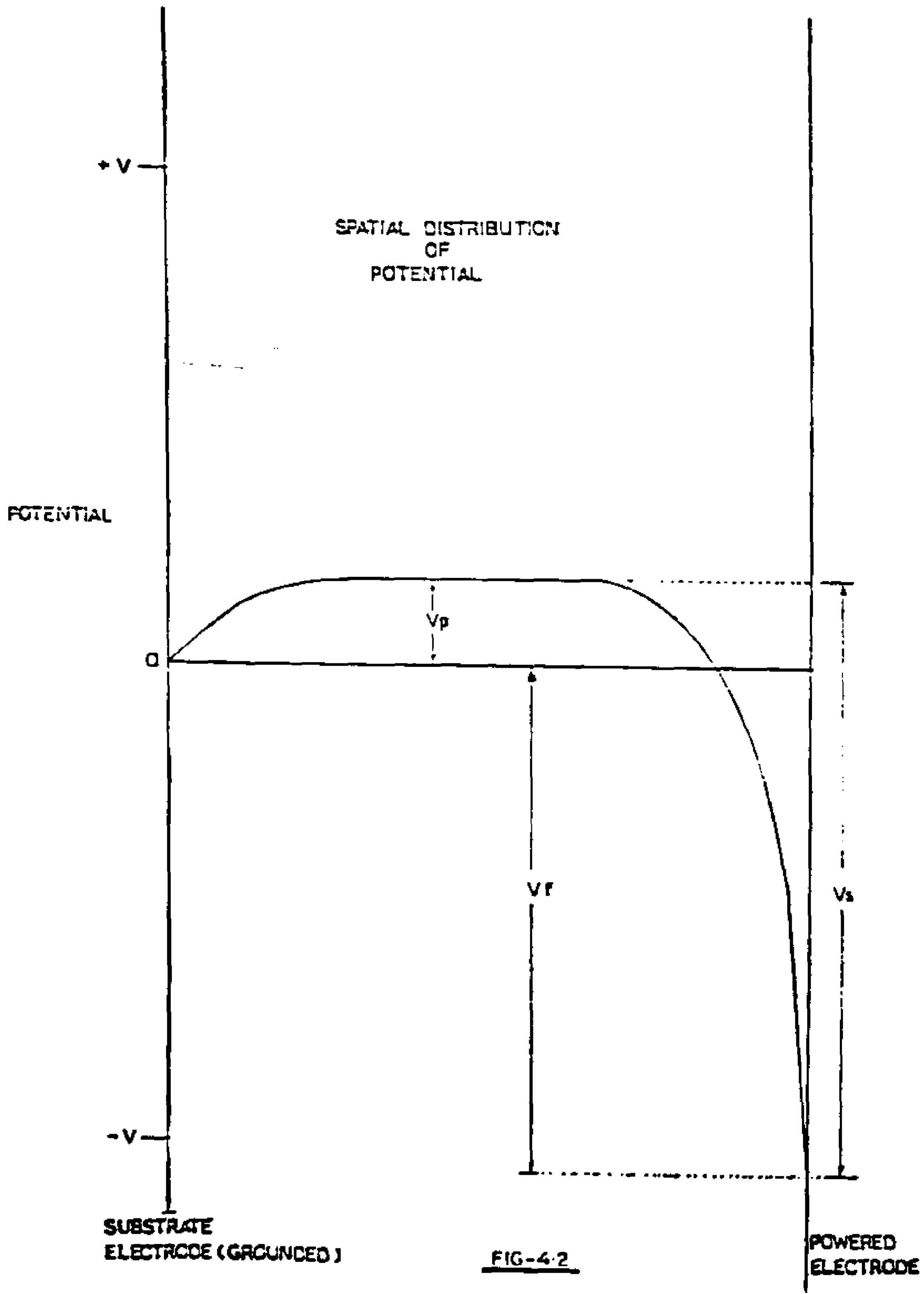

FIG-4.2

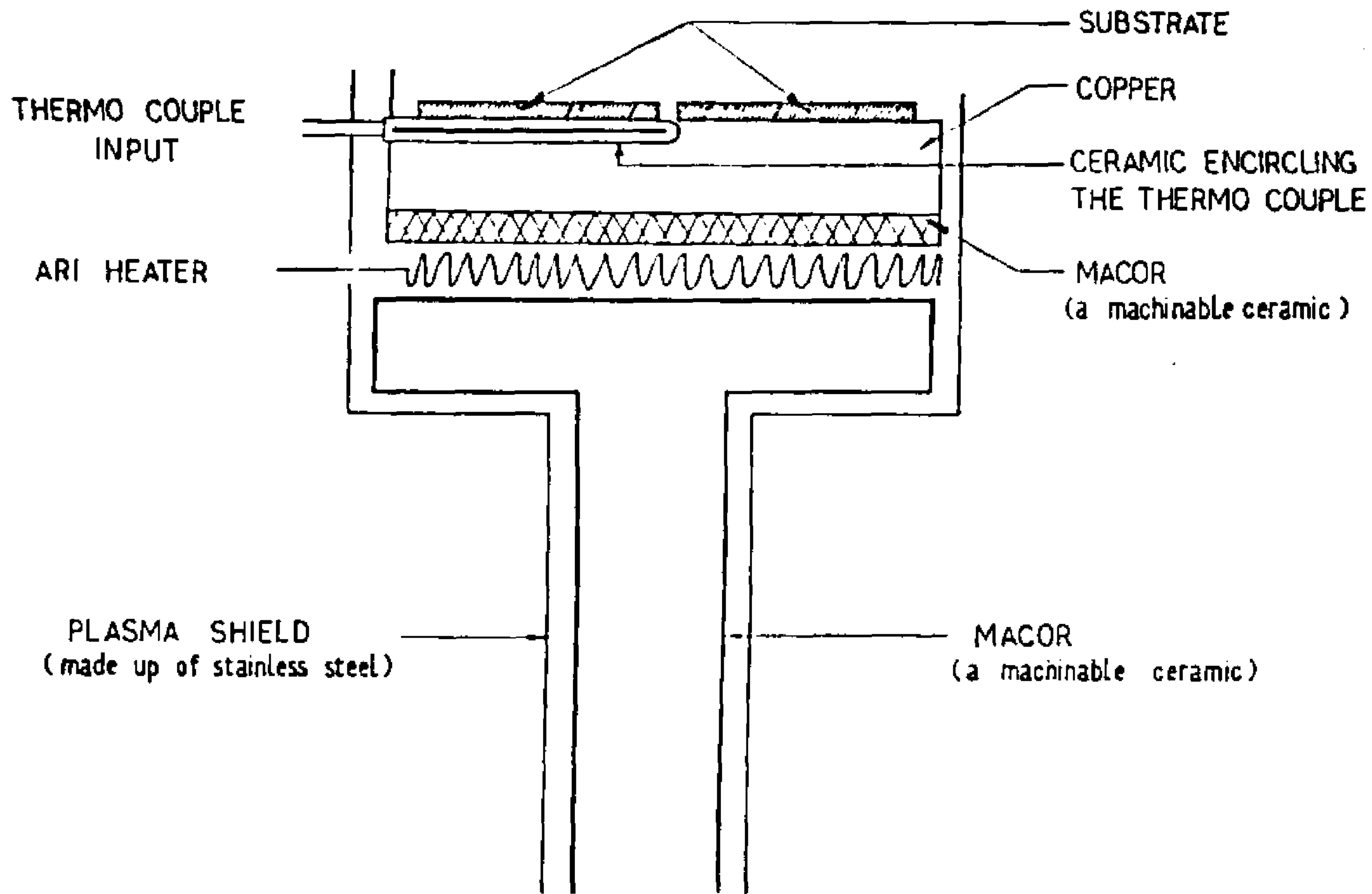

FIG:-4.3

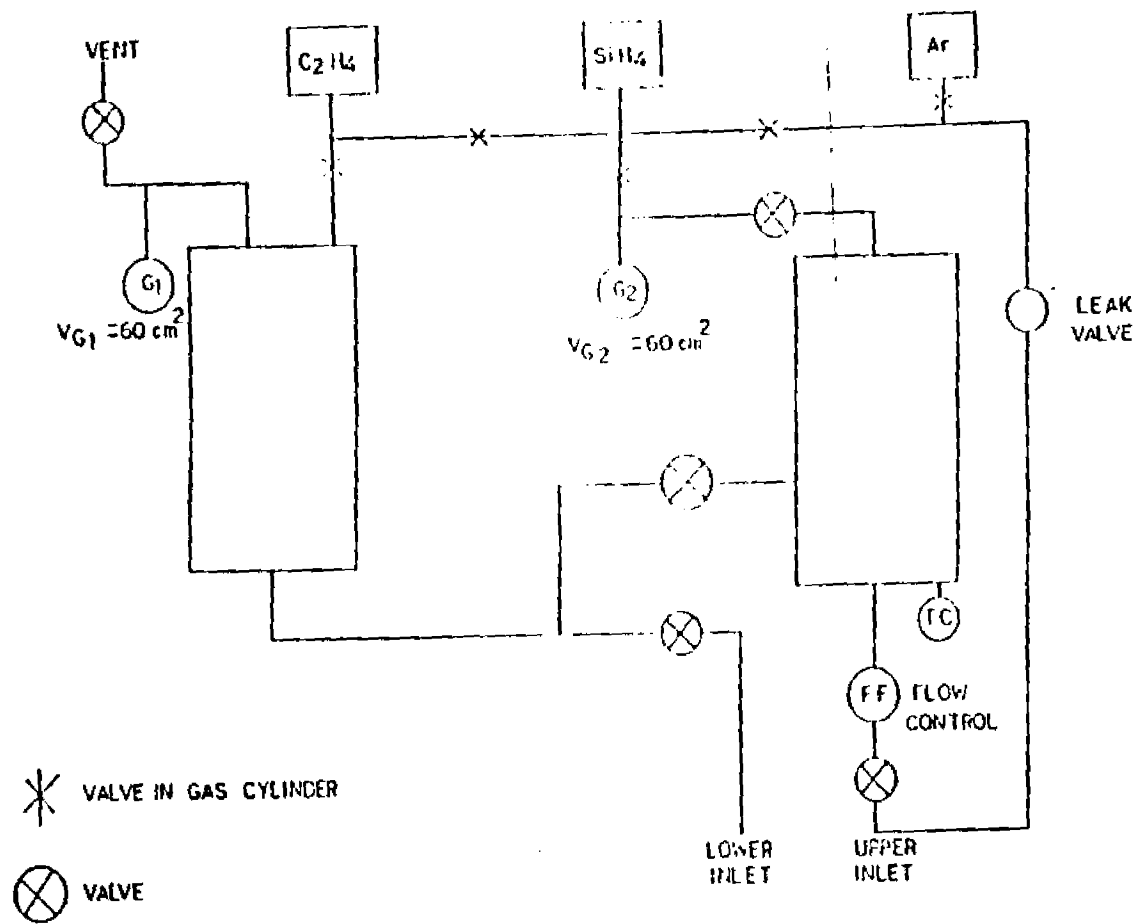

FIG. 4.4.

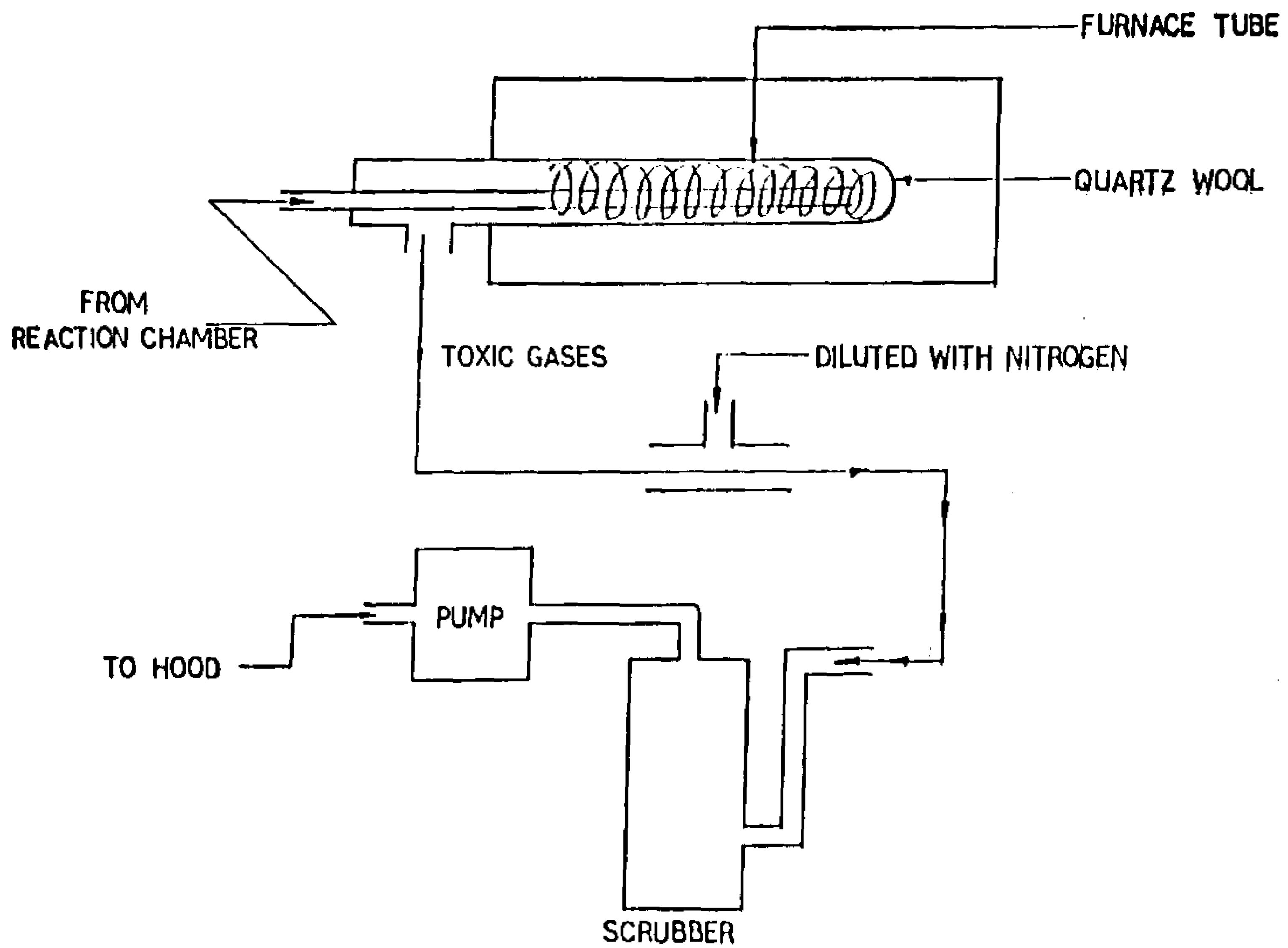

FIG:- 4.5

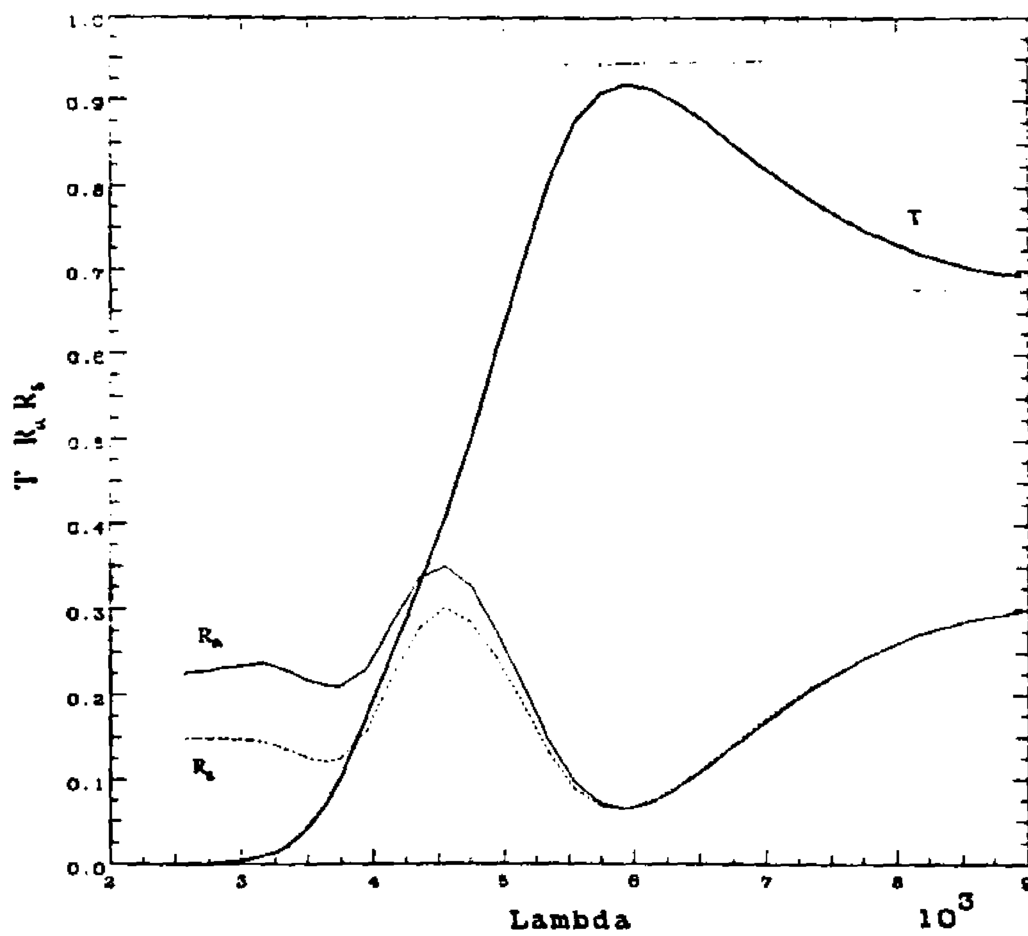

Fig. 4.6

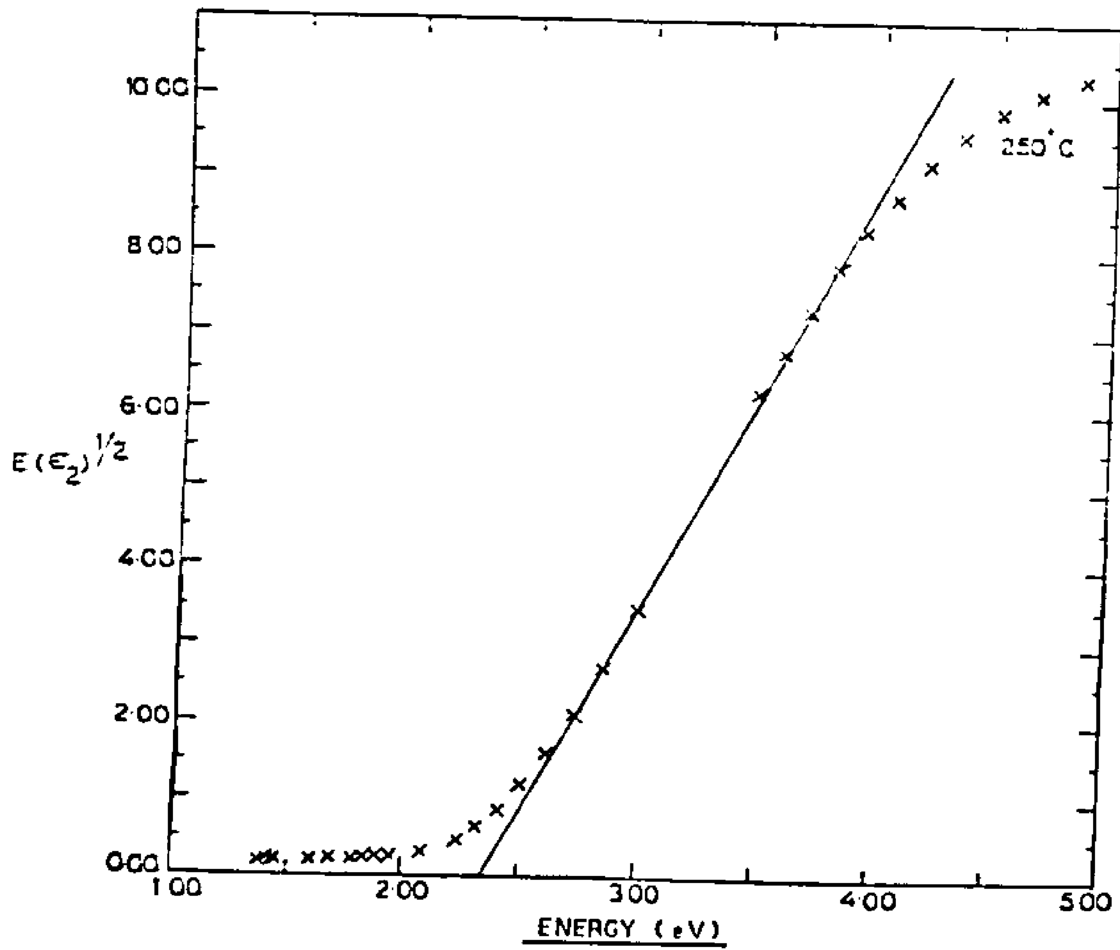

FIG. 4·7

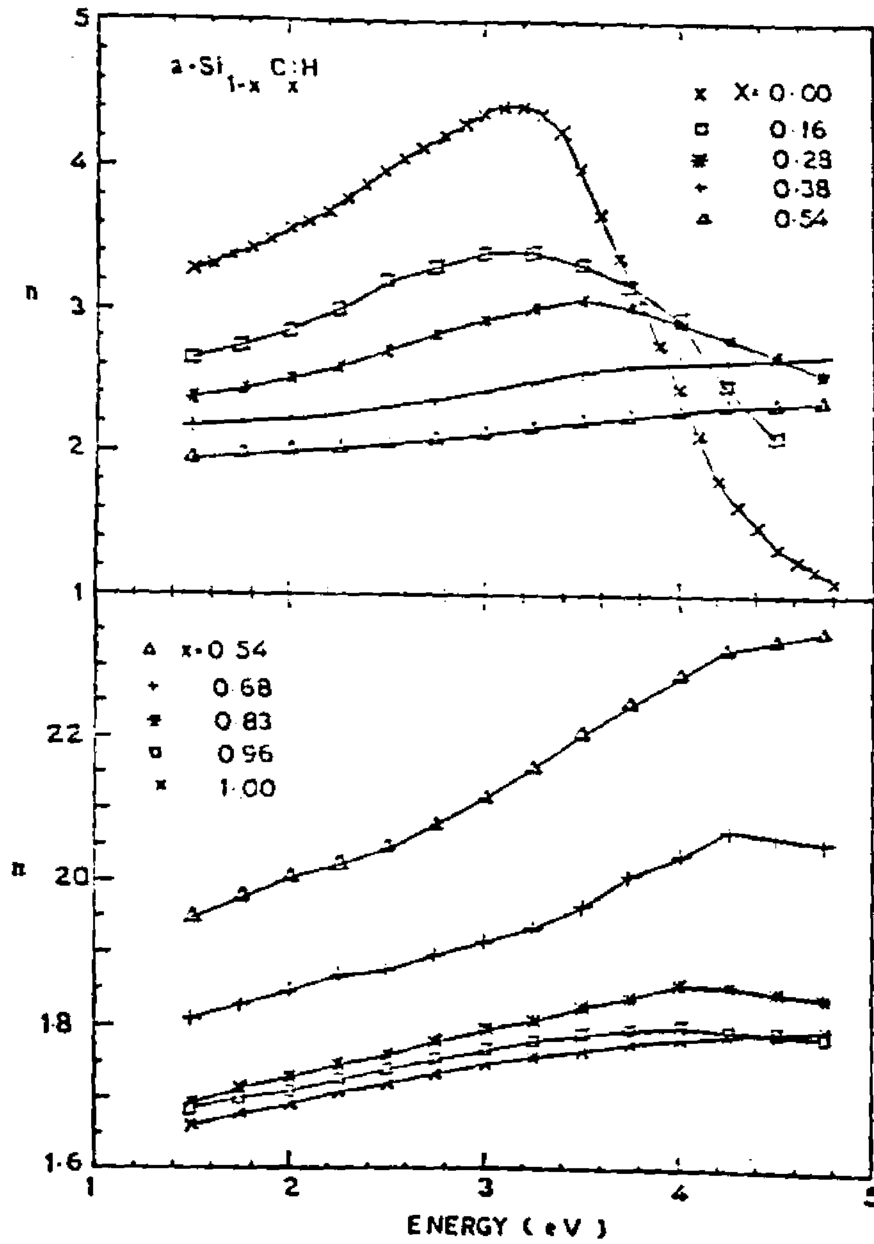

FIG 5.1

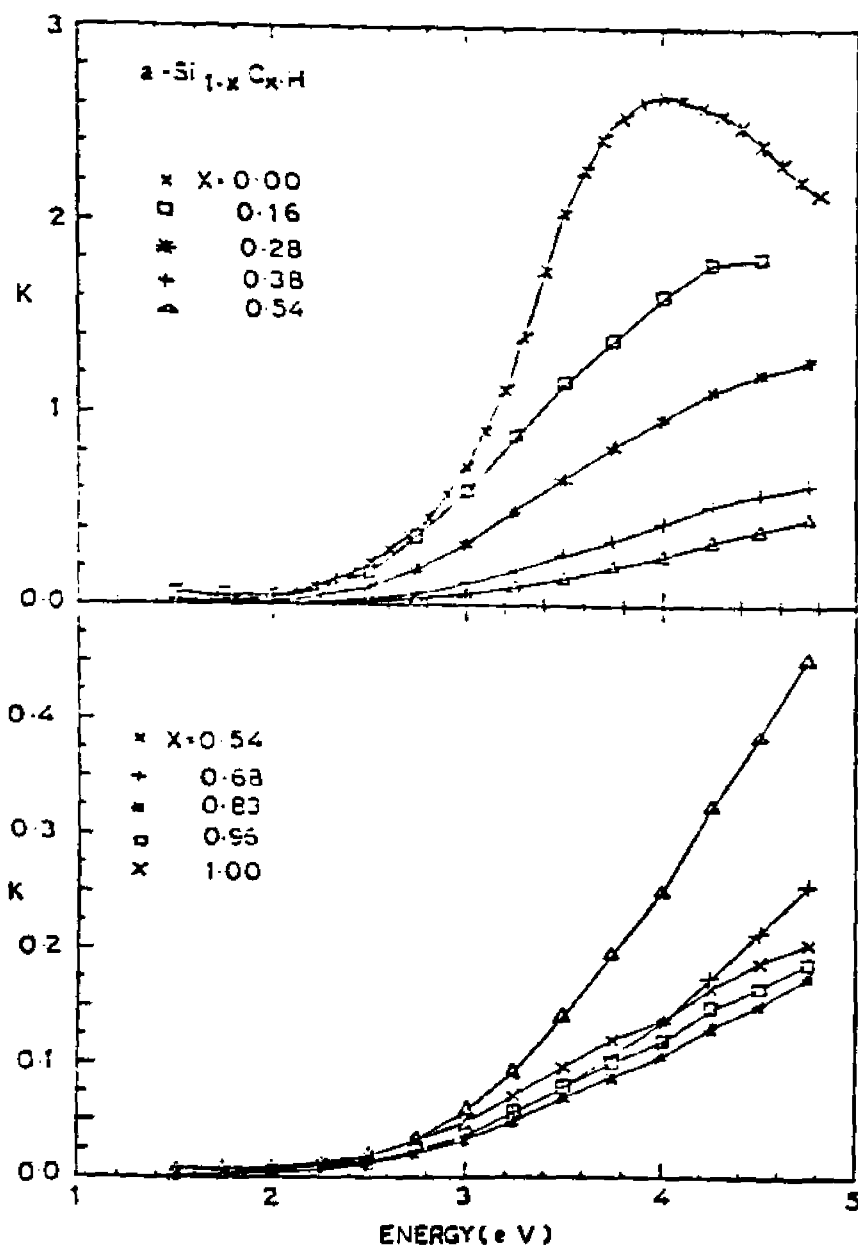

FIG 5.2

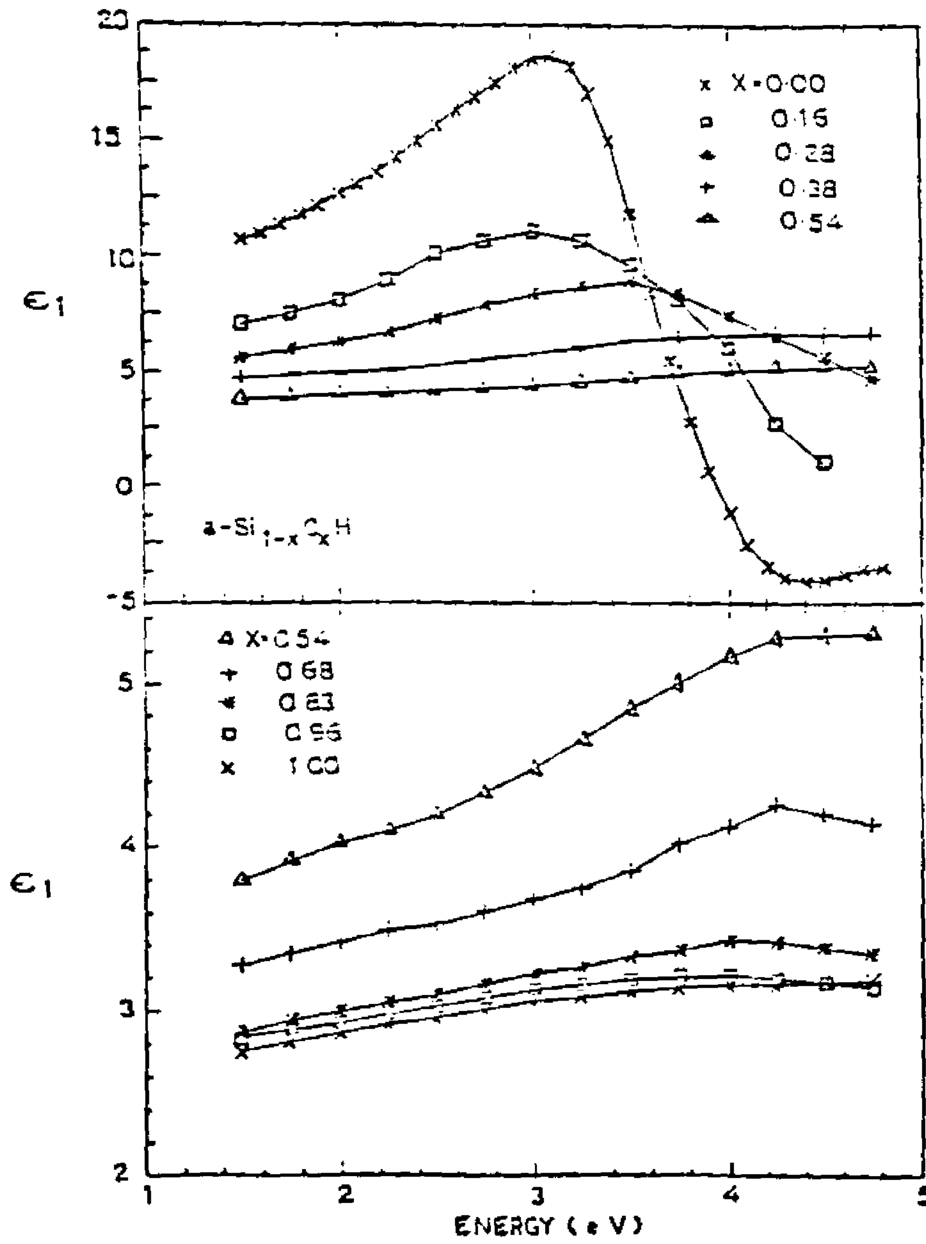

FIG 5.3

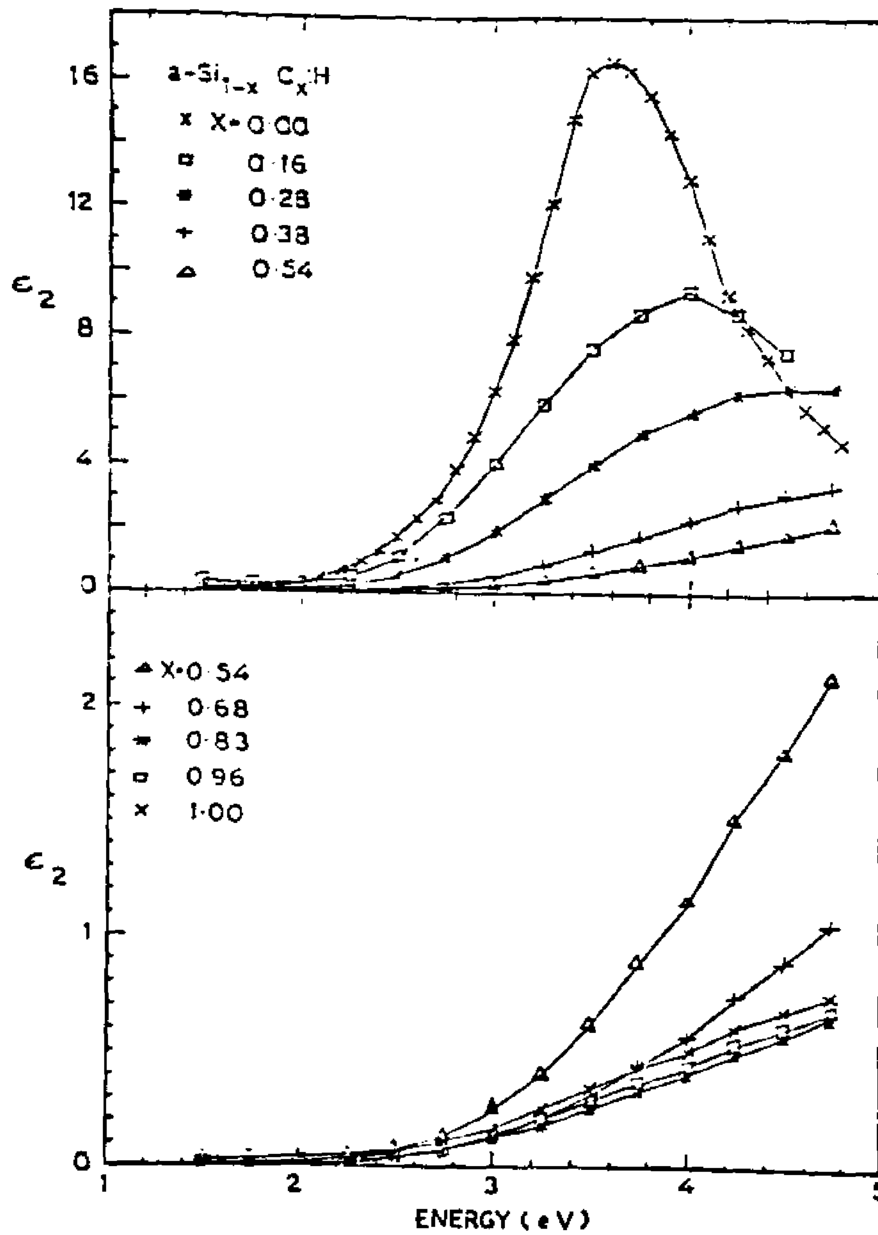

FIG 5.4

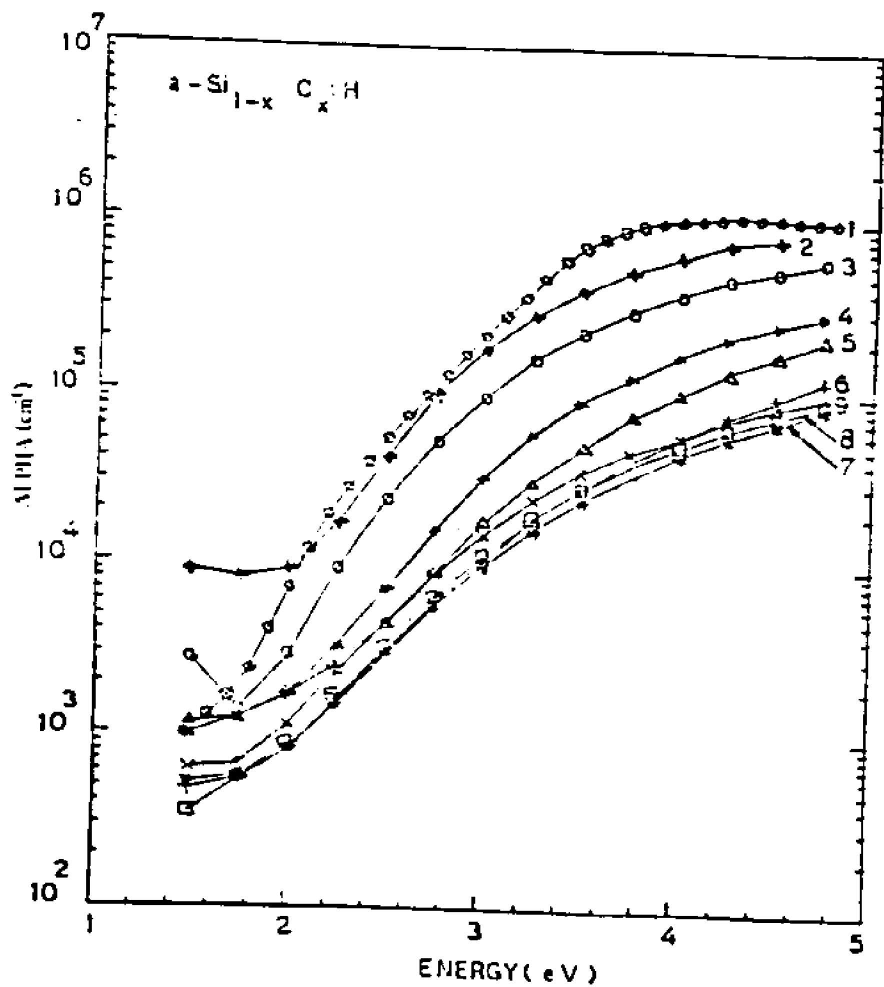

FIG. 5.5

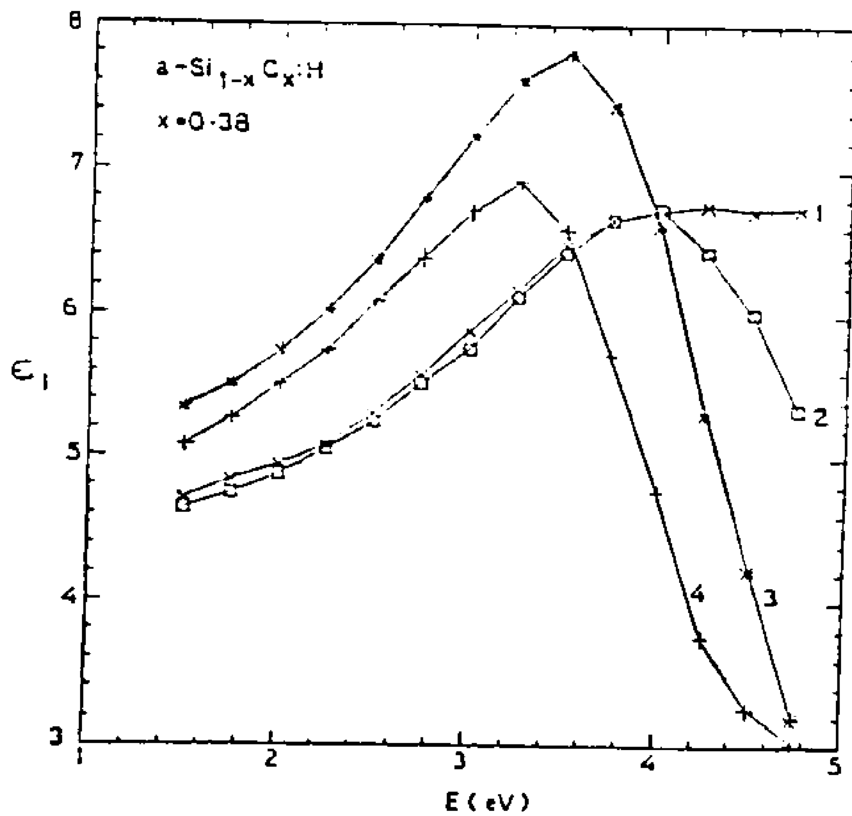

FIG 5.6

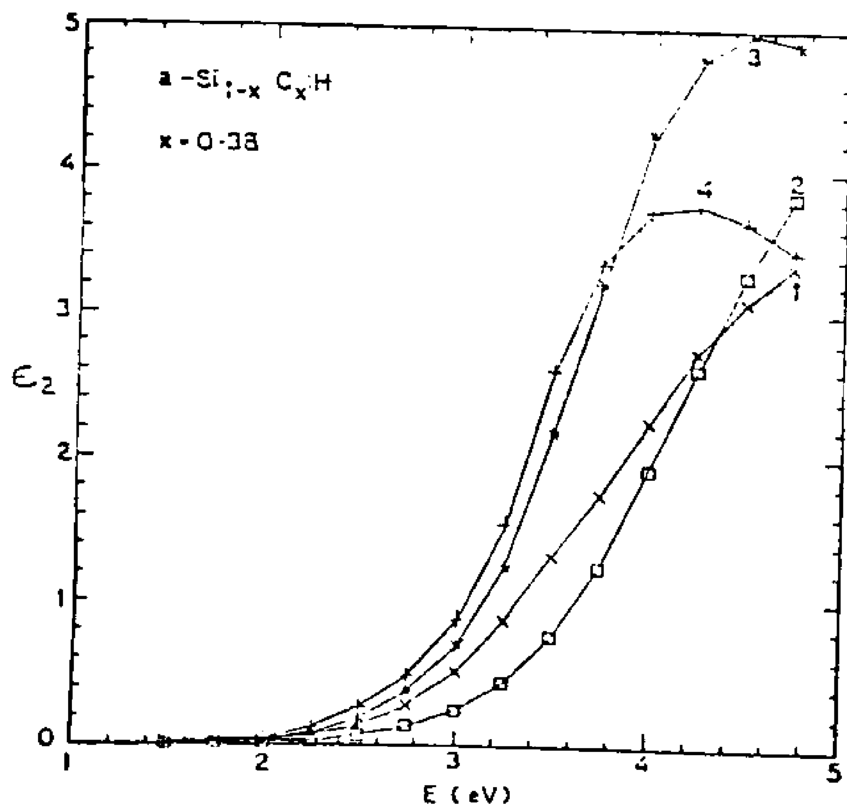

FIG 5.7

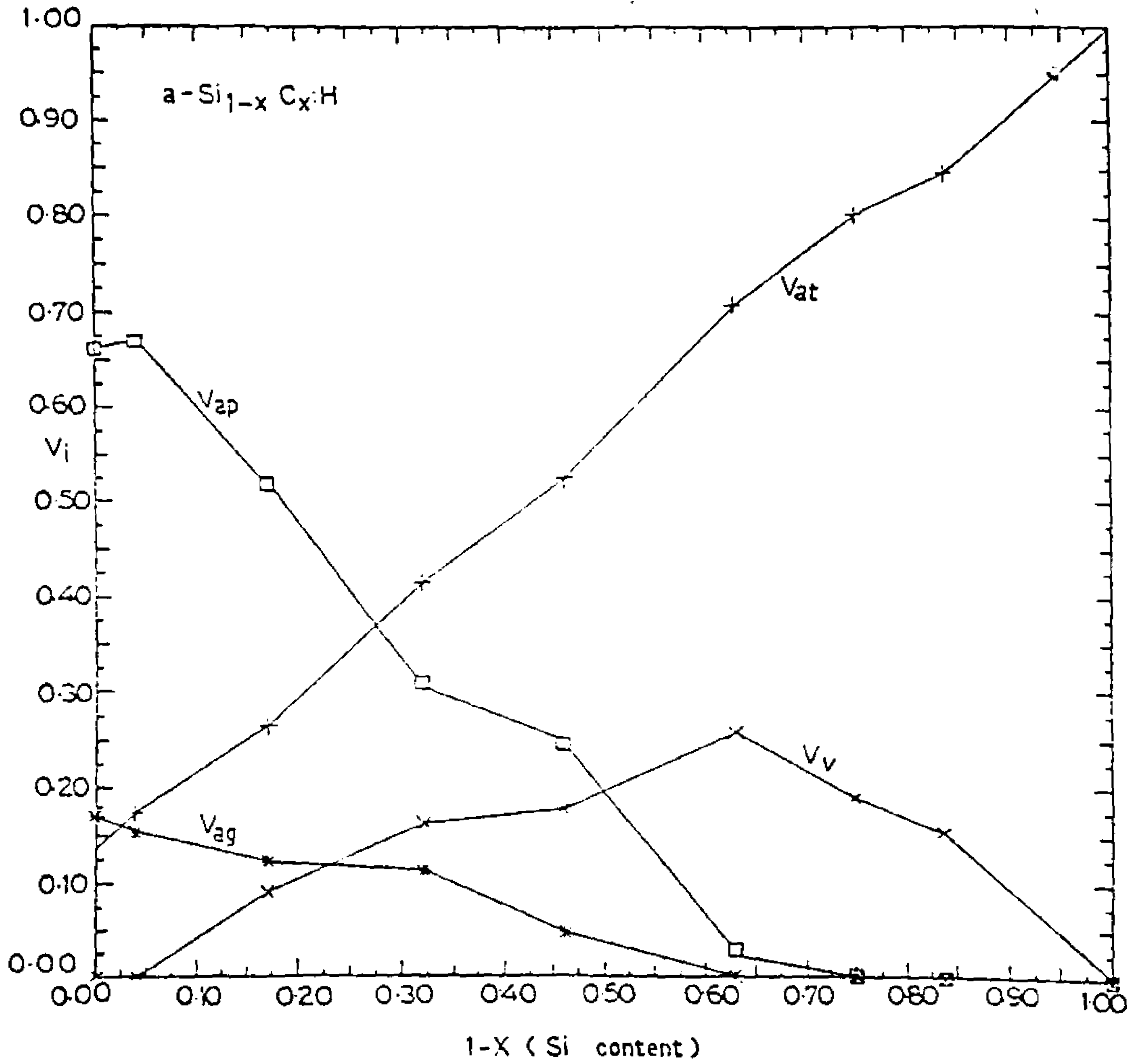

FIG. 5.8

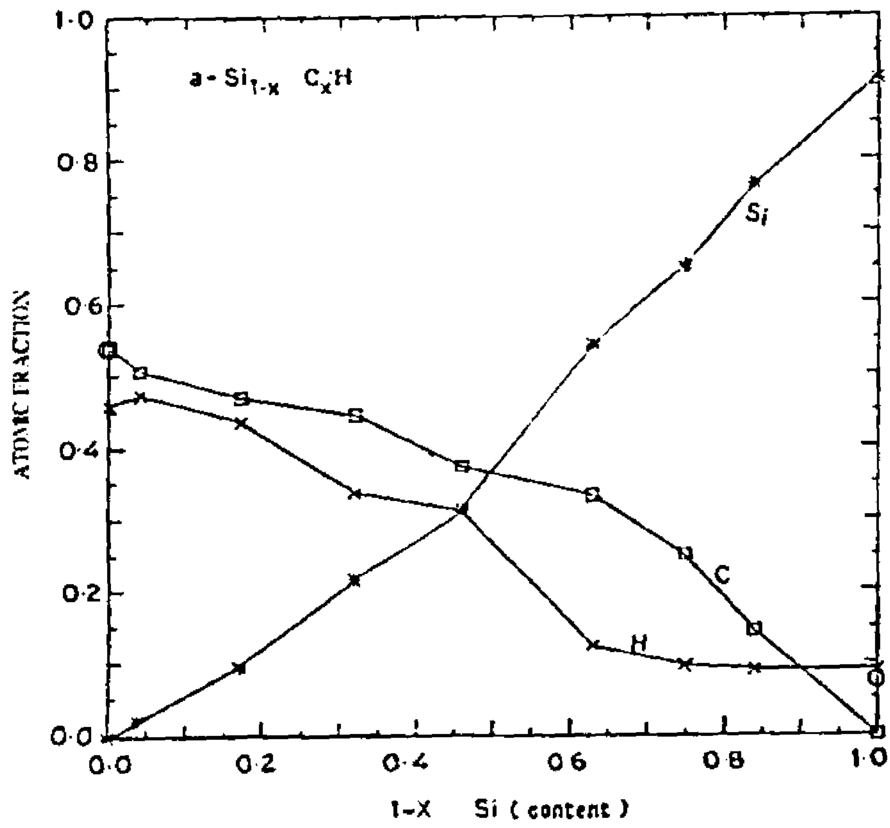

FIG. 59

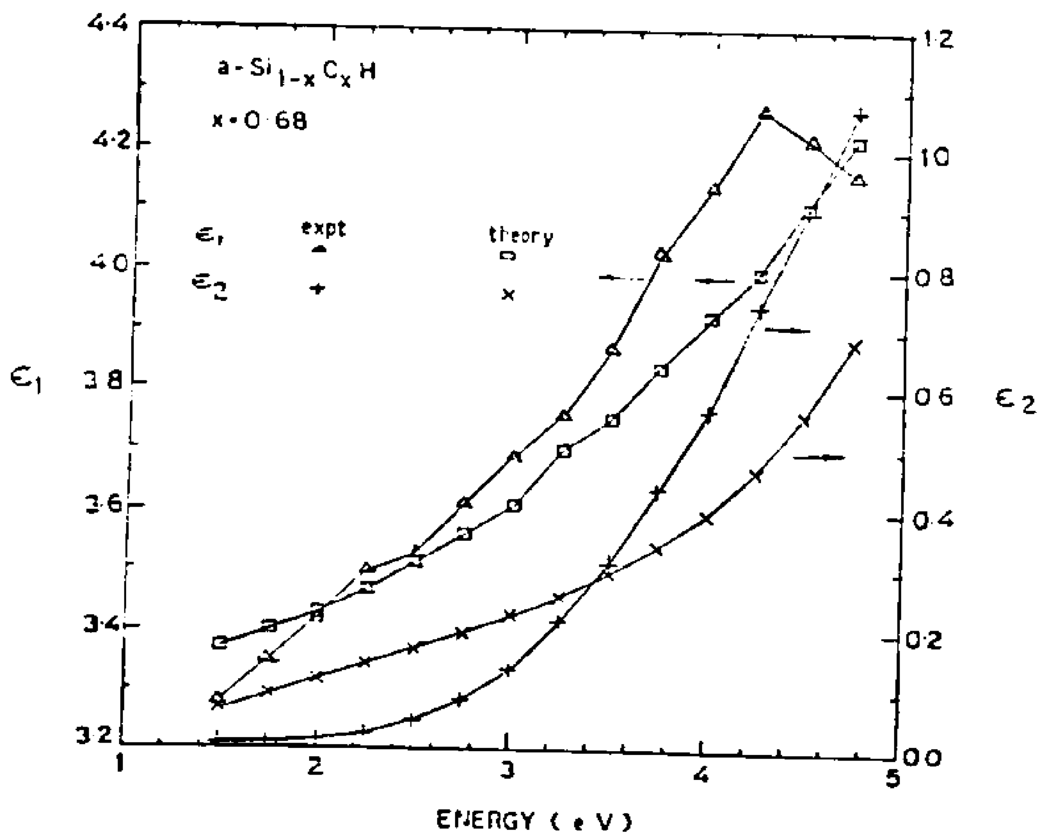

FIG 5.10

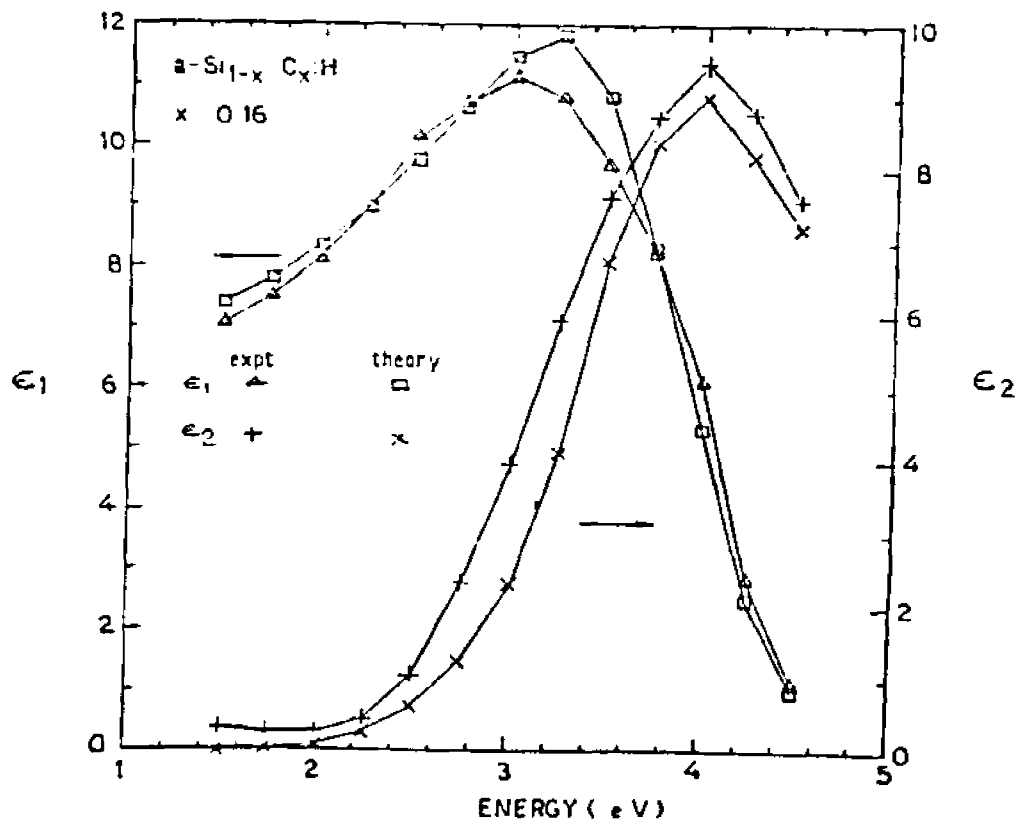

FIG 5.11

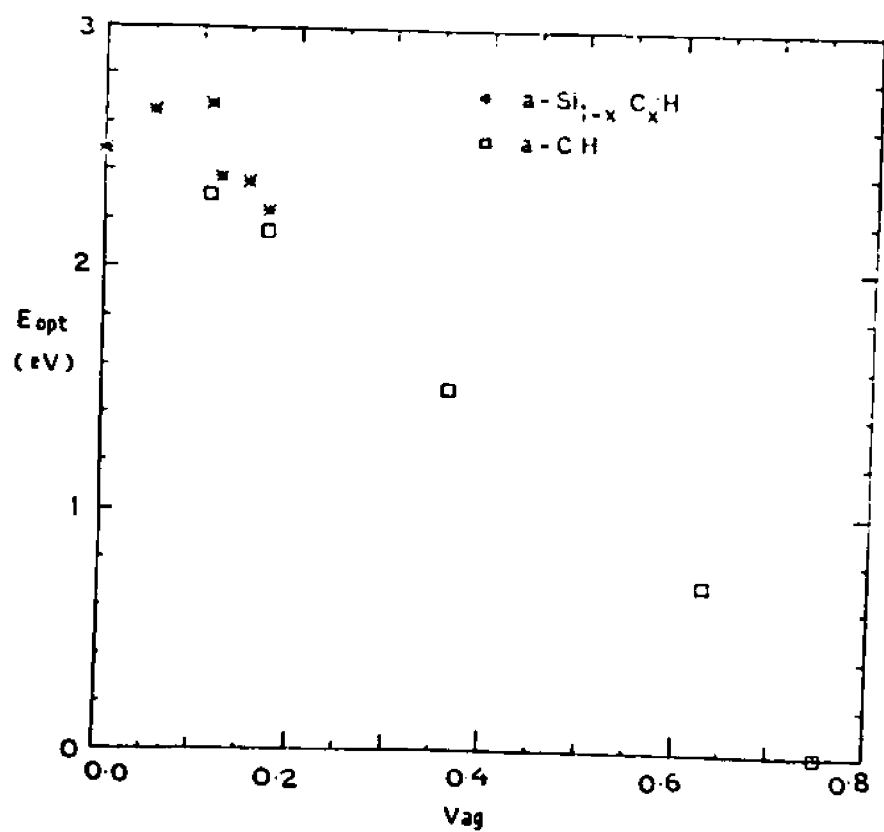

FIG 5 12

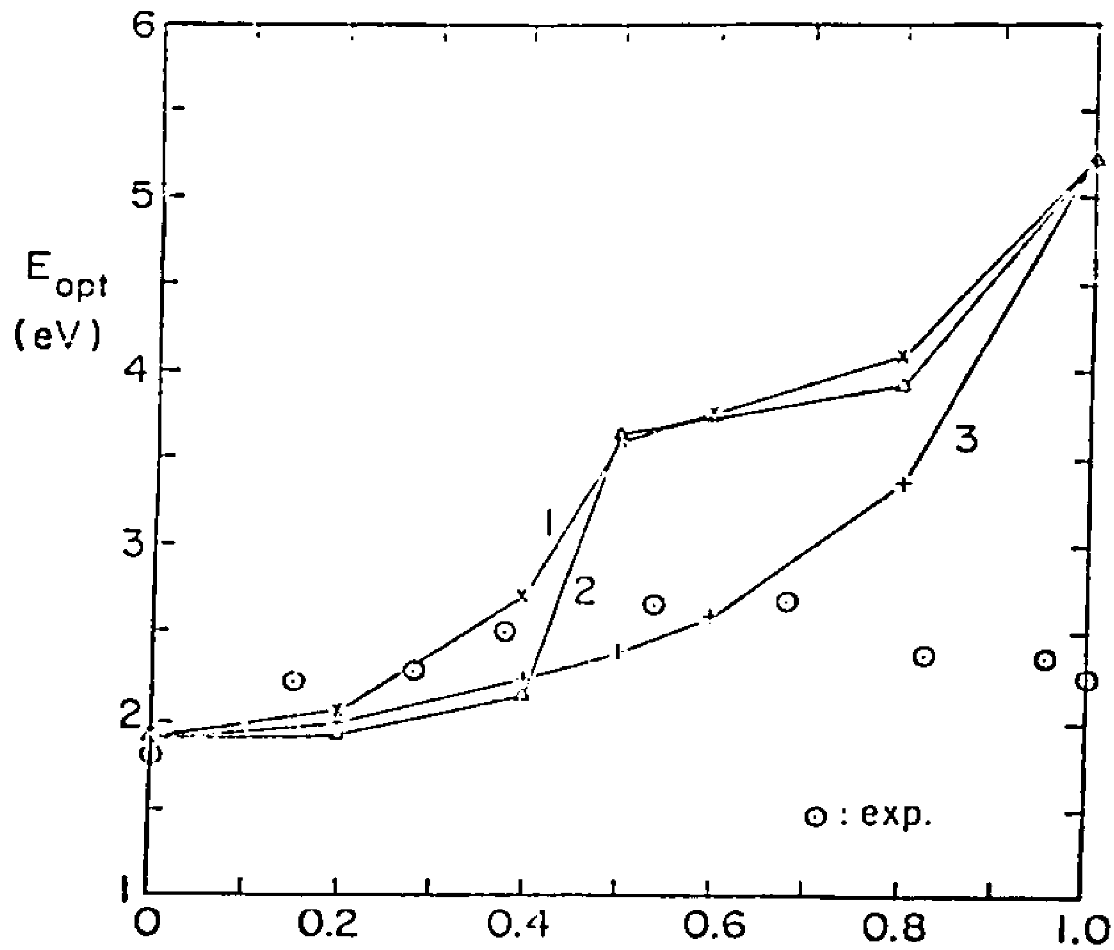

FIG 5.13

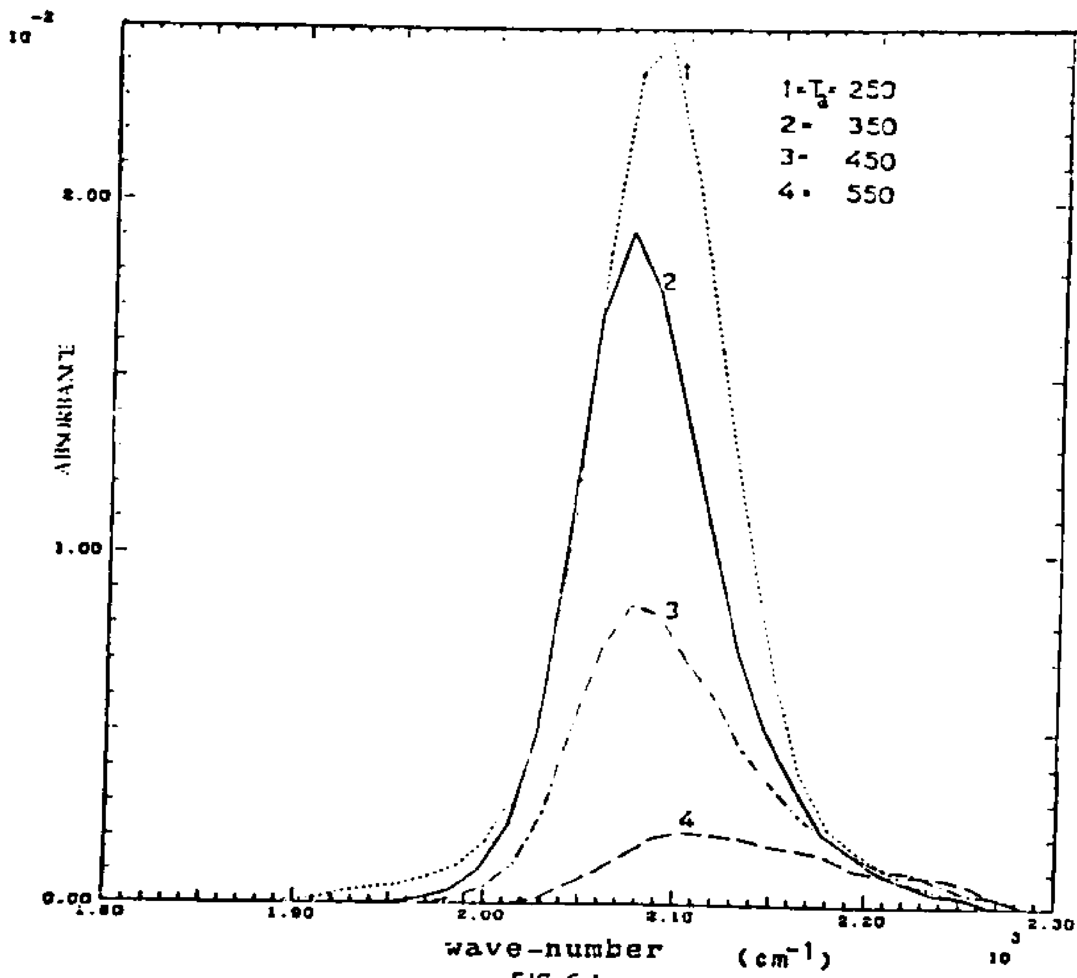

FIG. 6-1

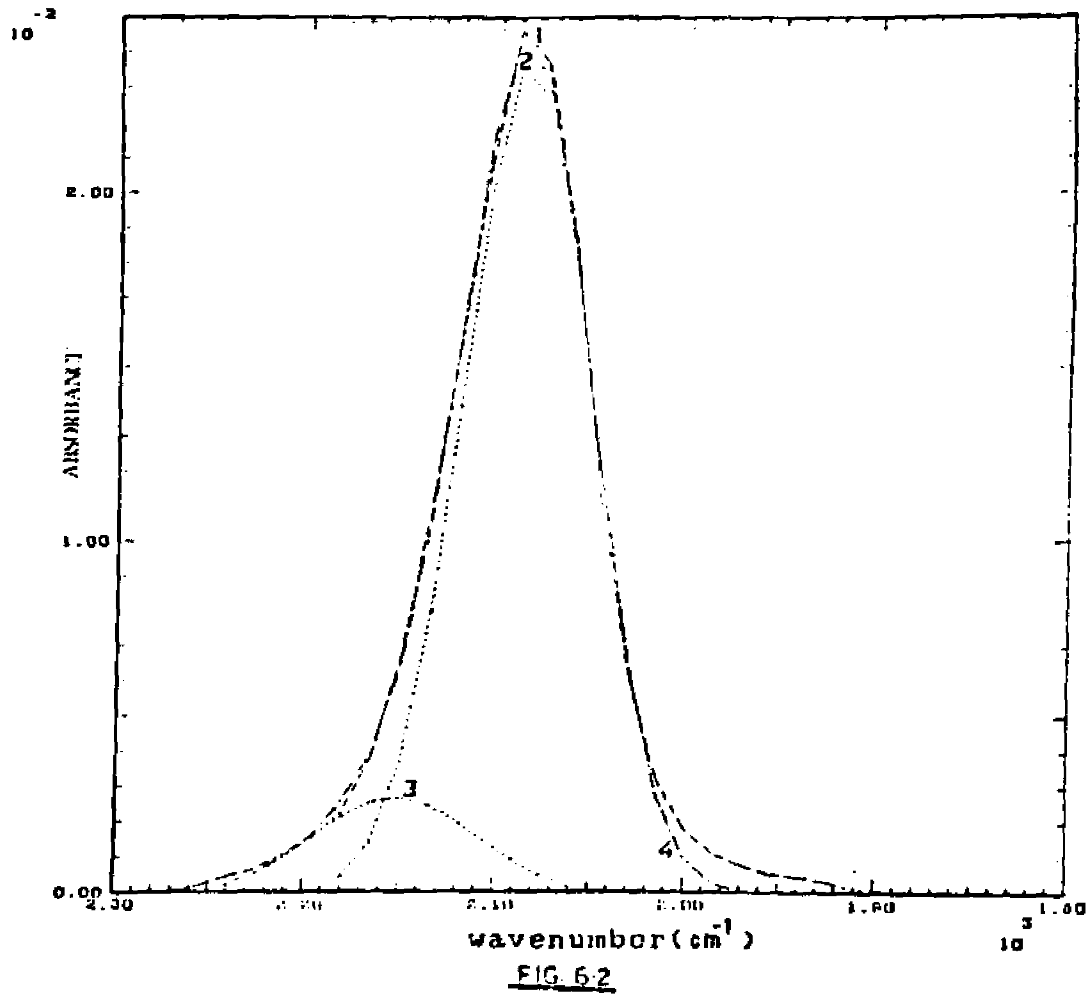

FIG. 6.2

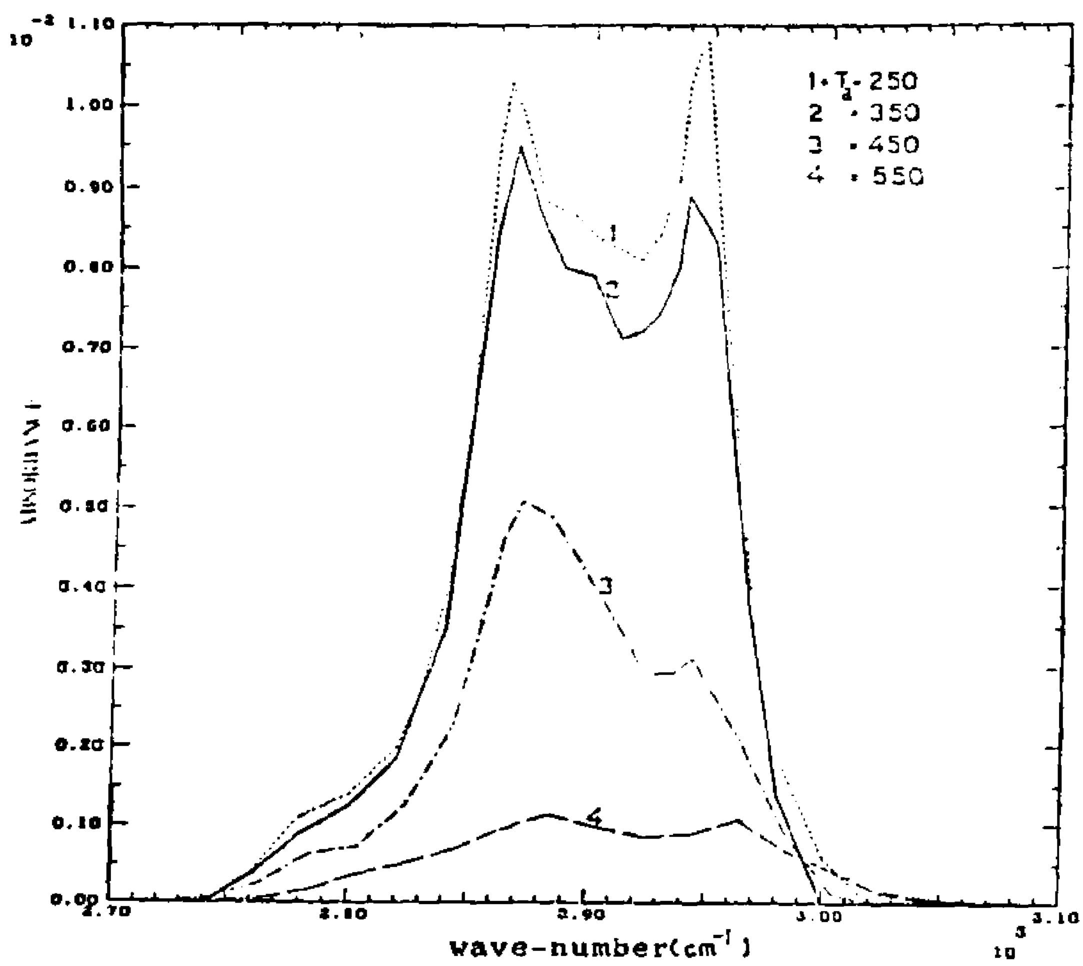

FIG 6.3

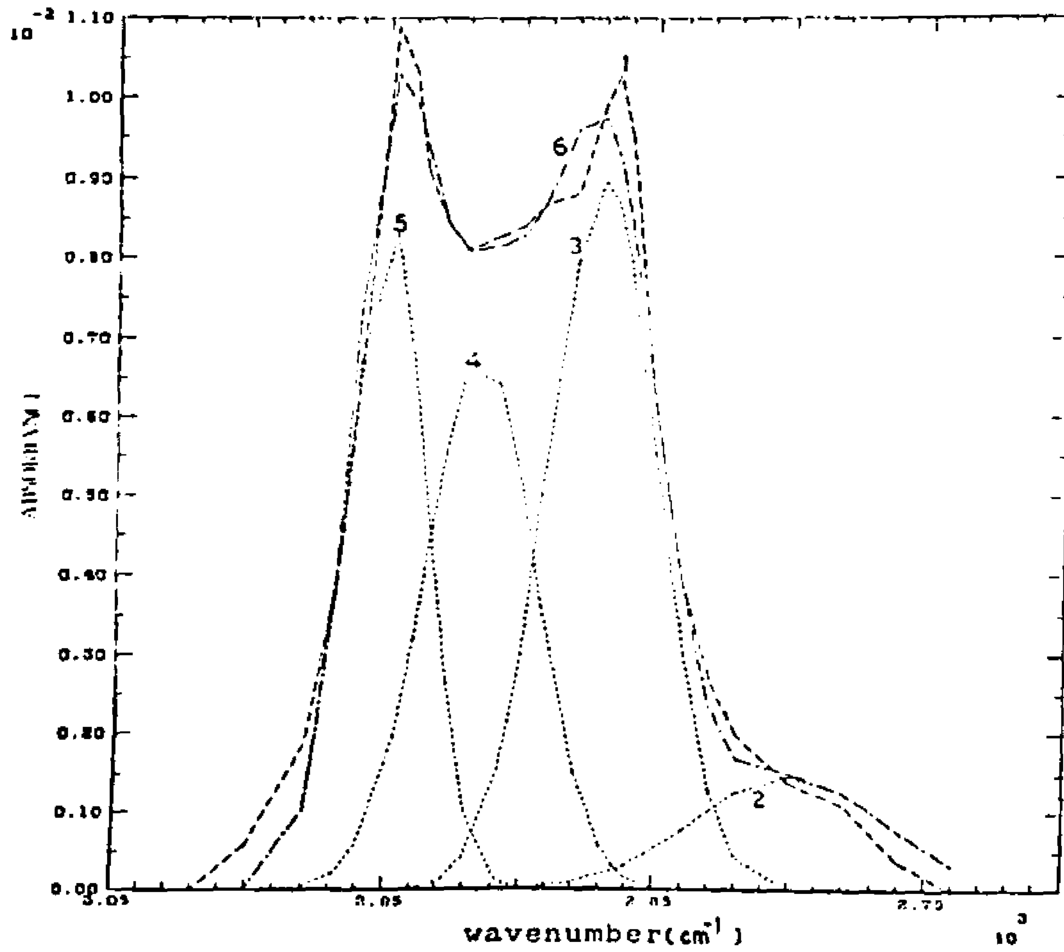

FIG 6.4

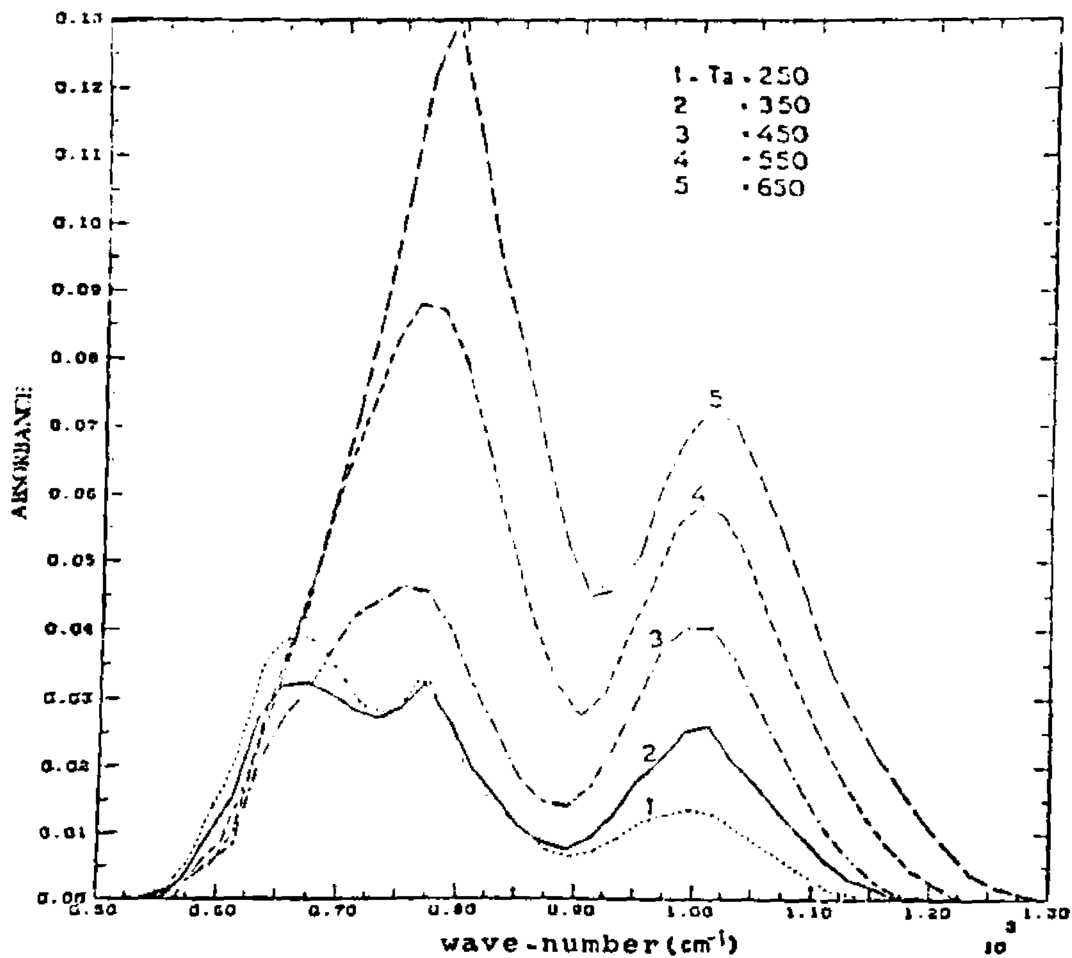

FIG65 a

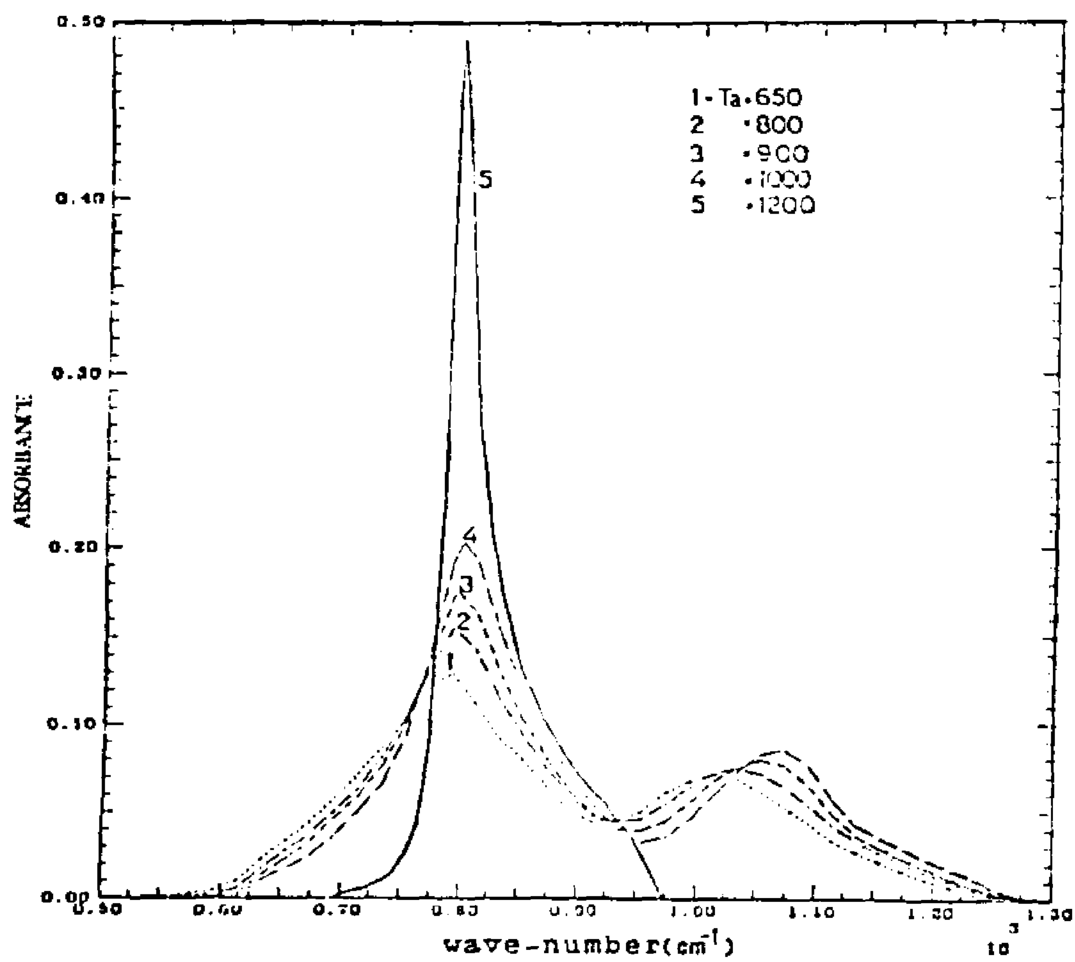

FIG 6.5 b

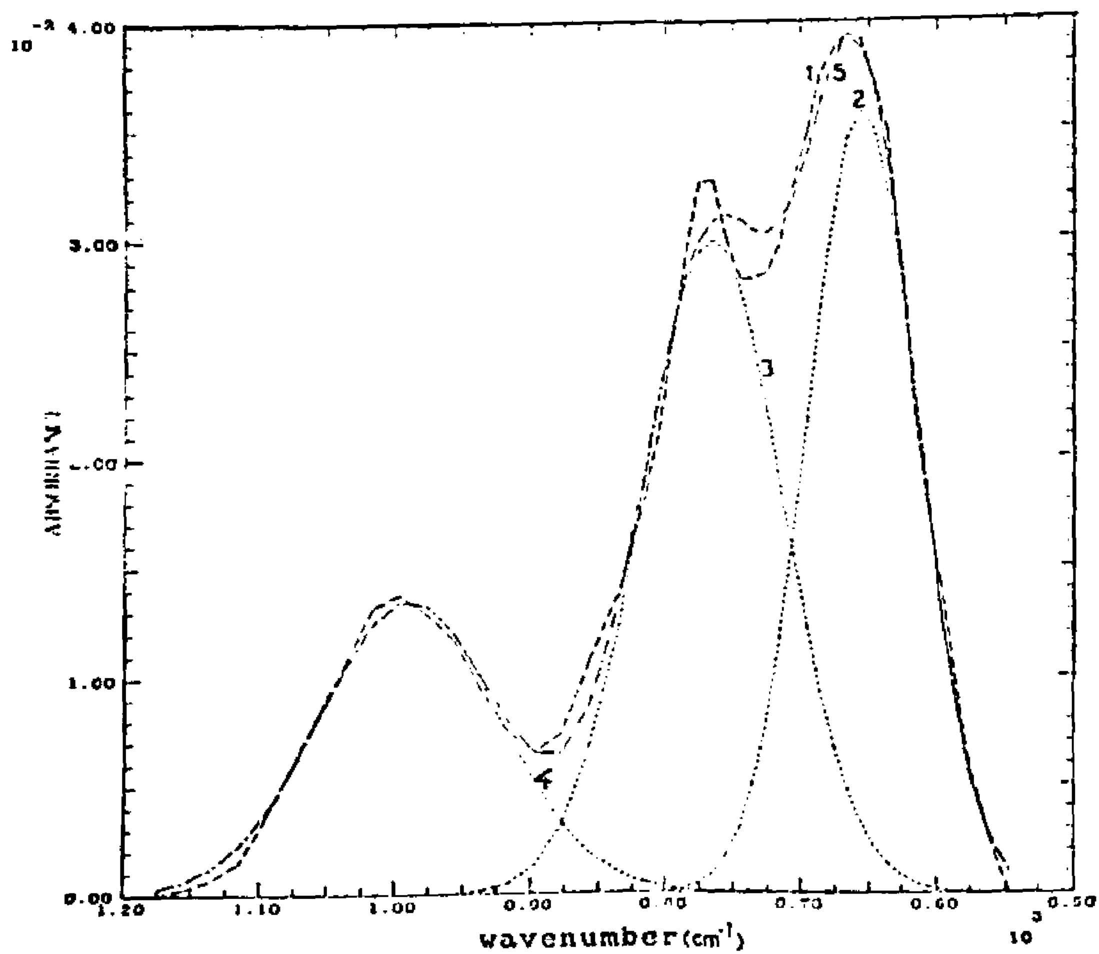

FIG. 6.5a

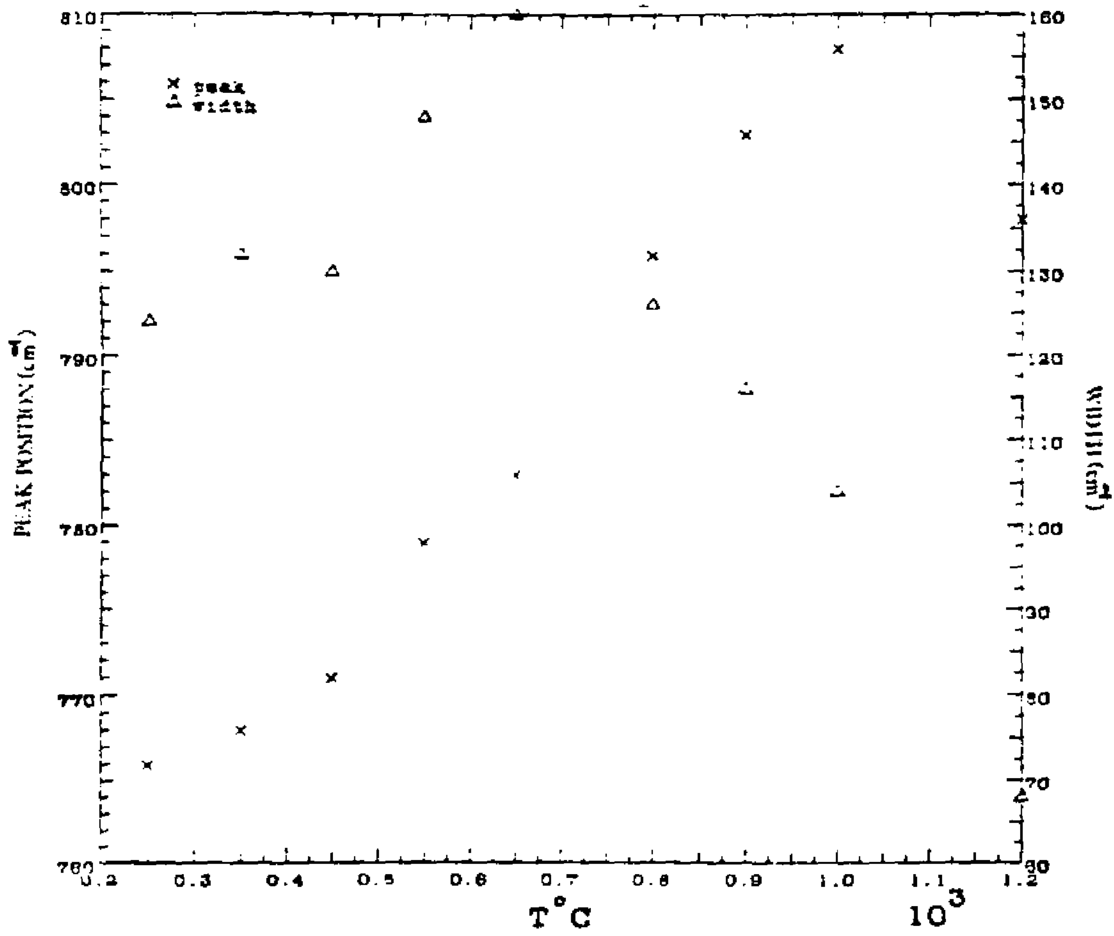

Fig. 6.6b

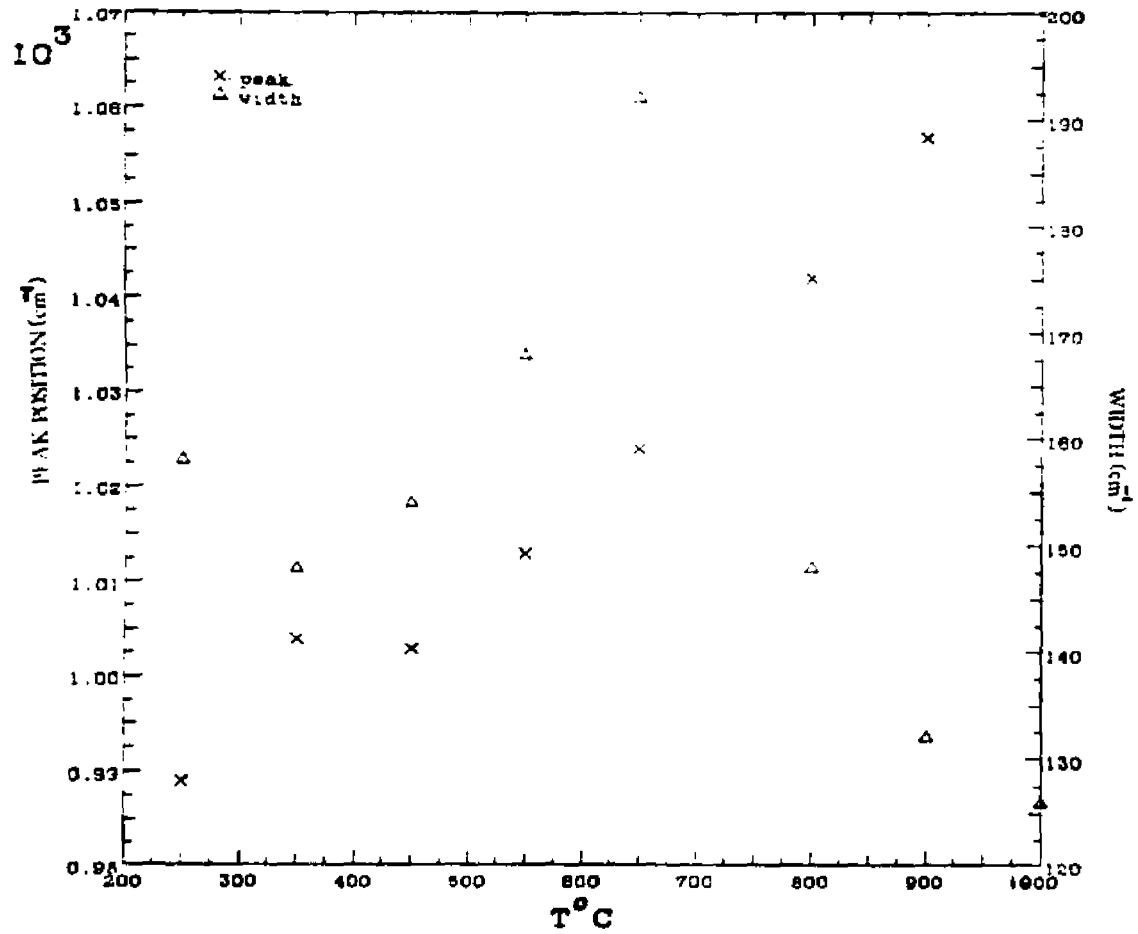

Fig. 6.6c

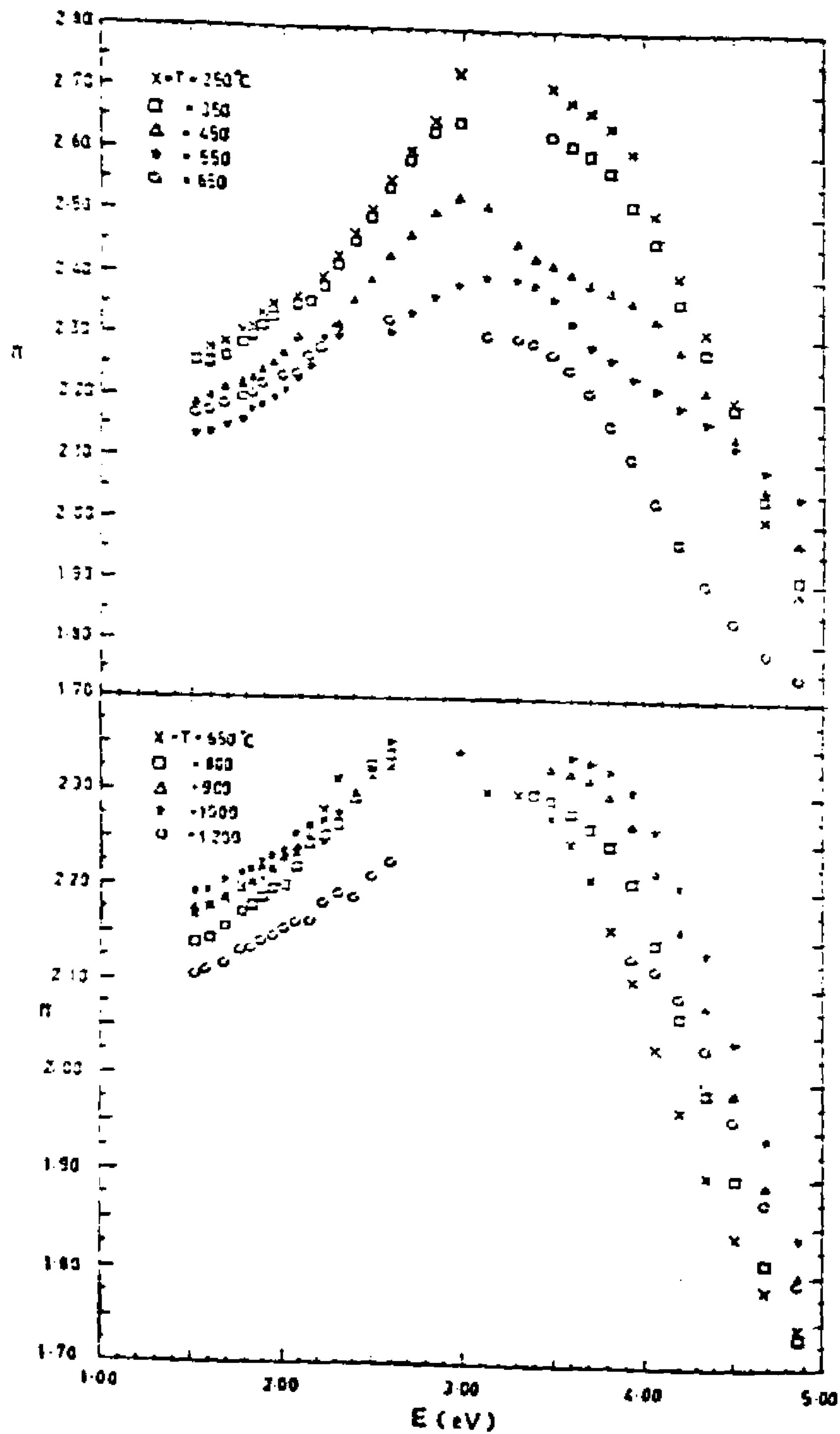

FIG.6·7

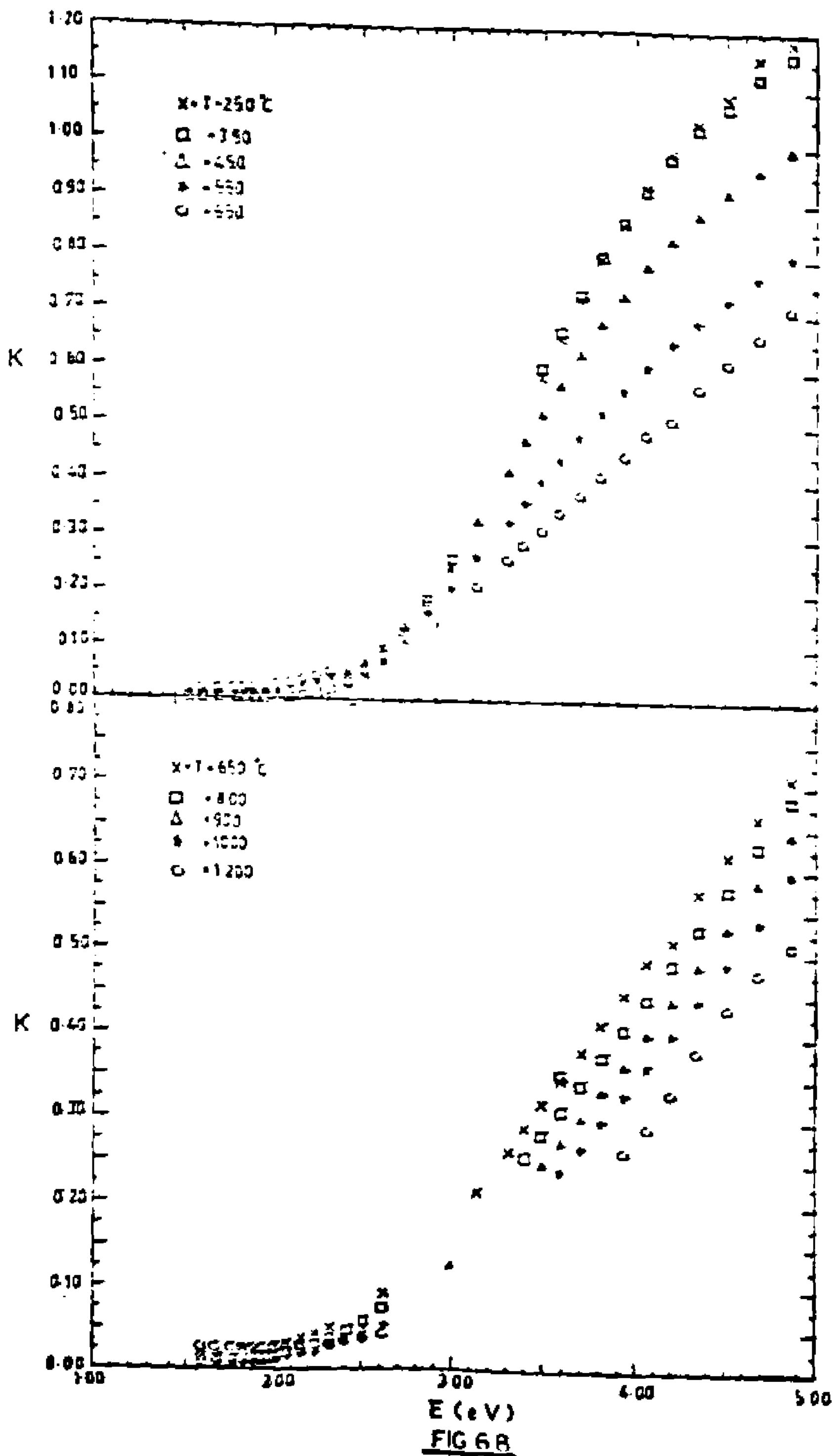

FIG 6 B

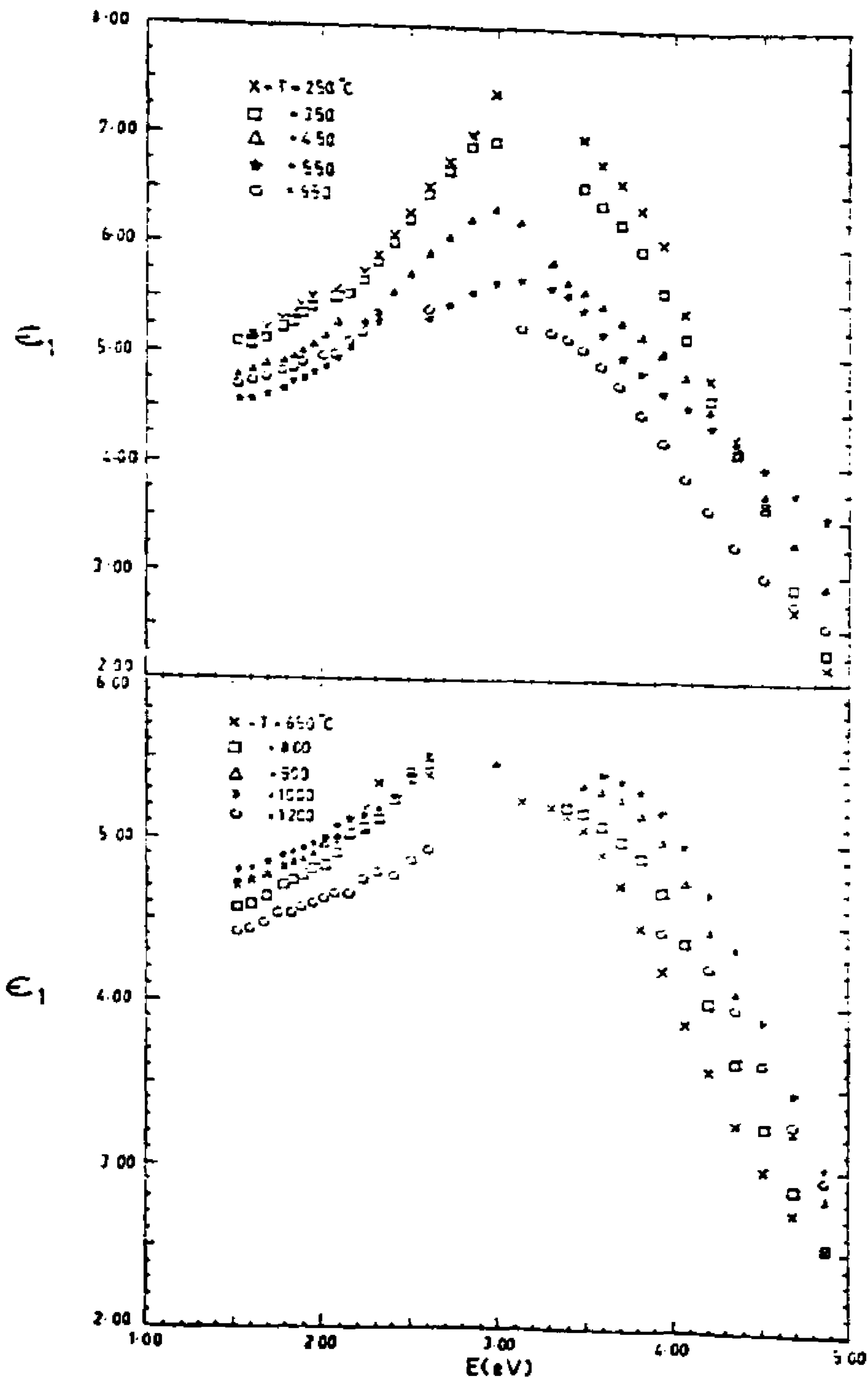

FIG 6.9

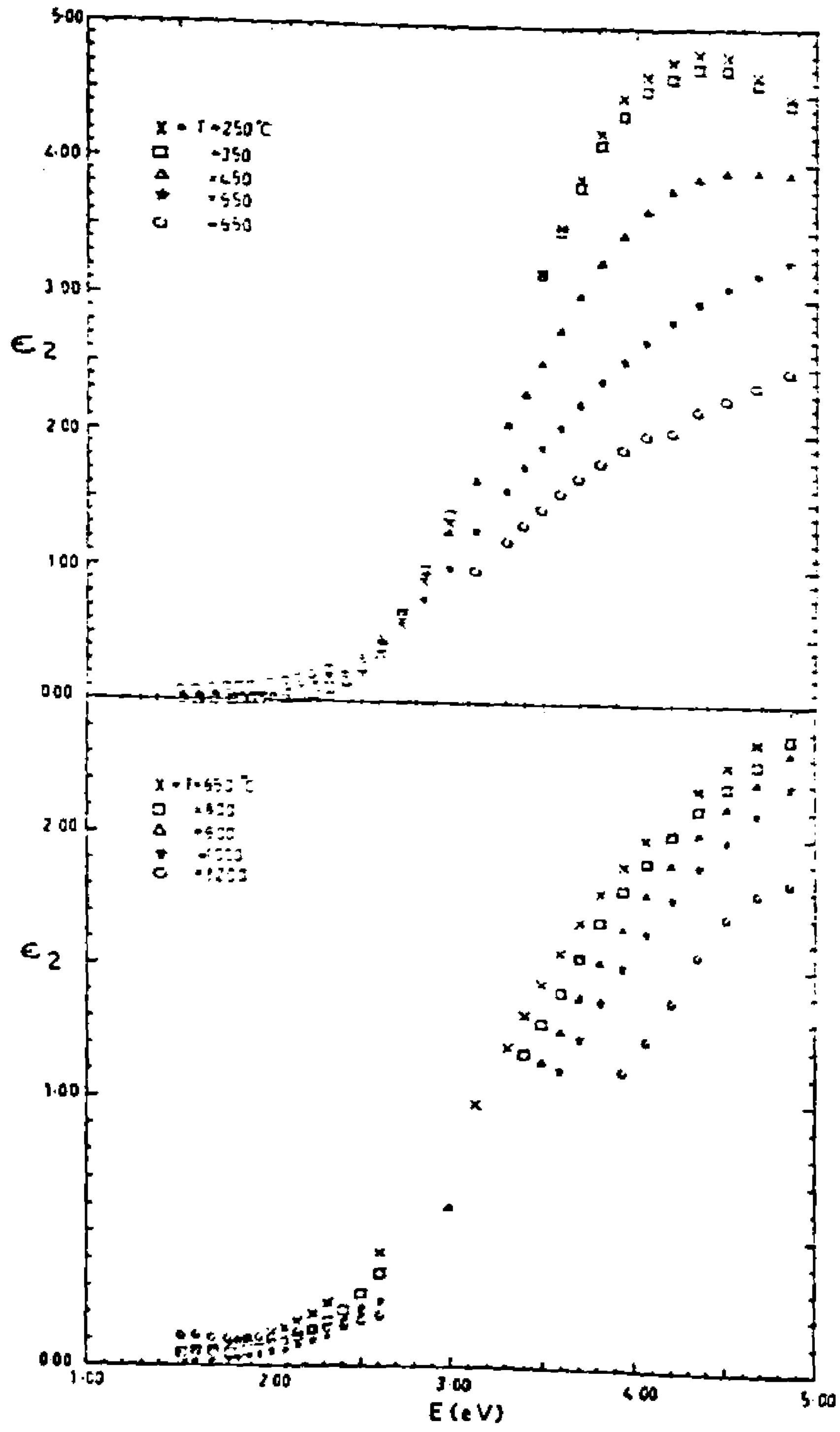

FIG. 6.10

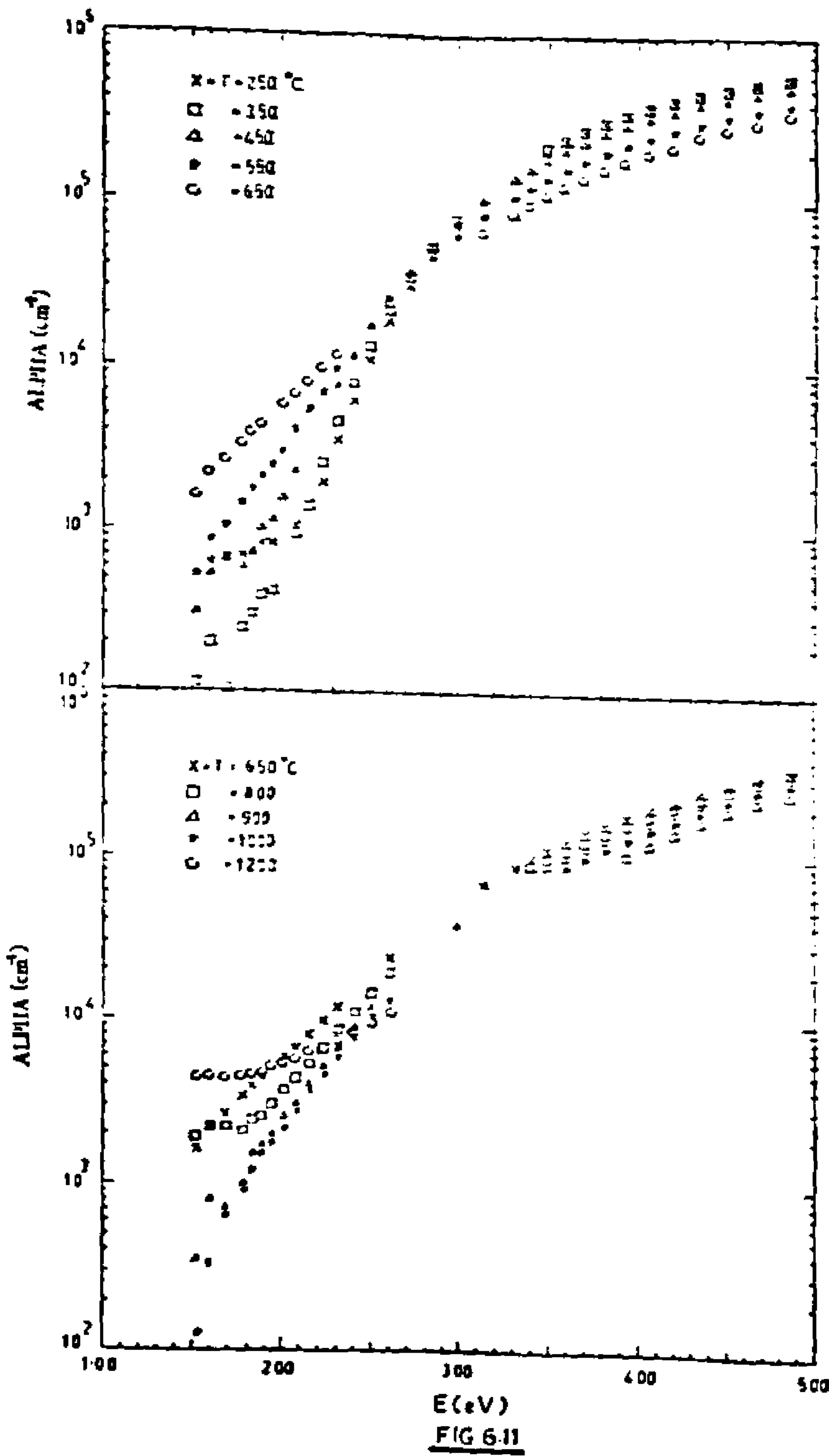

FIG 6.11

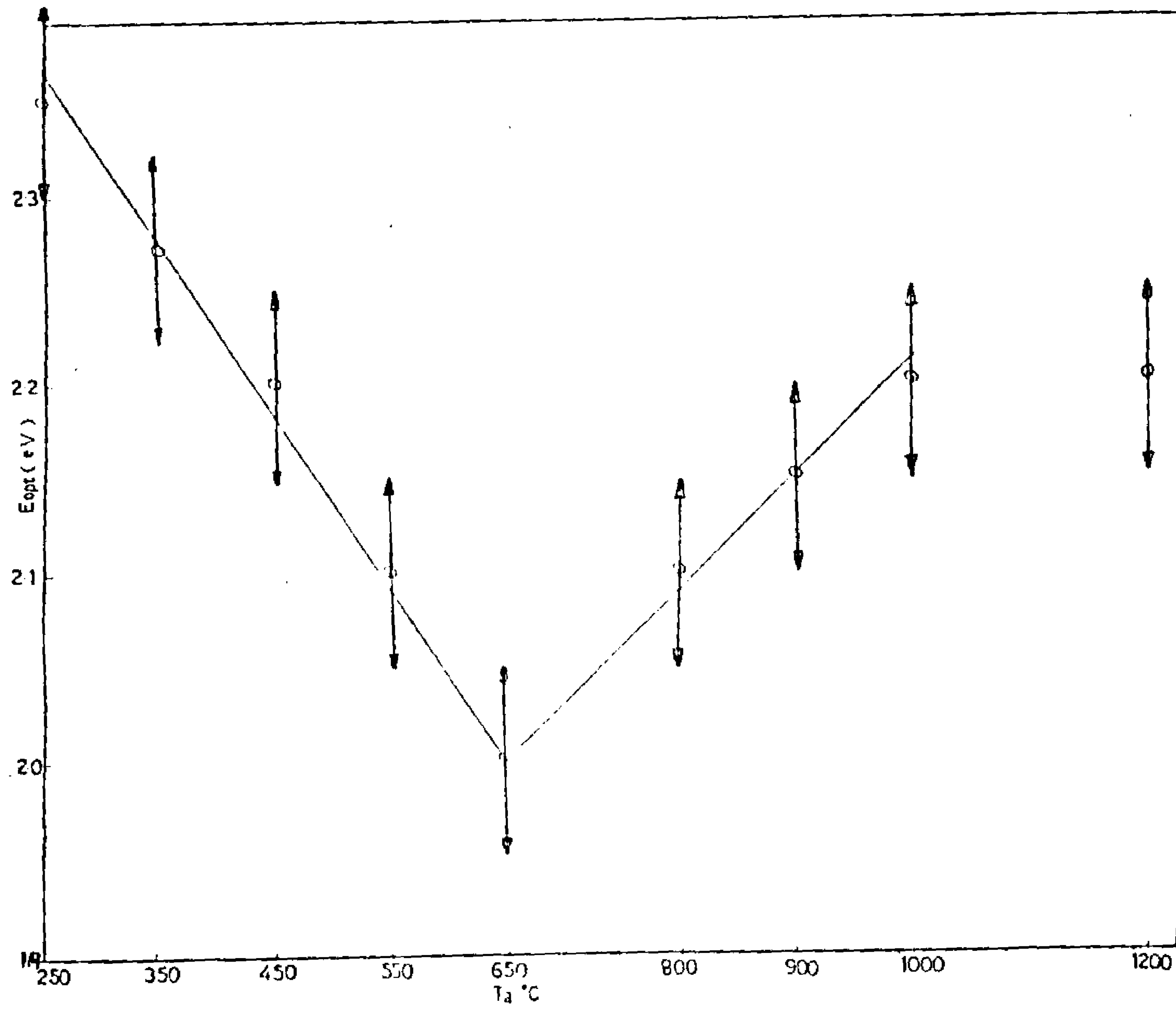

FIG 6.12

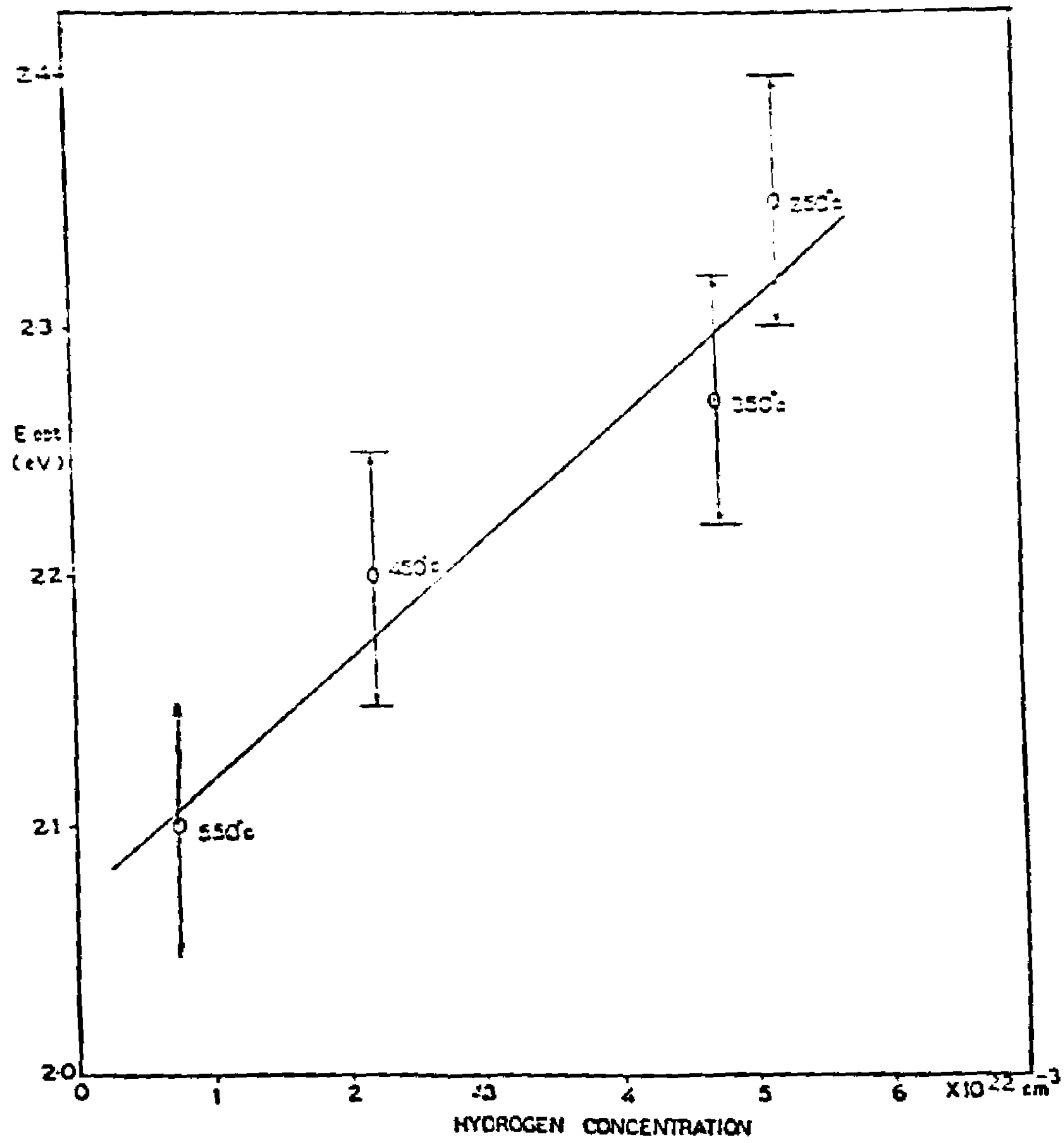

FIG. 6.13

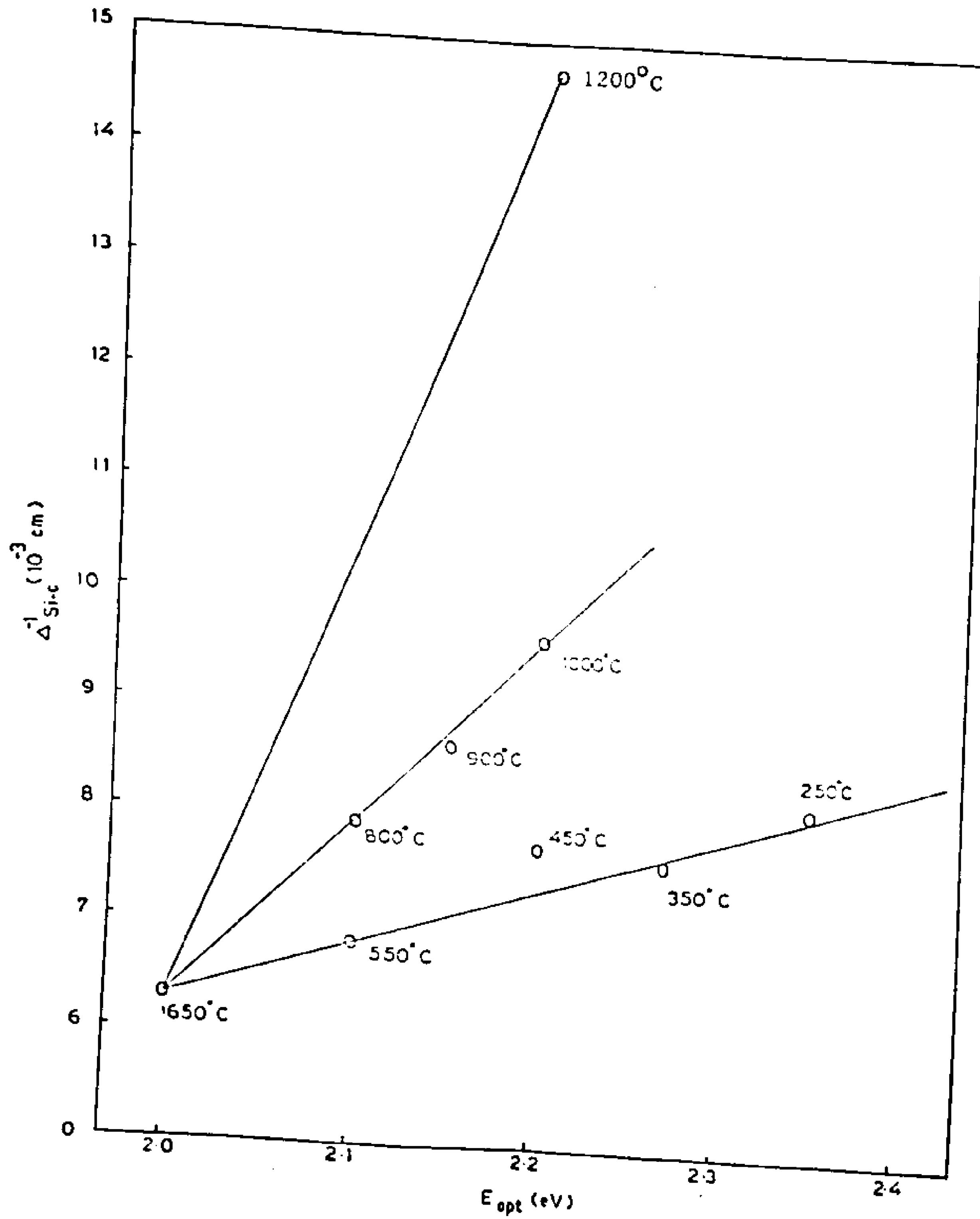

FIG-6.14

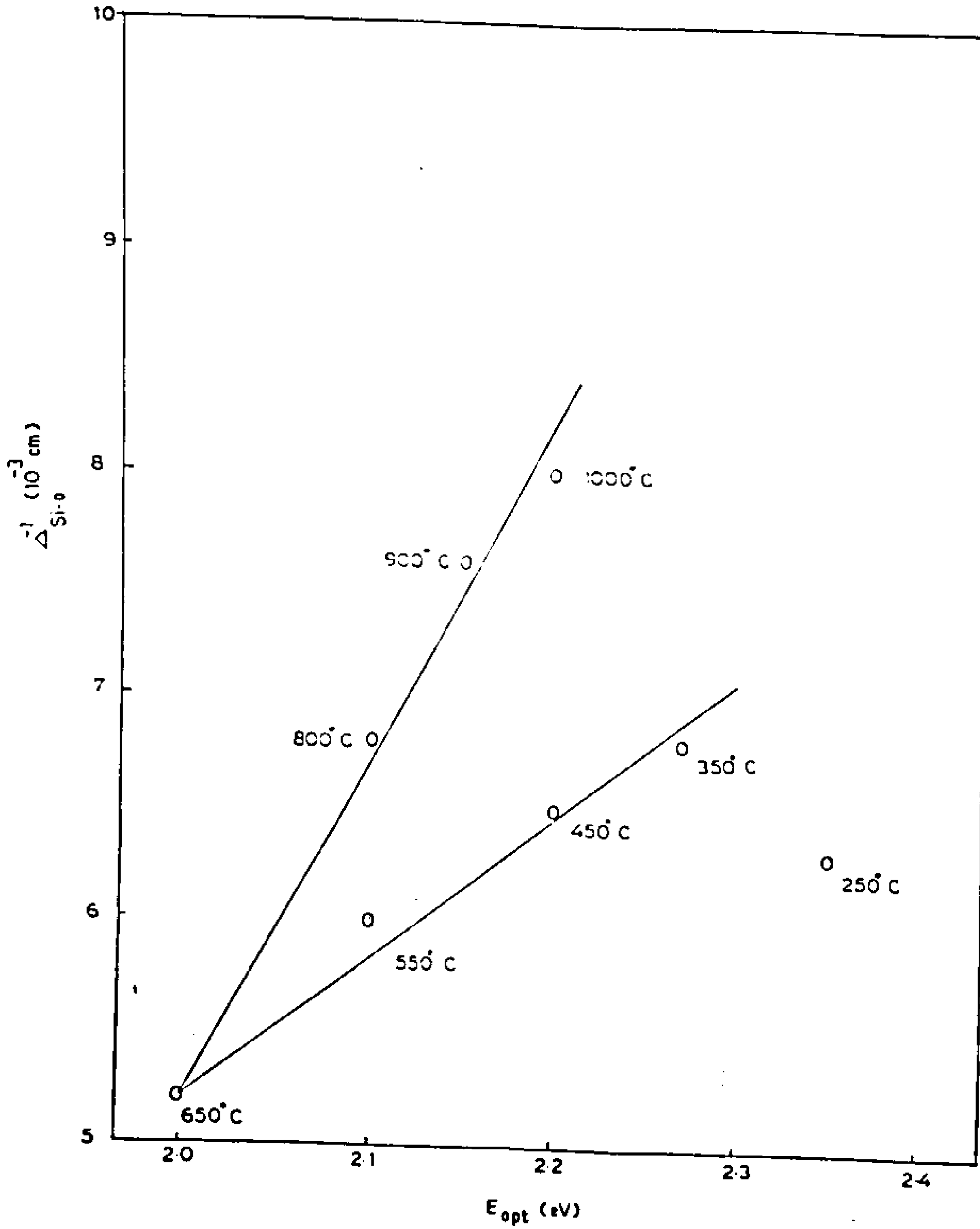

FIG-6·15

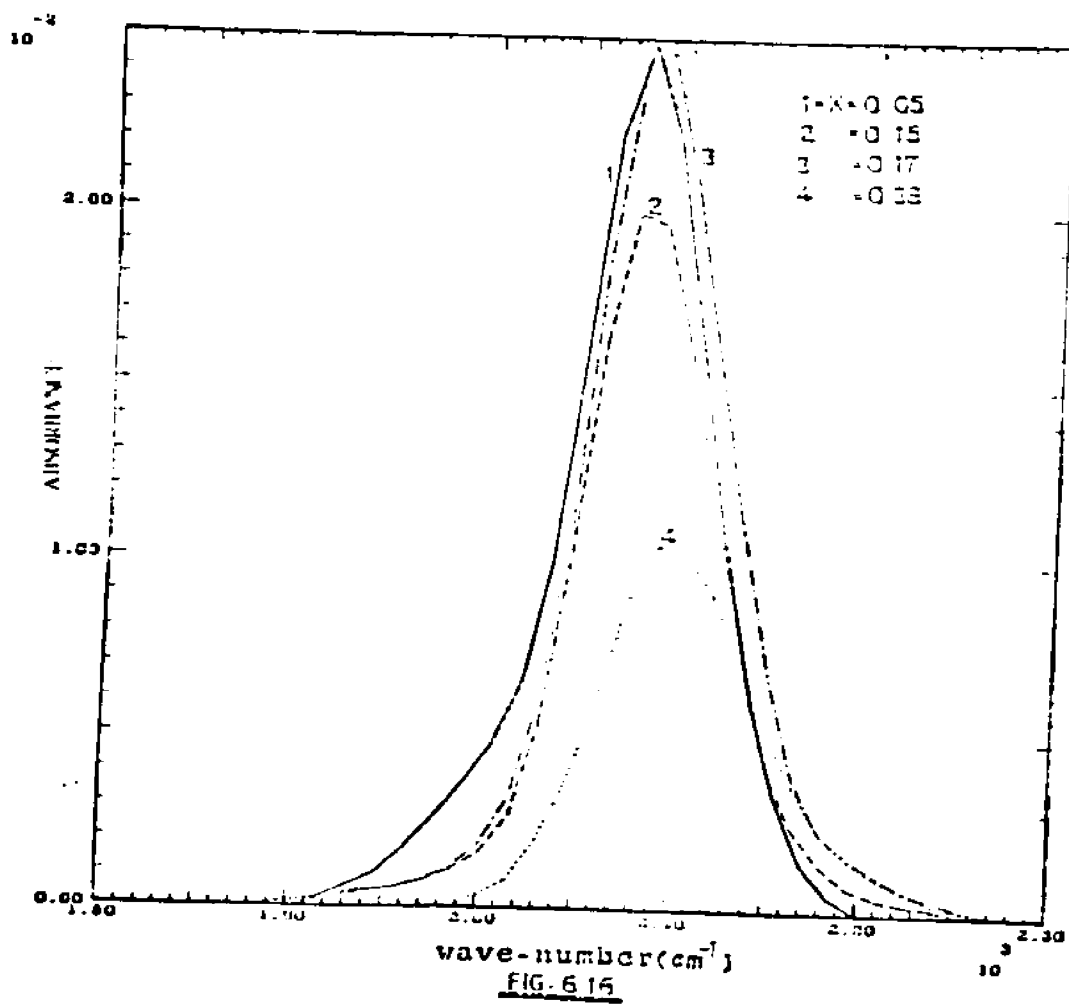

FIG. 6.16

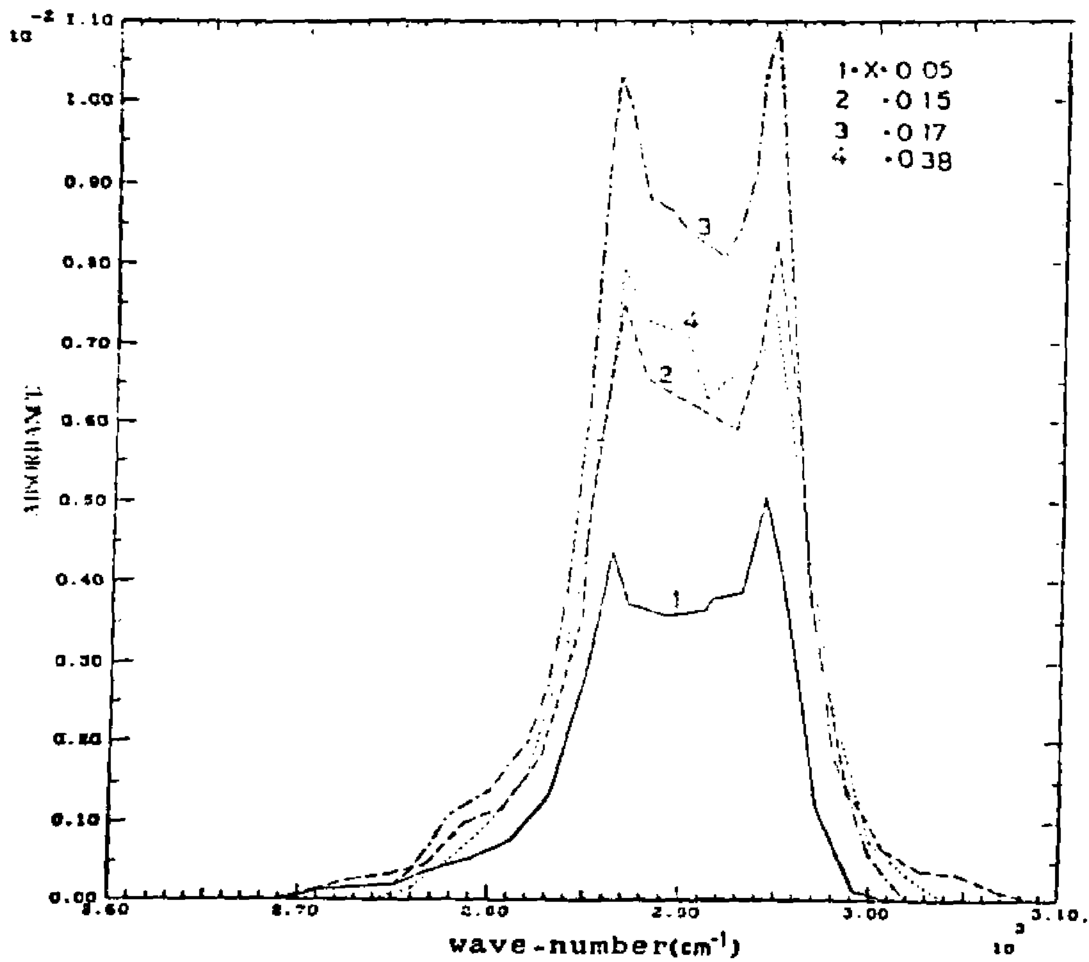

FIG. 6·17

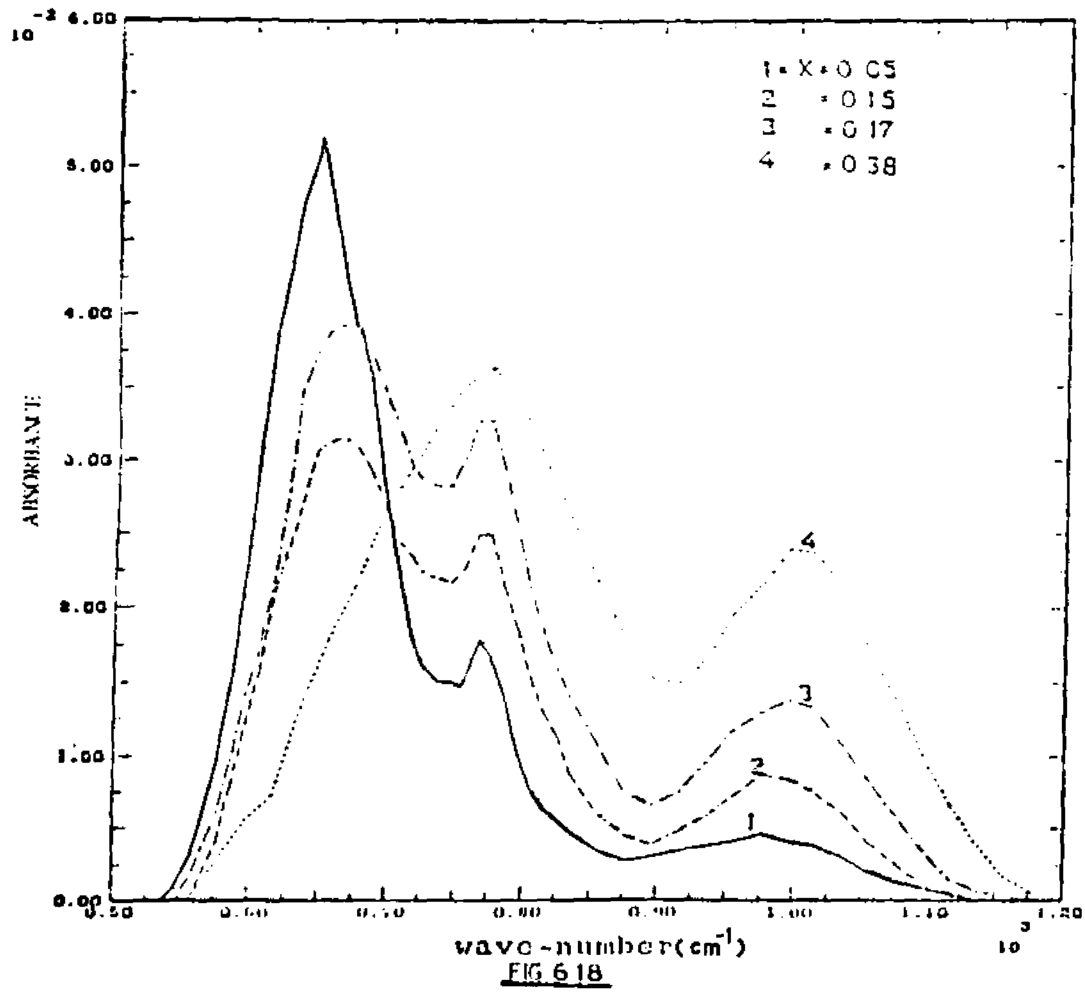

FIG 6.18

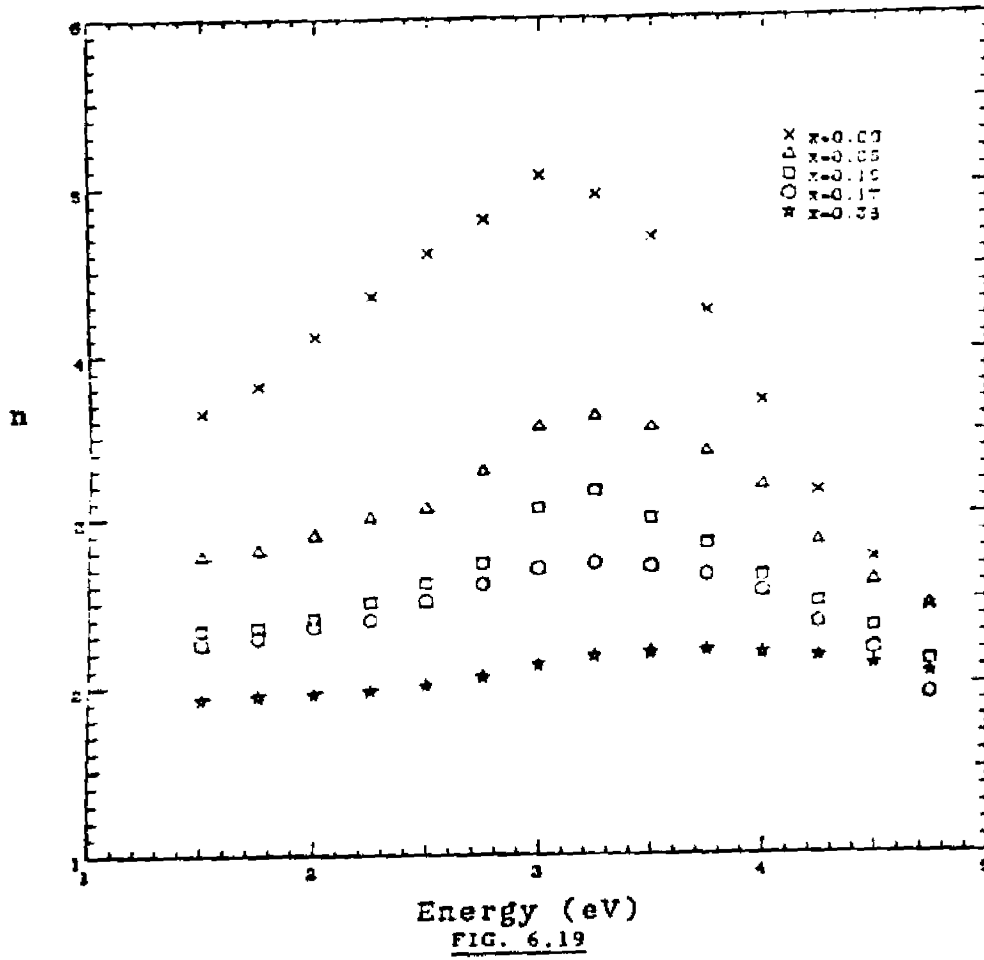

FIG. 6.19

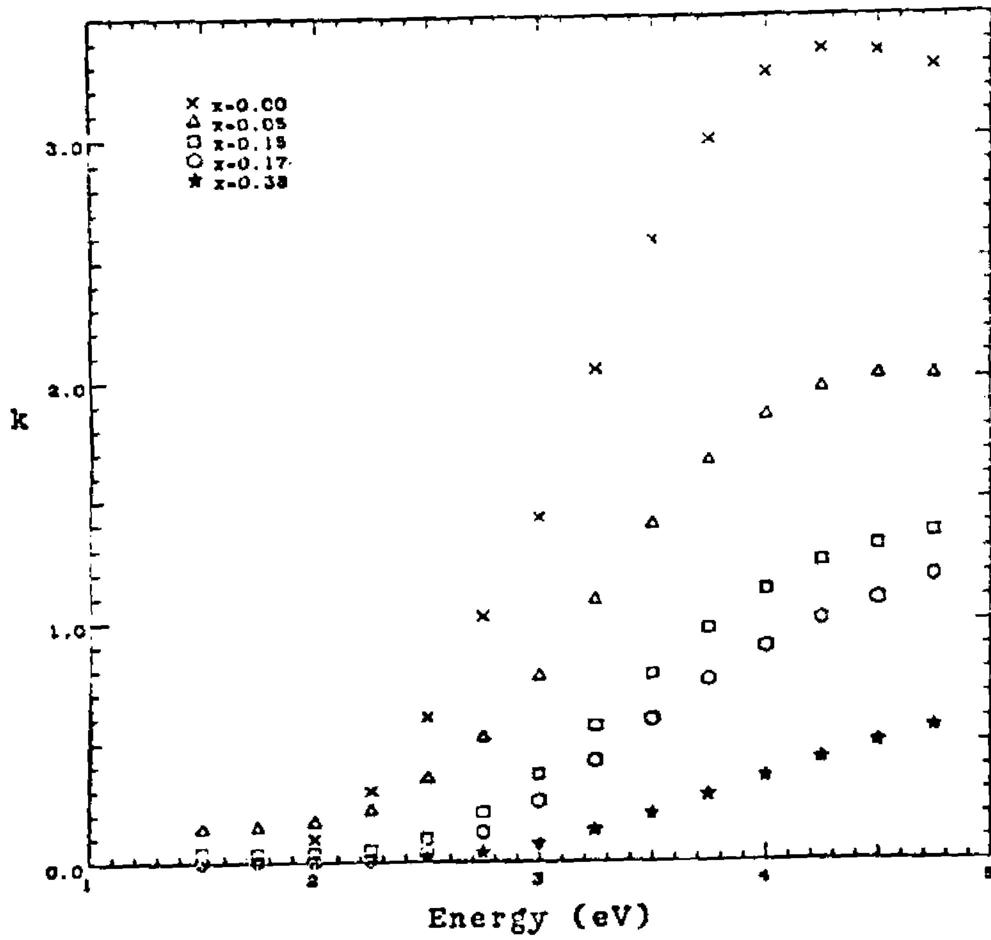

FIG. 6.20

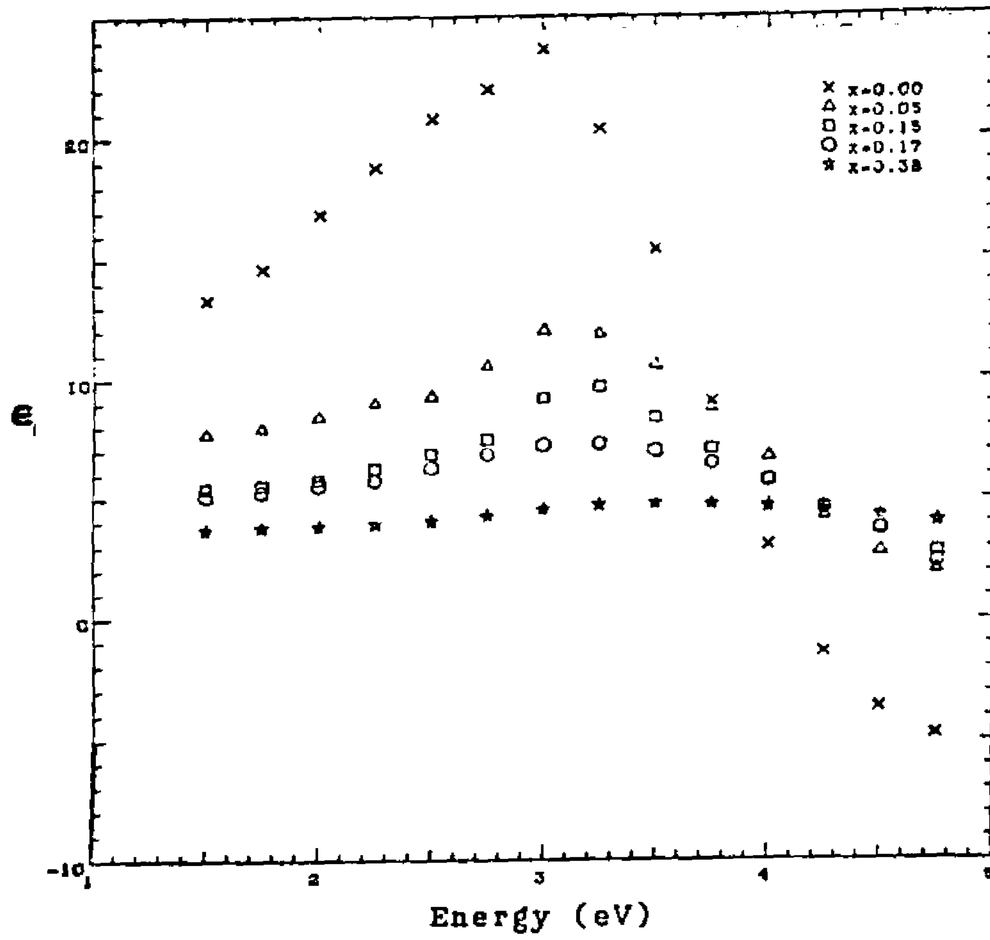

FIG. 6.21

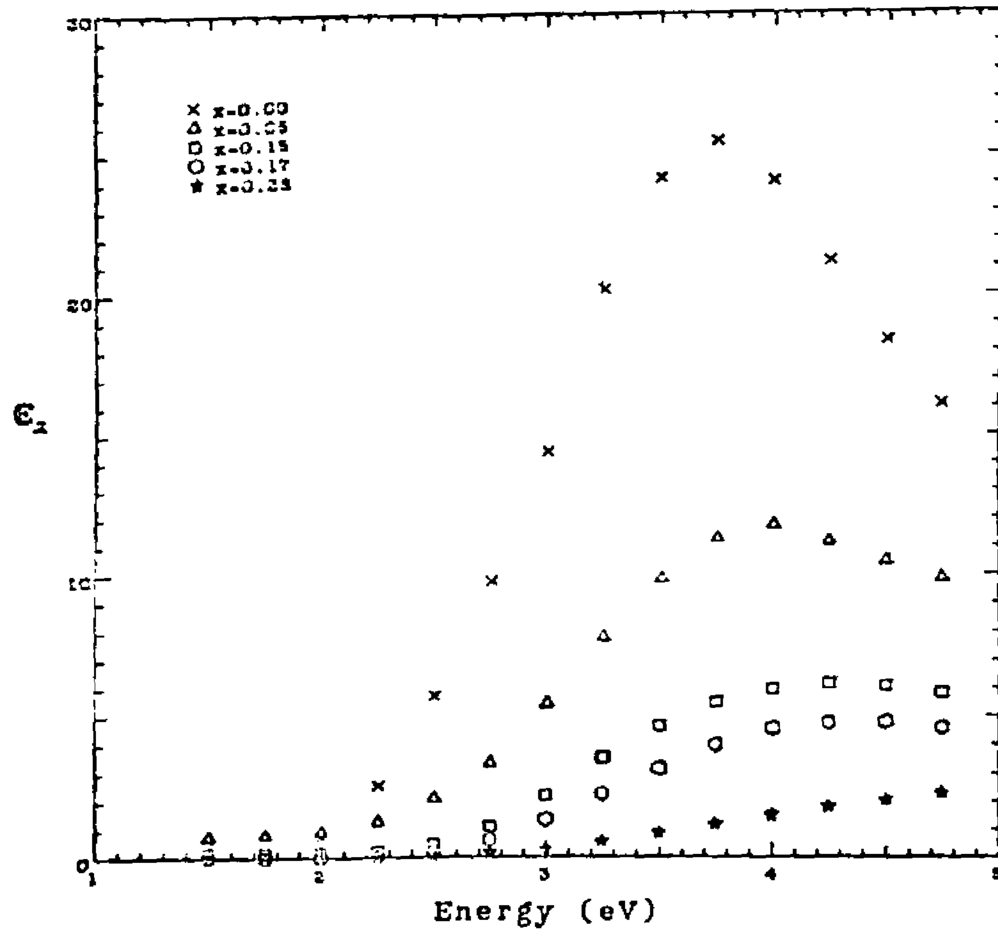

FIG. 6.22

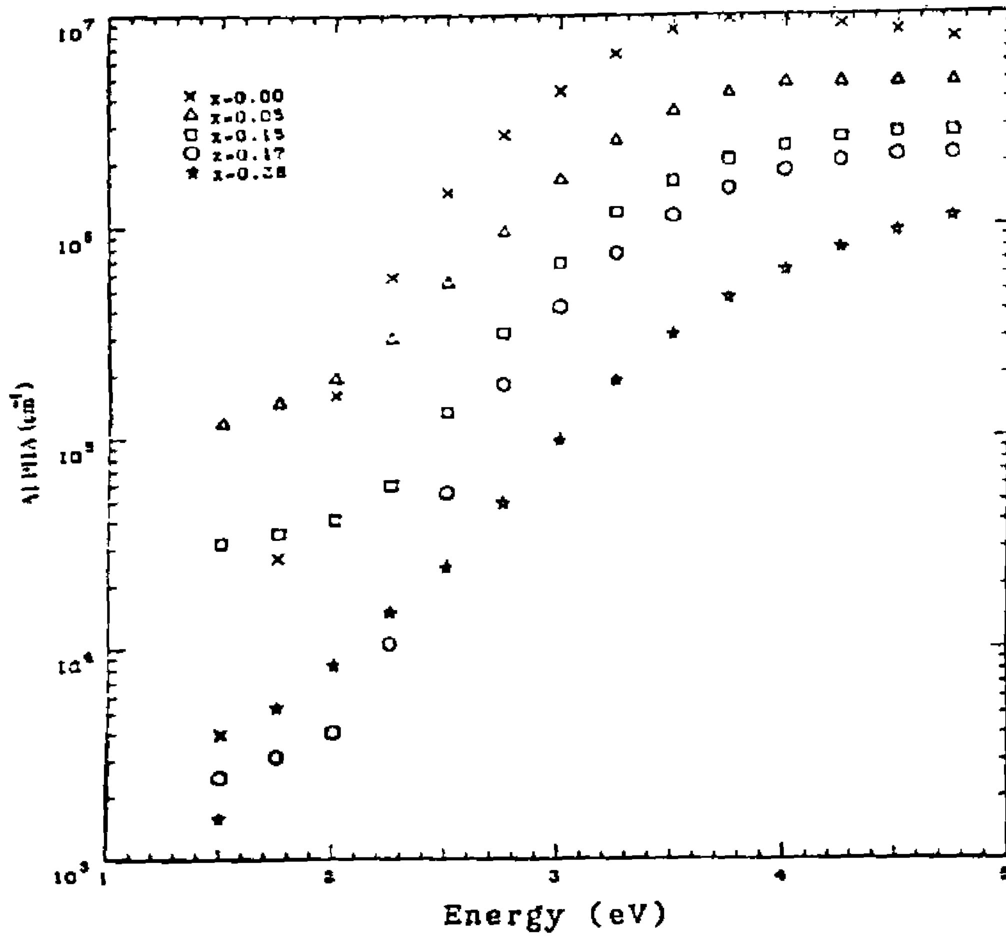

FIG. 6.23

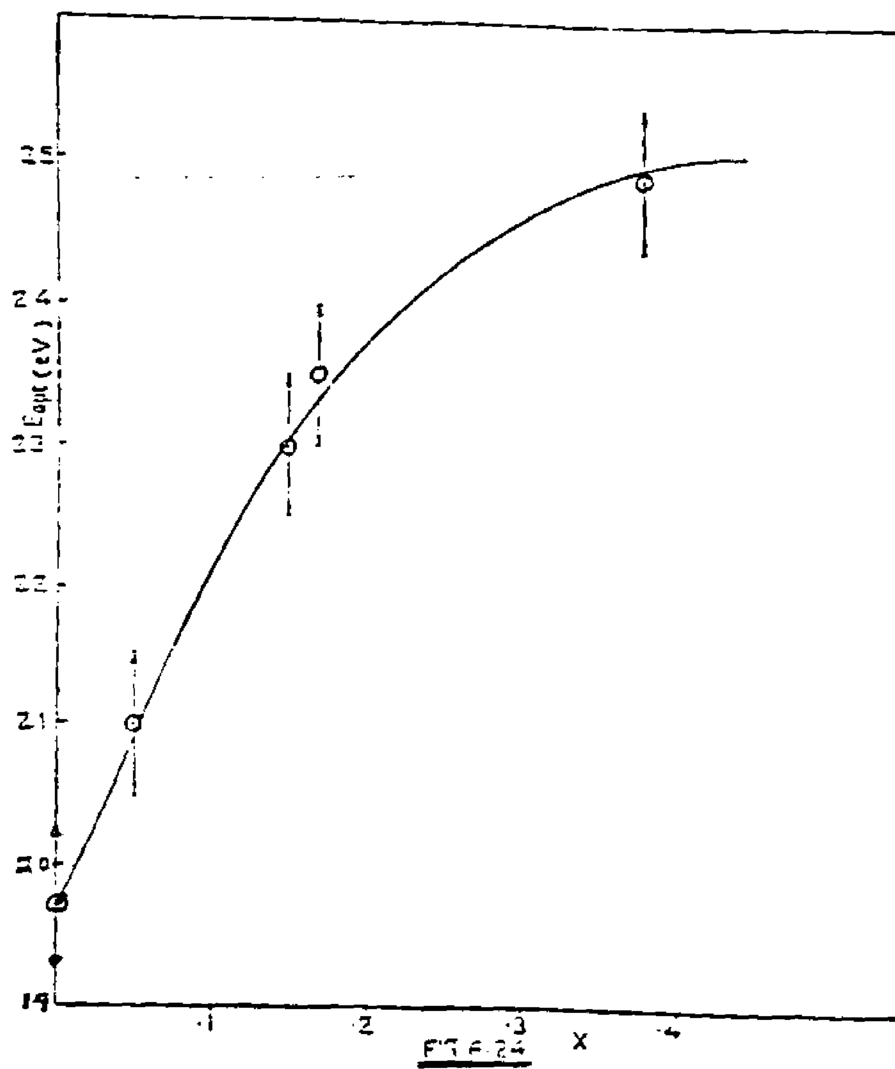

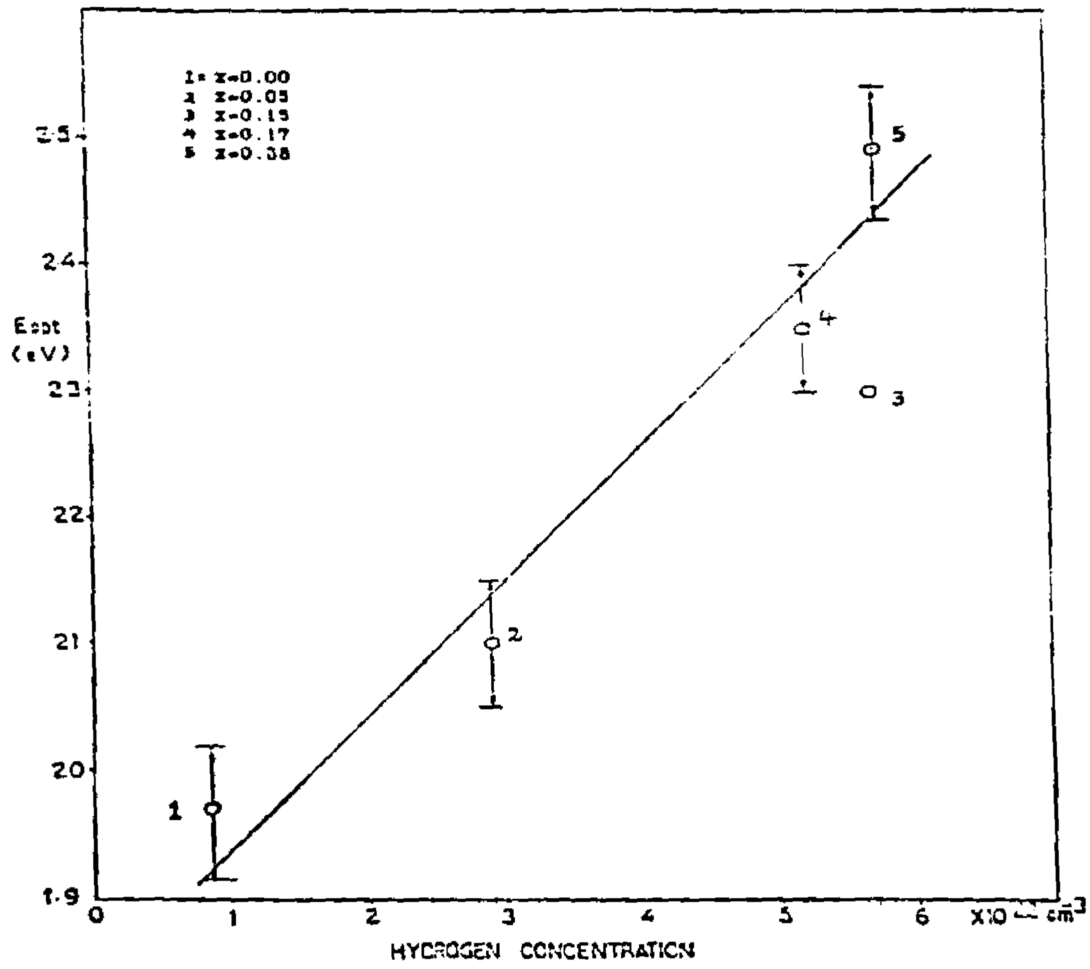

FIG 6.25

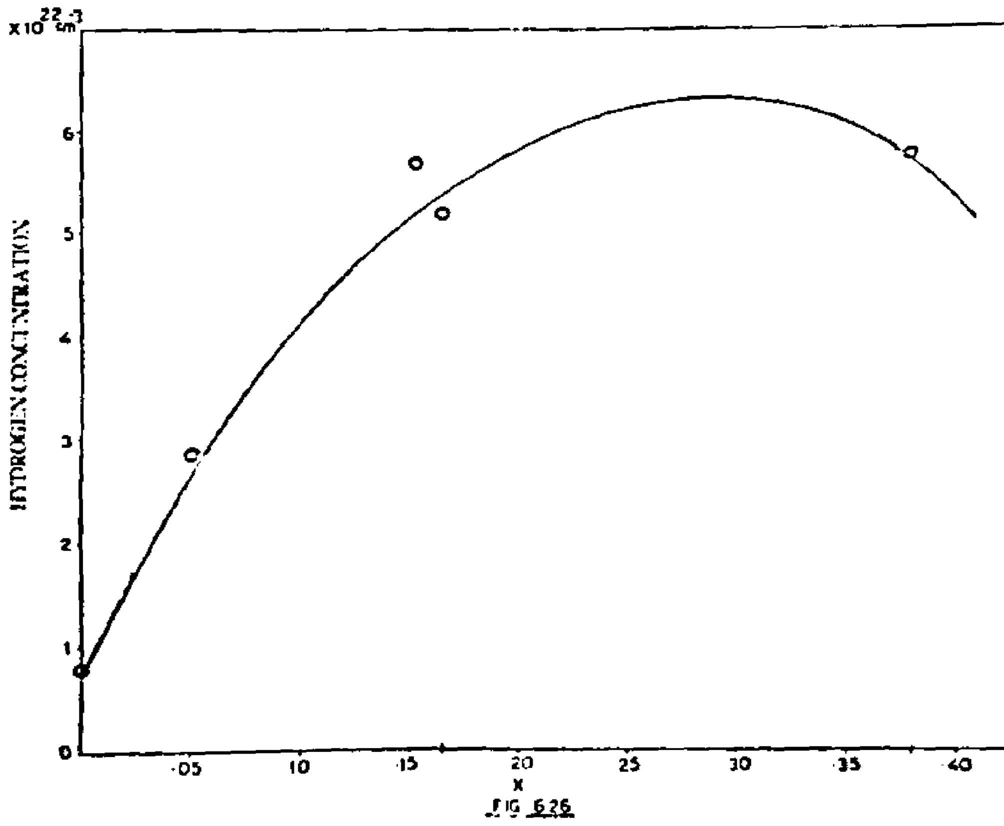

FIG 6.26

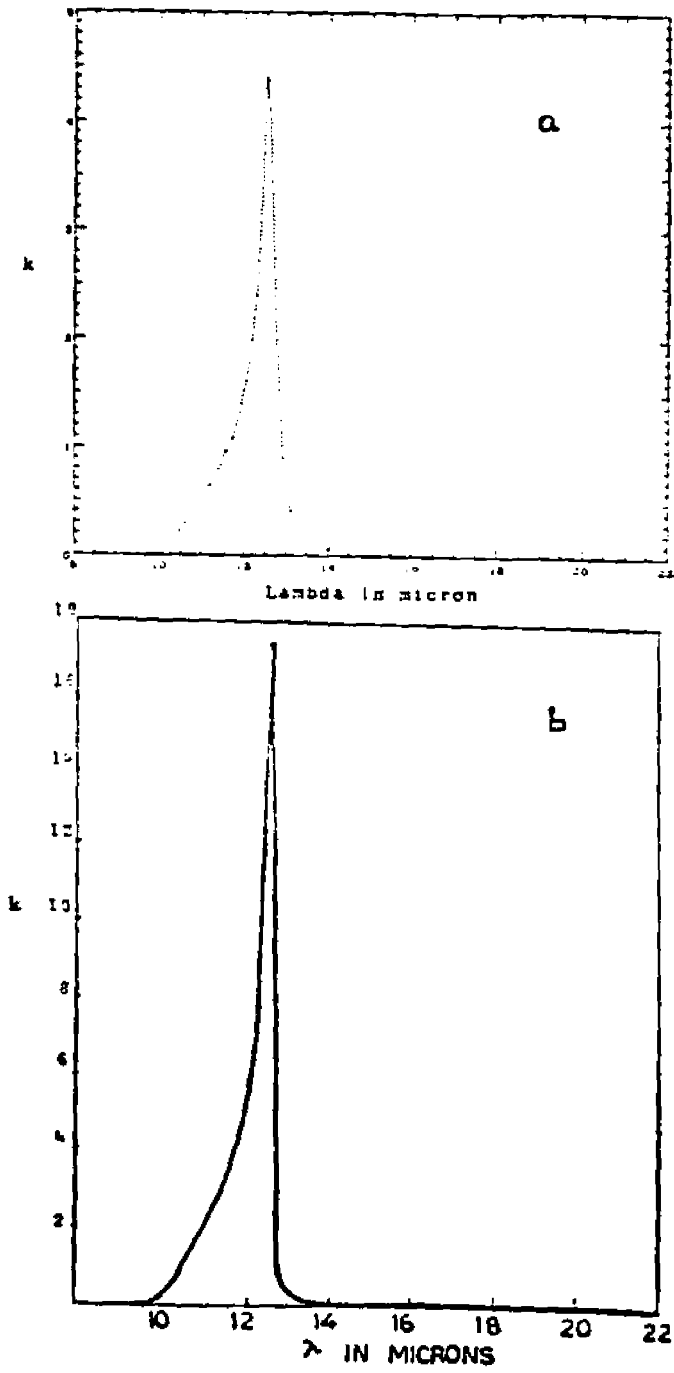

FIG. 6.27

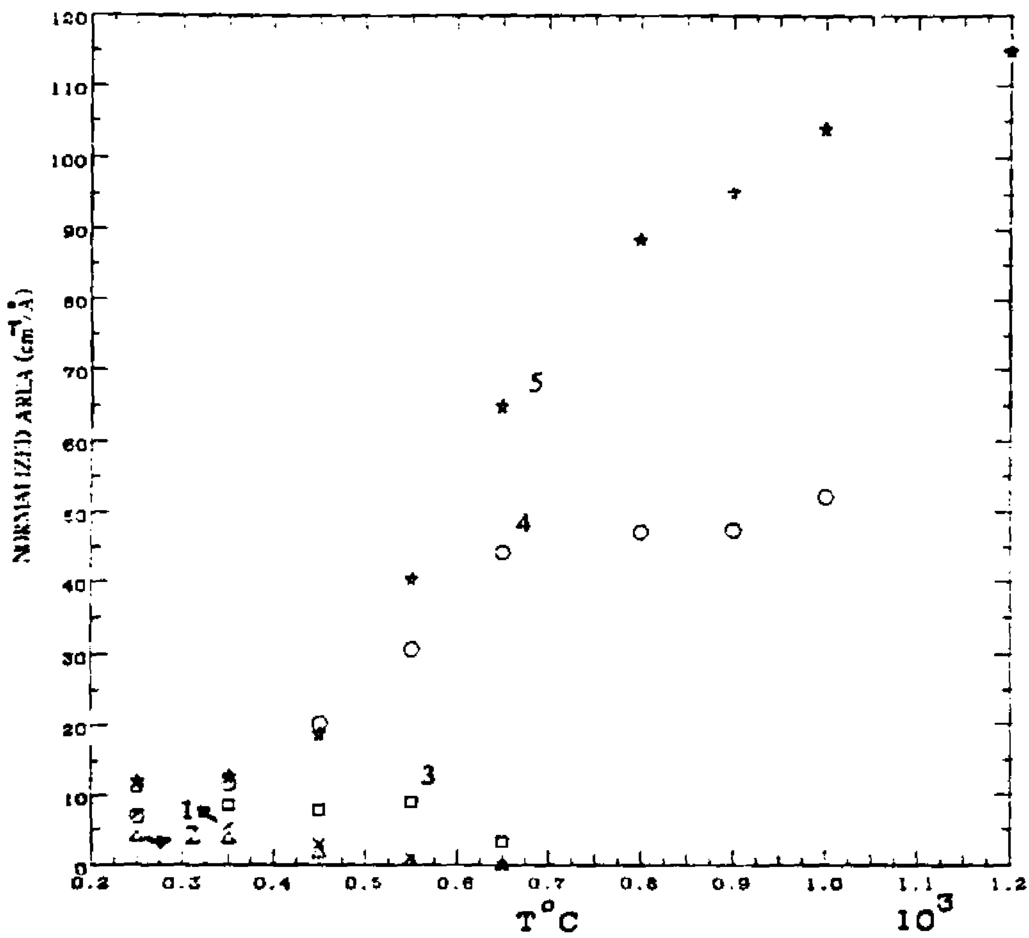

Fig. 6.I

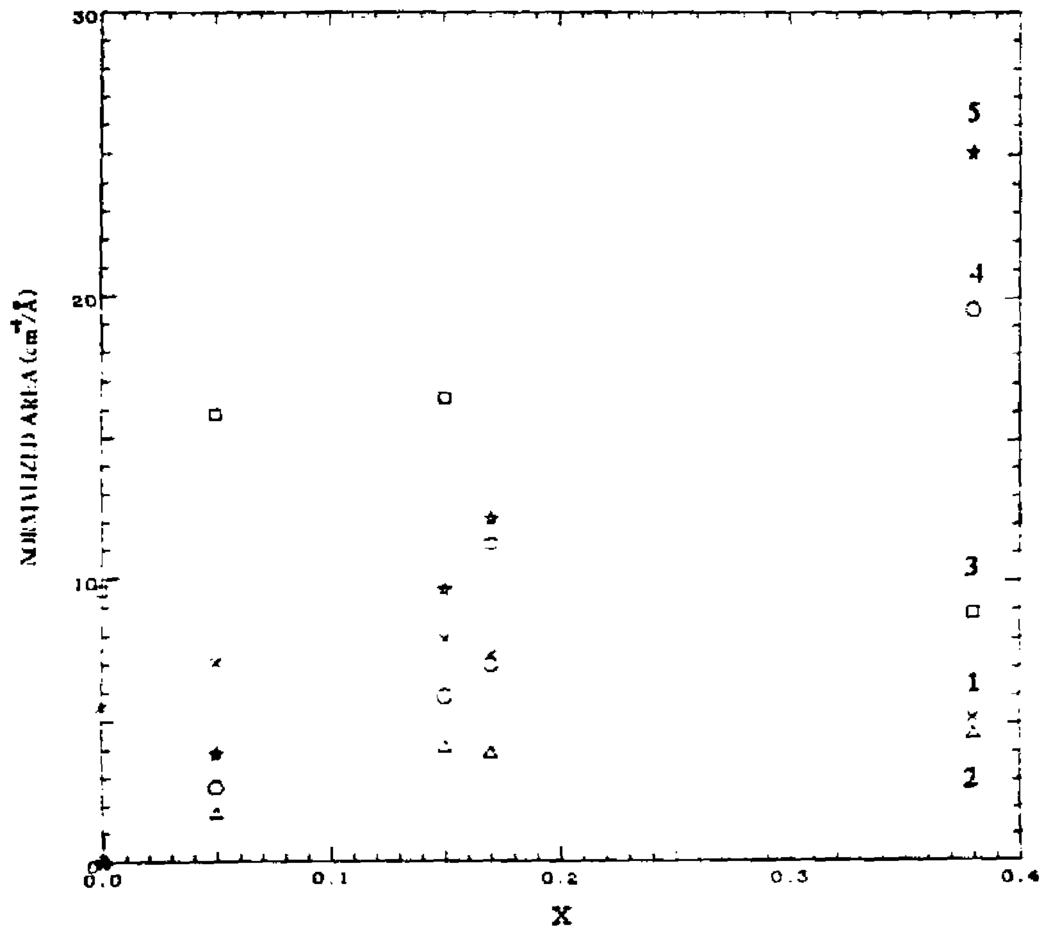

Fig. 6.II

Appendix I

The tetrahedron model[55] is developed for calculating ϵ_1 and ϵ_2 of amorphous silicon-carbon (a-$Si_{1-x}C_x$) alloys using Phillips-Van Vechten- Levine[106-108] dielectric model, along with the scaling procedure of Aspnes and Theeten.[17] This type of approach was first discussed by Philipp,[56] who proposed that the optical response of films based on silicon, oxygen, and nitrogen was determined by the response of Si-centered tetrahedra such as $Si\text{-}Si_{4-\nu}O_\nu$ and $Si\text{-}Si_{4-\nu}N_\nu$ ($\nu = 0,4$). Aspnes and Theeten[17] further developed this approach and combined it with the Bruggemann[49] effective medium approximation (EMA) and scaling of the dielectric function to determine ϵ_1 and ϵ_2 for $Si_{1-x}(SiO_2)_x$ and $Si_{1-x}(SiN_{4/3})_x$ mixtures.

I. Tetrahedron model

The model considers Si- and C- centered tetrahedra (i.e. $Si\text{-}Si_{4-\nu}C_\nu$ and $C\text{-}Si_{4-\nu}C_\nu$, $\nu = 0,4$) as the fundamental structural units determining the optical response of the alloy, films. The dielectric function for the film may be defined via the Bruggemann[49] EMA, given by the equations,

$$\sum_i v_i \frac{\epsilon_i - \epsilon}{\epsilon_i + 2\epsilon} = 0 \qquad (A.1)$$

$$\sum_i v_i = 1$$

where v_i and ϵ_i are the volume fraction and dielectric function, respectively, of the ith component. In this model we use ten components corresponding to ten distinct Si- and C- centered tetrahedra present in the films.

For calculating the complex dielectric function ϵ appropriate for the silicon-carbon alloy using the EMA expressed in Eq. (A.1) we need to know v_i and ϵ_i for the individual Si- and C- centered tetrahedra. We will first consider the volume fractions v_i which are functions of the individual tetrahedron volume V_i and tetrahedron probabilities P_i. We will then turn to the ϵ_i which will be obtained from our measured ϵ for a-Si:H using a scaling procedure whose parameters will be determined using the plasma sum rule and the dielectric model of Phillips, Van Vechten, and Levine.[106-108] We note that although hydrogen atoms have not been explicitly included at this stage in the Si- and C- centered tetrahedron model, their presence in a-$Si_{1-x}C_x$:H alloy films has been at least indirectly taken into account in the model as the ϵ_i spectra for individual tetrahedra have been scaled from the ϵ spectrum for a-Si:H which clearly does reflect the contribution of the incorporated hydrogen atoms.

A. Si- and C- centered tetrahedra: Probabilities and volume fractions.

The probabilities P for the individual Si-$Si_{4-\nu}C_\nu$ and C-$Si_{4-\nu}C_\nu$ (ν= 0-4) tetrahedra are functions both of the composition parameter x in these a-$Si_{1-x}C_x$ alloys and of the type of chemical ordering present in the films. For the case of no chemical ordering i.e. no preferential bonding between Si and C atoms, the probability for a particular bond in a given tetrahedron is simply proportional to the

fraction of atoms in the film available to complete that bond, i.e., (1-x) for a Si-Si bond in a Si- centered tetrahedron or for C-Si bond in a C- centered tetrahedron. The total probability P for a given tetrahedron is then equal to the product of (1) The probability for starting with a Si or C atom at the center of the tetrahedron. (2) The probabilities for the individual bonds within the tetrahedron. (3) A factor giving the number of possible ways of connecting the bonds within the tetrahedron. For example, for a $Si\text{-}Si_3C$ tetrahedron, the resultant probability $P = 4x(1-x)^4$ results from the product of four factors : (1-x) for having the Si atom at the center of the tetrahedron, $(1-x)^3$ for having three Si atoms bonded to central Si atom, x for having one C atom bonded to the central Si atom, and a factor of 4 for the possible ways of connecting the three Si and one C atoms to the four bonds available in the tetrahedron. The resulting probabilities P_i for the ten possible tetrahedra for the case of no chemical ordering are listed in Table A.I .

For the cases of complete chemical ordering with homogeneous dispersion and with phase separation, the tetrahedron probabilities P_i must take into account the fact that, in a Si- rich alloy, for example, C atoms will be bonded only to Si atoms. To determine the P_i for Si-rich alloys, we begin by defining f(Si)=(1-x) and f(C)=x as the fractions of Si and C atoms in the film. Also,

$f_1(Si)=f(Si)-f(C)=(1-x)-x = (1-2x)$

is the fraction of Si atoms which can bond to a given Si atom and $f(C)=f(C)=x$ is the fraction fo C atoms which can bond to a given Si atom. We note that $f_1(Si)$ is reduced below $f(Si)=(1-x)$ by an amount $f(C)=x$ since a fraction of $f(C)$ of the Si atoms must have their bonds effectively tied up by C atoms and thus, as a result of the complete chemical ordering, are effectively unavailable to bond to other Si atoms. Finally,

$f_2(Si)=f_1(Si)/[f_1(Si)+f_1(C)]=(1-2x)/(1-x)$

is the fraction of all atoms which can bond to Si atoms which are Si atoms. Likewise,

$f_2(C)=f_1(C)/[f_1(Si)+f_1(C)]=x/(1-x)$

is the fraction of all atoms which can bond to Si atoms which are C atoms.

The probability P_1 for a Si-Si_3C tetrahedron for the case of complete chemical ordering with homogeneous dispersion is given by

$$P_1=4f(Si)f_2^3(Si)f_2(C)$$
$$= 4(1-x)\left[\frac{(1-2x)}{(1-x)}\right]^3\left[\frac{x}{1-x}\right]$$

The remaining P_i for Si-rich and C-rich alloys for the case of homogeneous dispersion are given in Table A.I.

For the case of complete chemical ordering with phase separation, the only possible tetrahedra in a Si-rich alloy are Si-Si_4, Si-C_4, and C-Si_4, where the first tetrahedron

can be thought of as corresponding to a-Si and the remaining two as corresponding to a-SiC. The probability for the Si-Si_4 tetrahedron is given by

$$P_i = f(Si) f_2(Si)(1)^3$$
$$= (1-x)\left[\frac{(1-2x)}{(1-x)}\right] = (1-2x)$$

since if a single Si atom is bonded to the central Si atom, then all of the three remaining atoms must also be Si atoms (i.e. with unit probability). For the Si-C_4 tetrahedron, we have

$$P_i = f(Si) f_2(C)(1)^3$$
$$= (1-x)\left[\frac{x}{1-x}\right] = x$$

for similar reasons, while for C-Si_4 tetrahedron, we have $P_i = f(C)(1)^4 = x$ due to the existence of complete chemical ordering with phase separation.

The tetrahedron probabilities for the case of no chemical ordering, complete chemical ordering with homogeneous dispersion, and complete chemical ordering with phase separation, respectively, are given in Table A.I.

The contribution of each tetrahedron to the optical response of an a-$Si_{1-x}C_x$:H alloy film is determined both by its dielectric function ϵ_i and its volume fraction ν_i in the film. The individual ν_i are given by $P_i V_i / \sum P_i V_i$, where V_i is the volume associated with the ith tetrahedron. For a tetrahedron with all like atoms, e.g., Si-Si_4, the volume of the tetrahedron is given by $V_{tet} = 8a^3/9\sqrt{3}$, where a=d(Si-Si) is the Si-Si bond length, equal to 2.35 Å. However, in

crystalline Si, in order to account for the entire volume of the crystal, the volume associated with each Si-Si tetrahedron is actually $V = 3\ V_{tet}$. This extra factor of 3 is necessary, for example, in calculating atomic densities. Similarly, for tetrahedra such as $Si-Si_3C$, we have $V_{tet} = 2a^2(a+3b)/9\sqrt{3}$, where a=d(Si-Si) and b=d(Si-C)= 1.884 Å. Finally, for tetrahedra such as $Si-Si_2C_2$ we have $V_{tet} = 4ab(a+b)/9\sqrt{3}$, with a=d(Si-Si) and b=d(Si-C). Note that d(C-C)=1.542 Å. Using these expressions for V_{tet}, and including the necessary factor of three as discussed above, the volumes V_i associated with each of the ten tetrahedra are listed in Table A.II.

B. Scaling of ϵ_1 and ϵ_2

The dielectric response ϵ_i of the tetrahedra which are listed in Table A.I are, in general, not directly available from experiment. Aspnes and Theeten[17] have shown, however, that it is possible to determine $\epsilon_i = \epsilon_1 + i\ \epsilon_2$ for each tetrahedron by scaling from the measured E for amorphous Si. The measured ϵ for amorphous Si will in fact be taken to be the ϵ_i for the $Si-Si_4$ tetrahedron. This scaling approach is based on the expression.

$$\epsilon_i(E) - 1 = C_{1i}\left[\epsilon_{a\text{-}Si:H}(C_{2i}E) - 1\right] \qquad (A.2)$$

where E is the photon energy and C_{1i} and C_{2i} are scaling parameters appropriate to the ith tetrahedron, to be defined below using the plasma sum rule and the Phillips-Van Vechten-Levine (PVVL)[106-108] dielectric model. The scaled ϵ_i spectra for the tetrahedra will indirectly include the

effect of the hydrogen as we have scaled from our measured ϵ of a-Si:H

Aspnes and Theeten[17] have indicated that when Eq.(A.2) and the plasma sum rule given by

$$n_{eff}(E) = \left(\frac{m}{2\pi^2 e^2 \hbar^2}\right) \int_0^{E} E' \epsilon_2(E')\, dE' \qquad (A.3)$$

are taken together, then the following relationship between the scaling parameters C_{1i} and C_{2i} can be obtained:

$$C_{1i} = \left[n(i)/n(a\text{-}Si{:}H)\right] C_{2i}^2 \qquad (A.4)$$

Here n(i) and n(a-Si:H) are the density of bonding electrons associated with the ith tetrahedron and with a-Si:H, respectively.

The scaling parameter C_{2i} for the energy will now be shown to be simply related to E_g, the average energy gap parameter in PVVL[106-108] dielectric model. We note that the real part of Eq.(A.2), when evaluated at zero energy, can be written as

$$\epsilon_{1i}(0) - 1 = C_{1i}\left[\epsilon_{1\,a\text{-}Si:H}(0) - 1\right] \qquad (A.5)$$

By using the expression $\epsilon_1(0) - 1 = A\left(\frac{\hbar\omega_p}{E_g}\right)^2$ where A is a constant and $\hbar\omega_p$ is the plasma energy ($\omega_p^2 = 4\pi n e^2/m$) Eq.(A.5) can be written in the form

$$A(\hbar\omega_p/E_g)_i^2 = C_{1i}\, A(\hbar\omega_p/E_g)^2_{a\text{-}Si:H} \qquad (A.6)$$

Given that $(\hbar\omega_p)_i^2 \propto n(i)$ and $(\hbar\omega_p)^2 \propto n(a\text{-}Si{:}H)$, Eq.(A.6) can be rearranged to yield

$$C_{1i} = \left[n(i)/n(a\text{-}Si{:}H)\right]\left[E_g(a\text{-}Si{:}H)/E_{gi}\right]^2 \qquad (A.7)$$

Comparing Eq. (A.7) with equation (A.4), we can see that the energy scaling parameter C_{2i} is given by

$$C_{2i} = E_g(a\text{-}Si{:}H)/E_{gi} \qquad (A.8)$$

C. Dielectric model for the average energy gap parameter E_g

The average energy-gap parameter E_g of the dielectric model of PVVL does not correspond to any particular energy gap in the band structure, but rather is an average over all the bands. As such, E_g can be calculated from the PVVL dielectric model using the following relationships which have been generalized to and are appropriate for the Si-centered tetrahedra listed in Table A.II (using the notation $Si\text{-}Si_{4-\nu}C_\nu$)

$$E_g^2 = E_H^2 + C^2 \tag{A.9a}$$

$$E_H = (7.123\,eV)(\langle r\rangle)^{-2.48} \tag{A.9b}$$

$$\langle r\rangle = (4-\nu)\,r(Si\text{-}Si)/4 + \nu\, r(Si\text{-}C)/4 \tag{A.9c}$$

$$C = (14.4\,eV)\, b \exp(-k_s\langle r\rangle)\left[Z_{Si}/r(Si\text{-}Si) - \langle Z_i/r_i\rangle\right] \tag{A.9d}$$

$$b = 0.089\, N_c^2 \tag{A.9e}$$

$$k_s = (4k_f/\pi a_b)^{1/2} \tag{A.9f}$$

$$k_f = [3\pi^2 n(i)]^{1/3} \tag{A.9g}$$

Here E_H and C are the homopolar (covalent) and heteropolar (ionic) parts of E_g. $\langle r\rangle$ is one half of the average bond length between the central (Si) atom and the four other atoms in the tetrahedron, with r(Si-Si) = d(Si-Si)/2 = 1.176 Å, r(Si-C) =0.942 Å and r(C-C)=0.771 Å . In Eq.(A.9d) for C, Z_{Si} = 4 and $Z_i = Z_{Si}$ or Z_C = 4 (as appropriate). The average $\langle Z_i/r_i\rangle$ in Eq.(A.9d) is taken over the four atoms surrounding the central (Si) atom in the tetrahedron, with r = r(Si-Si) or r(C-C) as appropriate. Finally, N_C is the average coordination number of the atoms in the crystal

(equal to 4 for $Si_{1-x}C_x$ alloys), a_B is the Bohr radius, and n(i) is the density of the bonding electrons in the ith tetrahedron, given by n(i)= $4/V_i$, where the V_i are the volumes associated with the tetrahedra in Table A. II. Equations (A.9a)-(A.9g) are also appropriate for C-centered tetrahedra ($C-Si_{4-\nu}C_\nu$, ν = 0-4), when r(Si-Si) and Z_{Si} are replaced by r(C-C) and Z_C, respectively. We note that C_{1i} and C_{2i} for the $Si-C_4$ and $C-Si_4$ tetrahedra listed in Table A.II are identical , indicating that these two tetrahedra have the same dielectric response, as expected.

II. Tetrahedron model - Predictions

Making use of the values of C_{1i} and C_{2i} for the individual tetrahedra listed in Table A.II and measured dielectric function data for a-Si:H, we have used Eq.(A.2) to generate scaled ϵ_i spectra for the Si- and C- centered tetrahedra. The results which we have used for $\epsilon_{a-Si:H}$ in the range 1.5 to 4.75 eV have been extrapolated down to 0 eV using the single oscillator expression for $\epsilon_2(E)$, see Eq. (A14) of Ref 109. The ϵ_1 and ϵ_2 spectra for $a-Si_{1-x}C_x$:H alloys will now be generated by using ϵ_i of the Si- and C-centered tetrahedra as the components in the EMA as expressed by Eq.(A.1). The procedure for obtaining ϵ_1 and ϵ_2 for a given composition x involves (1) choosing which type of chemical ordering is to be considered (2) calculate the appropriate probabilities $P_i(x)$ from Table A.I, (3) calculating the volume fractions $v_i(x)$ for each tetrahedron

according to

$$v_i(x) = P_i(x) V_i / \sum P_i(x) V_i$$

where the V_i are the tetrahedron volumes listed in Table A.II and the sum in the denominator is over all the possible tetrahedra, Substituting the $v_i(x)$ and the appropriate ϵ_{1i} and ϵ_{2i} from above for the tetrahedra into Eq.(A.1) we obtain the resulting ϵ_1 and ϵ_2 corresponding to the alloy of composition x. Using the above procedure as outlined in this Appendix we can calculate ϵ_1 and ϵ_2 for the tetrahedral components.

APPENDIX II

Peak positions for Si-H stretch for all bonding configurations using Lucovsky's approach[83]

Bonding configuration	Frequency (cm^{-1})
$Si-Si_3H$	2013
$Si-Si_2CH$	2054
$Si-SiC_2H$	2095
$Si-C_3H$	2135
$Si-Si_2OH$	2103
$Si-SiO_2H$	2192
$Si-O_3H$	2282
$Si-SiCOH$	2144
$Si-C_2OH$	2184
$Si-CO_2H$	2233
$Si-Si_2H_2$	2089
$Si-SiCH_2$	2119
$Si-C_2H_2$	2149
$Si-SiOH_2$	2155
$Si-COH_2$	2185
$Si-O_2H_2$	2220

REFERENCES

1) D.A. Anderson and W.E. Spear, Philos. Mag. 35, 1 (1977)

2) T. Shimada, Y. Katayama, and K.F. Komatsubara, J.Appl. Phys. 50, 5530 (1979)

3) H. Wieder, M. Cardona, and C.R. Guarnieri, Phys. Status Solidi B 92, 99 (1979)

4) Y. Katayama, K. Usami, and T. Shimada, Philos. Mag. B 43, 283 (1981)

5) R. Sussmann and R. Ogden, Philos. Mag. B 44, 137 (1981)

6) Y. Katayama, T. Shimada, and K. Usami, Phys. Rev. Lett. 46, 1146 (1981)

7) N. Saito, T. Yamada, T. Yamaguchi, I. Nakaaki, and N.Tanaka, Philos. Mag. B 52, 987 (1985)

8) J.Tafto and F.J.Kampas, Appl. Phys. Lett. 46, 949 (1985)

9) A.H. Mahan, B.Von Roedern, D.L. Williamson, and A.Madan J.Appl. Phys. 57, 2717 (1985)

10) K. Mui, D.K. Basa, and F.W. Smith, J.Appl. Phys. 59, 582 (1986)

11) Y. Tawada, H. Okamoto, and Y. Hamakawa, Appl.Phys.Lett. 39, 237 (1981)

12) Y. Tawada, K. Tsuge, M.Kondo, H.Okamoto, and Y.Hamakawa J.Appl. Phys. 53, 5273(1982)

13) D.R. McKenzie, N. Savvides, D.R. Mills, R.C. McPhedran, and L.C.Botten, Solar Energy Mater 9, 113 (1983)

14) B.G. Yacobi, B. Von Roedern, A.H. Mahan, and K.M. Jones Phys. Rev. B 31, 8257 (1984)

15) F.W.Smith, J.Appl. Phys. 55, 764 (1984)

16) K. Mui, D.K. Basa, F.W. Smith, and R. Corderman Phys. Rev. B35, 8089 (1987)

17) D.E.Aspnes and J.B.Theeten J.Appl.Phys. 50, 4928 (1979)

18) J. Tauc, R. Grigorovici, and A. Vancu, Phys. Status Solidi 15, 627 (1966)

19) G.A.N. Connell in Amorphous Semiconductors, Vol 36 of Topics in Applied Physics, edited by M.H. Brodsky (Springer-Verlag, Berlin, 1979), p.73

20) A.F. Ioffe and A.R. Regel, Prog. Semicond. 4, 237 (1960)

21) H. Fritzsche in Physical Properties of Amorphous Materials, edited by D.Adler, B.B.Schwartz, and M.C. Steele (Plenum, New York, 1985), p.313

22) W.Spear and P.LeComber, Solid State Commun. 17, 9 (1975)

23) B. Meyerson and F.W. Smith, J.Non-Cryst. Solids 35\36, 435 (1980)

24) B. Meyerson and F.W. Smith, Solid State Commun. 34, 531 (1980)

25) M. Gorman and S.A. Solin, Solid State Commun. 15, 761 (1974)

26) Y. Inoue, S. Nakashima, A. Mitsuishi, S. Tabata, and S.Tsuboi, Solid State Commun. 48, 1071 (1983)

27) A. Morimoto, T. Kataoka, M. Kumeda, and T. Shimizu, Philos. Mag. B 50, 517 (1984)

28) J. Tejeda, N.J. Shevchik and M. Cardona, Proc. 5th Int. Conf. Amorphous and Liquid Semiconductors, edited by J.Stuke and W.Brenig (Taylor and Francis, London, 1974) p.

29) W.Y. Lee, J.Appl. Phys. 51, 3365 (1980)

30) M.H. Brodsky, M. Cardona, and J.J. Cuomo, Phys. Rev. B 16, 3556 (1977)

31) C.C. Tsai and H. Fritzsche, Solar Energy 1, 29 (1979)

32) H. Wagner and W. Beyer, Solid State Commun. 48, 585 (1983)

33) D.R. McKenzie, J. Phys. D: Appl. Phys. 18, 1935 (1985)

33a) B. Dischler, A. Bubenzer, and P. Koidl, Solid State Commun. 48, 105 (1985)

34) Y.Katayama and T.Shimada, Jpn. J. Appl. Phys. 19, suppl 19-2, 115 (1980)

35) J.A. Borders, S.T. Picraux, and W. Beezhold, Appl. Phys. Lett. 18, 509 (1971)

36) M.H. Cohen, H. Fritzsche, and S.R. Oshinsky, Phys. Rev. Lett. 22,1065 (1969)

37) L. Ley, J. Reichardt and R.L. Johnson, Phys. Rev. Lett. 49, 1664 (1982)

38) G.D.Cody in Semiconductors and Semimetals, Vol. 21 B, edited by J.I. Pankove (Academic, New York, 1984), p.11

39) M.H.Cohen, C.M.Soukoulis, and E.N.Economou, in Optical Effects in Amorphous Semiconductors, AIP conference Proceedings, Vol. 120, edited by P.C. Taylor and S.G. Bishop (AIP, New York 1984) p.371

40) W.B. Jackson, S.M. Keko, C.C. Tsai, J.W. Allen, and S. J. Oh, Phys. Rev. B 31, 5187 (1985)

41) G.D.Cody, T.Tiedje, B.Abeles, B.Brooks and Y.Goldstein, Phys. Rev. Lett. 47, 1480 (1981)

42) D.K. Basa and F.W. Smith, (paper on annealing to be communicated)

43) M. Lax, Phys. Rev. 109, 192 (1958)

44) J.M. Ziman, Models of Disorder (Cambridge Univ. Press, London, 1979)

45) W.E. Spicer and T.M. Donovan, Phys. Rev. Lett. 24, 595 (1970)

46) F. Abeles, Ann. d. Physique 3, 504 (1948)

47) O.S. Heavens, Optical Properties of Thin Solid Films (Academic, New York, 1955), Chap.4

48) D. Stroud, Phys. Rev. B 12, 3368 (1975)

49) D.A.G. Bruggemann, Ann. Phys. (Leipzig) 24, 636 (1935)

50) R. Landauer, J.Appl. Phys. 23, 779 (1952)

51) J.C. Maxwell-Garnett, Philos. Trans.R. Soc. London 203, 385 (1904) ; 205, 237 (1906)

52) G.B.Smith J.Phys. D 10, L 39 (1977)

53) G.A. Niklaason, C.G. Granquist, and O. Hunderi, Appl. Opt. 20, 26 (1981)

54) L.R. Pointer, E.T. Arakawa, M.W. Williams, and J.C. Ashley, Radiat. Res. 83, 1 (1980)

55) K. Mui and F.W. Smith, Phys. Rev. B 35, 8080 (1987)

56) H.R. Philipp, J.Phys. Chem. Solids 32, 1935 (1971); H.R Philipp, J.Electrochem. Soc. 120, 295 (1973)

57) H.R. Shanks, C.J. Fang, L. Ley, M. Cardona, F.J.Demond, and S. Kalbitzer, Phys. Status. Solidi B 100, 43 (1980)

58) C.J. Fang, L. Ley, H.R. Shanks, K.J. Gruntz, and M. Cardona, Phys. Rev. B 22, 6140 (1980)

59) K. Nakazawa, S. Ueda, M. Kumeda, A. Morimoto, and T. Shimizu, Jpn.J.Appl. Phys. 21, L176 (1982)

60) F. Fujimoto, A. Ootsuka, K. Komaki, Y. Iwata, I. Yamane, H. Hamashita, Y. Hashimoto, Y. Tawada, K. Nishimura, H. Okamoto, and Y. Hamakawa, Jpn.J.Appl. Phys. 23, 810 (1984)

61) C.J. Mogab, J. Electrochem. Soc. 7, 932 (1973)

62) W.G. Spitzer and D.A. Kleinman, Phys. Rev. B 121, 1324 (1961)

63) W.E. Spear and P. LeComber, J. Non-Cryst. Solids 8-10, 727 (1972)

64) A. Mearns, Thin Solid Films 3, 201 (1969)

65) M. Hirose, in Semiconductors and Semimetals, Vol. 21 A edited by J.I. Pankove (Academic, New York, 1984), p.9

66) D.B. Fraser, in Pumping of hazardous gases published by the Thin Film Division, American Vacuum Society (1979)

67) D.M. Hoffman, J. Vac. Sci. Technol 16, 71 (1979)

68) L.E. Davis, N.C. MacDonald, P.W. Palmberg, G.E. Riach, and R.E. Weber, Hand book of Auger Electron Spectroscopy (Physical Electronics Division, Perkin-Elmer Corporation, Eden Prairie, MN, 1976)

69) C.L.Nagendra and G.K.M.Thutupalli, Vacuum 31, 141 (1981)

70) J. Bullot, M. Gauthier, M. Schmidt, Y. Catherine, and A. Zamouche, Philos. Mag. B 49, 489 (1984)

71) D.R. McKenzie, L.C. Botten, and R.C. McPhedran, Phys. Rev. Lett. 51, 280 (1983)

72) J.C. Knights, R.A. Lujan, M.P. Rosenblum, R.A. Street, D.K. Bieglesen, and J.A. Reimer, Appl. Phys. Lett. 38, 331 (1981)

73) Y. Catherine and G. Turban, Thin Solid Films 60, 193 (1979)

74) J.C. Phillips, Bonds and Bands in Semiconductors (Academic, New York, 1973)

75) A.Skumanich, A.Frova, and N.M.Amer, Solid State Commun. 54, 597 (1985); F. Boulitrop, J. Bullot, M. Gauthier, M. P Schmidt, and Y. Catherine, ibid, 54, 107 (1985)

76) A. Guivarch, J. Richard, M. Le. Contellec, E. Ligeon, and J. Fontenille, J. Appl. Phys. 51, 2167 (1980).

77) Y. Catherine, A. Zamouche, J. Bullot, and M. Gauthier, Thin Solid Films 109, 145 (1983)

78) J. Saraie, Y. Fujii, M. Yoshimoto, K. Yamazoe and H. Matsunami, Thin Solid Films 117, 59 (1984)

79) J.A. Reimer, R.W. Vaughan, J.C. Knights, and R.A. Lujan, J. Vac. Sci. Technol. 19, 53 (1981)

80) J.C. Phillips, J. Non-Cryst. Solids 34, 153 (1979)

81) J.L. Martins and A. Zunger, Phys. Rev. Lett. 56, 1400 (1986)

82) G. Lucovsky, J. Yang, S.S. Chao, J.E. Tyler, and W. Czubatyi Phys. Rev. B 28, 3225 (1983)

83) G. Lucovsky, Solid State Commun. 29, 571 (1979)

84) N.L. Alpert, W.E. Keiser, H.A. Szymanski, IR Theory and Practice of Infrared Spectroscopy (Plenum, New York, 1970)

85) W. Beyer, H. Wagner, and H. Mell, in Material Research Society Vol. 49, edited by D. Adler, A. Madan, and M.J. Thompson, (Plenum, New York, 1985), p.189

86) Y. Hishikawa, J.Appl. Phys. 62, 3150 (1987)

87) P.J. Zanzucchi in Semiconductors and Semimetals, Vol.21 B, edited by J.I. Pankove (Academic, New York, 1984), p.113

88) W.L. Lin, H.K. Tsai, S.C.Lee, W.J. Sah, and W.J. Tzeng, Appl. Phys. Lett. 51, 2112 (1987)

89) K.D. MacKenzie, J.R. Eggert, D.J. Leopold, Y.M. Li, S.Lin, and W.Paul, Phys. Rev. B 31, 2198 (1985)

90) G.W. Bethke and M.K. Wilson, J.Chem.Phys.26,1107 (1957)

91) G. Socrate, Infrared Characteristic Group Frequencies (Wiley, New York, 1980)

92) A. Matsuda, T. Yamaoka, S.Wolff, M.Kayama, Y. Imanishi, H. Kataoka, H. Matsuura, and K. Tanaka, J. Appl. Phys. 60, 4025 (1986)

93) E.A. Fagen, in Amorphous and Liquid Semiconductors, Vol. edited by J.Stuke and W.Brenig, (Taylor and Francis, London, 1974), p.

94) D. Beeman, R. Tsu, and M.F. Thorpe Phys. Rev. B 32, 874 (1985)

95) R.J. Nemanich, S.A. Solin, and R.M. Martin, Phys. Rev. B 32, 6348 (1981)

96) H. Richter, Z.P. Wang, and L. Ley, Solid State Commun. 39, 625 (1981)

97) J.S. Lannin, in Semiconductors and Semimetals, Vol. 21 B, edited by J.I. Pankove (Academic, New York, 1984), p.159

98) Z. Iqbal, S. Veptek, A.P. Webb, and P. Capezzuto, Solid State Commun. 37, 993 (1981)

99) W.G. Spitzer, D. Kleinman, and D. Walsh, Phys. Rev.113, 127 (1959); 133 (1959)

100) H. Mukaida, H. Okumura, T.H. Lee, H. Davimon, E.Sakuma, S.Misawa, K.Endo, and S.Yoshida, J.Appl.Phys. 62, 254 (1987)

101) M.H. Brodsky, R.S. Title, K. Weiser, and G.D. Pettit, Phys. Rev. B 1, 2632 (1970)

102) M.L. Theye, in Thin Film Technology and Applications, edited by K.L. Chopra and L.K. Malhotra (Tata Mc Graw-Hill, New Delhi, 1985), p.163

103) L. Ley, in The Physics of Hydrogenated Amorphous Silicon II, Vol. of Topics in Applied Physics, edited by J.D. Joannopoulos and G. Lucovsky (Springer-Verlag, Berlin, 1983), p.61

104) B. Von Roedern, L. Ley, M. Cardona, and F.W. Smith, Philos. Mag. B 40, 433 (1979)

105) W.Y. Ching, C.C. Lin, and L. Guttman, Phys. Rev. B 16, 5488 (1977)

106) J.C. Phillips, Phys. Rev. Lett. 20, 550 (1968); Rev. Mod. Phys 42, 317 (1970)

107) J.A. Van Vechten, Phys. Rev. 182, 891 (1969); 187, 1007 (1969)

108) B.F. Levine, J. Chem, Phys. 59, 1463 (1973)

109) S.H. Wemple, J. Chem, Phys. 67, 2151 (1977)